University of Naples Federico II
Department of Industrial Engineering

Doctorate School of Industrial Engineering

Ph.D. degree in Mechanical Engineering

Design and Analysis of Radial-Inflow Turbines for Small Scale Organic Rankine Cycles Applications

Ph.D. Candidate:
Alessandro Cappiello

Supervisors:
Prof. Raffaele Tuccillo
Prof. Maria Cristina Cameretti

Thesis submitted in 2022

Abstract

Single stage Radial-Inflow Turbines (RITs) are a promising alternative to volumetric machines to achieve flexible, lightweight and compact expanders for tens of kW scale Organic Rankine Cycle (ORC) power plants. However, their design is made extremely challenging by several peculiar characteristics of these applications. Above all, the exceptionally large expansion ratio leads to the insurgence of particularly high Mach numbers, demanding special care to shape the flow passages. Nonetheless, the organic fluids generally exploited are made up of complex molecules, entailing non-ideal gasdynamics effects. As a result of these exceptional peculiarities, conventional RIT design rules are often impractical for this class of turbines.

In the present thesis, RIT design methods are developed, encompassing preliminary design and first guess geometry generation. Particularly, a meanline design code is developed and used to carry out parametric analyses of ORC RIT design space for several test cases. Optimal design requirements and loss components are discussed.

A design method for RIT convergent-divergent vanes is also presented. The approach relies on a Method of Characteristics-based algorithm –for the design of the divergent section– whose extension to dense gases is provided.

The codes are used to design several RIT convergent-divergent stators, investigating the effect of stator design parameters on stator loss and downstream flow field uniformity –for which a novel figure of merit is introduced– that showed conflicting trends.

Thus, the effects of stator efficiency and stator downstream flow field

uniformity levels on the unsteady stator-rotor interaction, rotor operation and stage efficiency are assessed by means of unsteady CFD calculations, showing that the stator downstream uniformity might outweigh the stator efficiency. Therefore, designing the stator aiming only at its efficiency might lead to highly substantial configurations from stage efficiency point of view.

The role of the stator-rotor radial gap size is analyzed designing several stator geometries of increasing outlet radius, showing that, for this unconventional operative conditions, this parameter can play a crucial role in loss production and expansion ratio share between vaned and vaneless region of the stationary component.

Finally, the results presented in this thesis allow to infer design guidelines for the rather exceptional flow conditions that characterize small scale supersonic RITs for ORC applications.

Acknowledgements

I wish to express my genuine gratitude to my PhD supervisors, Prof. Raffaele Tuccillo and Prof. Maria Cristina Cameretti, who have guided me through this three-year journey. Their valuable advice and constant support helped me to grow as a researcher.

I would also like to thank Dr. Matteo Pini, who supervised my visiting stay at TU Delft, for his commitment and dedication and for many precious conversations, that have been a continuous source of inspiration.

I also wish to thank my friends Luigi Sequino and Marco Di Marzo, who made the time spent at Unina more enjoyable. Likewise, I also want to thank all the people that I met at TU Delft, who welcomed me since the beginning of my stay.

Finally, a special thanks goes to my family, for their love and unconditional support for all the challenges that I have undertaken.

Contents

List of Figures

List of Tables

Nomenclature

Latin Symbols

$\dot{m}$	Mass flow rate
$\dot{V}$	Volume flow rate
$\mathcal{M}$	Molecular mass
$\mathcal{R}$	Universal gas constant
Ma	Mach Number
Re	Reynolds Number
a	Speed of sound
b	Vane/Blade height
c	Flow velocity (abs frame of reference)
c_p	Specific heat at constant pressure
c_v	Specific heat at constant volume
D_s	Specific Diameter
E	Energy

f	Frequency
h	Enthalpy
I	Rothalpy
k	Polytropic exponent
m	Characteristic curve slope / meridional coordinate
N	Solidity
N_s	Specific Speed $= \omega \frac{\sqrt{\dot{V}_{5,is}}}{(h_{01}-h_{5,is})^{3/4}}$
P	Power
p	Pressure
R	Radius
R^*	Degree of reaction $= \frac{h_4-h_5}{h_{01}-h_5}$
R_p	Pressure-based reaction degree $= \frac{p_4-p_5}{p_{01}-p_5}$
s	Entropy
T	Temperature
t	Time
U	Blade peripheral velocity
V	Specific volume
w	Flow velocity (rel frame of reference)
x	Axial coordinate
Z	Compressibility factor/ Vane or blade count

Greek Symbols

α	Flow angle (abs frame of reference)
β	Flow angle (rel frame of reference)
β_{met}	Metal angle

Δ	Deviation
Γ	Fundamental Derivative of Gasdynamics
γ	Specific heat ratio
γ_{pv}	pressure-volume isentropic exponent
μ	Mach angle
ν	Prandtl-Meyer Function
Ω	Turbine rotational speed in RPM
ω	Turbine rotational speed in rad/s
Φ	Flow Coefficient $= \frac{c_{\mathrm{m,5\ is}}}{U_4}$
ϕ	Velocity potential
Π	Expansion/Compression ratio
Ψ	Work Coefficient $= \frac{\Delta h_{\mathrm{TS,\ is}}}{U_4^2}$
ρ	Density
σ	Molecular complexity
τ	Time period
θ	Tangential coordinate / wrap angle
φ	Streamline angle
ζ	Enthalpy loss coefficient $= \frac{h-h_s}{1/2c_{is}^2}$

Subscripts

θ	Tangential component
c	Property at critical point
m	Meridional component
mid	Mid-span
opt	Optimal value

tg	Target
x	Axial component
0	Total condition
1	Volute inlet
2	Stator inlet
3	Stator outlet
4	Rotor inlet
5	Rotor outlet
INT	Vaneless Interspace
is	Isentropic
LR	Left-Running
N	Nozzle
R	Rotor
r	Reduced quantity
RR	Right-Running

Acronyms

0D	Zero-Dimensional
1D	One-Dimensional
2D	Two-Dimensional
3D	Three-Dimensional
AXT	AXial Turbine
BZT	Bethe-Zel'dovich-Thompson
CCHP	Combined Cooling Heat and Power
CFD	Computational Fluid Dynamics

CHP	Combined Heat and Power
EoS	Equation of State
ISRE	Isentropic Simple Radial Equilibrium
LE	Leading Edge
LuT	Look-up Table
mGT	micro Gas Turbine
MLN	Minimum Length Nozzle
MoC	Method of Characteristics
ORC	Organic Rankine Cycle
PDE	Partial Differential Equation
RIT	Radial Inflow Turbine
TC	Test Case
TE	Trailing Edge
WHR	Waste Heat Recovery

CHAPTER 1

INTRODUCTION

1.1 General Aspects, History and Current Situation of Organic Rankine Cycle

The *Organic Rankine Cycle* (ORC) technology is a power producing plant technology based on the homonymous direct thermodynamic cycle, which features a working fluid evolving through thermodynamic states, similarly to steam Rankine Cycle, with which it shares the same thermodynamic transformations, (Macchi 2017b).
In its simplest configuration the cycle is made up of a compression (1-2), a heat addition (2-3), an expansion (3-4) and heat removal (4-1), figure 1.1a. Moreover, a recuperator might be present to recover part of the residual heat at the end of the expansion process (point 4, figure1.1a), which is then used to preheat the working fluid after the compression. Similarly to steam Rankine cycle power plants, a pump, an evaporator, an expander and a condenser are used to achieve the thermodynamic transformations (1-2), (2-3),(3-4) and (4-1), respectively, arranged as in the schematic representation provided in figure 1.1b.

However, differently from its steam-based counterpart, the ORC features an organic medium employed as working fluid. This peculiarity, which might

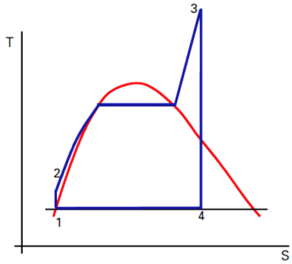

(a) Thermodynamic Cycle

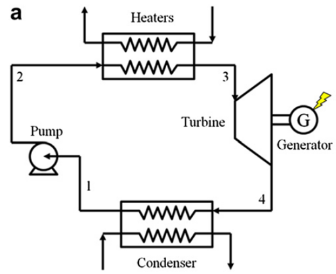

(b) Plant Schematic (Ho, Mao, and Greif 2012)

Figure 1.1: Organic Rankine Cycle

appear minor at first glance, entails major differences in plant peculiarities, technical solution adopted and machine design, (Astolfi 2017) with some details on the topic provided in sections 1.3 and 1.2.

It should be mentioned that ORC strength, in fact, relies on the possibility of selecting the working fluid; the latter can be seen as an additional degree of freedom for the design of the thermodynamic cycle, which provides the designer with the opportunity to better match the temperature profiles with heat source and sink in the Heat Exchangers (HEs), reducing irreversibilities and improving thermodynamic efficiency, (Colonna, Casati, et al. 2015). Additionally, organic fluid nature is such to make them well suited to exploit heat sources at moderate temperature levels, (Colonna, Casati, et al. 2015). In fact, this provides access to heat source which would be difficult to access by means of more conventional power cycles. On the other hand, the moderate maximum allowable temperature, limited by fluid thermal decomposition, inevitably affects the maximum conversion efficiency that can be reached by ORC technology, making its development and perspective related to novel fluids design and development.

Despite the rapid growth of interest towards this technology, which has been mainly led by an enhanced attention to environmental issues and more stringent emission regulations, the ORC technology is far from being a novel concept, (L. Bronicki 2017). As reported by Colonna, Casati, et al. (2015), who have traced back ORC evolution from its conception up to current and future applications, patents and prototypes concerning expanders working with fluids other than water can be found from the twenties of 19$^{\text{th}}$ century, e.g., those by Ofeldt (1898) and Tissandier and Parville (1888). However, according to Colonna, Casati, et al. (2015), the first milestone of this technology was set by Prof. Luigi d'Amelio's activity at Federico II University of Naples who developed in 1936 a solar driven plant for irrigation in north Africa (d'Amelio 1935), highlighting the first turbine design criteria depending on the working fluid (d'Amelio 1936a,b), also resulting in some prototypes. Bronicki, who was active in the second half of the 1900, also contributed actively to this field (Tabor and L. Bronicki 1963), as well as developing and testing some ORC plants (Spencer 1989). Other influential personalities who strongly contributed to ORC development are Prof. G. Angelino, Prof. G. Gaia and Prof. E. Macchi who were active in the second half of 20$^{\text{th}}$ century at Politecnico di Milano. However, for a detailed review of the ORC development the reader is referred to Colonna, Casati, et al. (2015).

Since the first milestones in the ORC development, a long path has been walked, leading to substantial improvements in ORC systems technological maturity, particularly for larger sizes, as witnessed by the continuous growth of the installed cumulative power occurred from the '90s (Colonna, Casati, et al. 2015). While the ORC systems historical developments have been characterized by discontinuous developments mainly due to changes in the economical scenario and oil price, e.g., the oil crisis of the '70s which strongly encouraged the developments of the ORC technology, nowadays its development is mainly led by the arisen environmental issues connected to fossil fuel exploitation as well as more stringent regulations on greenhouse gases and pollutant emissions and is also witnessed by the steep increase of the number of publication per year in the field of ORC systems after 2000 (Colonna, Casati, et al. 2015).

In this regard, improving the efficiency of existing power plant as well as exploiting renewable and renewable-equivalent energy sources is clearly appealing and promising thanks to the above-mentioned features of the organic fluids, enabling the exploitation of low temperature energy sources. This has led to numerous applications for the ORC technology, many of which already consolidated and viable, while other still being in an emerging stage. Furthermore, the use of ORC systems makes the opportunity of energy storage at hand, i.e., via *thermal energy harvesting*, alleviating the non-programmable nature of renewable energy source in a much easier way then other renewable-based energy conversion technologies. Additionally, the opportunities for enhanced system integration are relevant, by means of *co-generation*, the so-called Combined Heat and Power (CHP), and *tri-generation* arrangement, namely the so-called Combined Cooling Heat and Power (CCHP), (Ahmadi, Rosen, and Dincer 2012; Boyaghchi and Heidarnejad 2015; Al-Sulaiman, Dincer, and Hamdullahpur 2010a).

1.1.1 Applications

To enlighten the strength, flexibility and potential for future developments of the ORC technology it is most certainly worth to give a brief overview of the wide variety of applications and fields in which this technology is exploited at present or could be in the near future. Nowadays, the ORC technology is employed to exploit several heat sources, among which *geothermal energy*, *biomass combustion*, *waste heat* from industrial plants, reciprocating engines and power producing plants in general, as well as *solar energy*.

Among these, *geothermal energy* stands as one of the most promising renewable energy sources, particularly to cover the base-load of electricity demands, thanks to large annual capacity and large availability. This energy source relies on hot spots non-uniformly spread over the surface of planet Earth, associated to underground reservoirs in which hot fluid –originated by either volcanic or tectonics phenomena– is trapped.
The first pilot plant based on the ORC technology exploiting the geothermal energy was built in the early 80s of 20^{th} century by Ormat, for low temperature energy sources, (Spadacini, Xodo, and Quaia 2017). Nowadays, ORC power plants exploiting geothermal energy are mainly large-scale plants used for liquid-dominated reservoirs, both in stand-alone configurations and in combination with steam plant, either in combined or bottoming configuration, with one up to three pressure levels.

Another viable energy source for ORC system integration is offered by *biomass combustion*, although its use was originally limited to large plants ($\geq 2\text{MW}_{\text{el}}$) powered by conventional steam Rankine cycle, due to the intrinsic limitations that arise when the size is lowered further. Conversely, the adoption of the organic Rankine cycle enabled to reduce the minimum plant size that can be fired by biomass combustion, the majority of plants being nowadays in the range of electric power from 500 kW up to 2 MW, and further reductions in the minimum electric power size are expected in the future (Guercio and Bini 2017). The adoption of ORC plants for biomass combustion exploitation is particularly appealing in sites and processes where biomass is largely available, such as wood-manufacturing plants and agriculture (Rahbar et al. 2017). In the former case, CHP arrangement is often chosen, further exploiting heat discharged by the ORC unit used either for district heating or process requirements, e.g., wood drying; furthermore, net electrical efficiency reaches 15-20%, while total energy efficiency can reach

90%, (Colonna, Casati, et al. 2015).

Yet, an incredibly relevant amount of thermal energy is rejected every year to the atmosphere, either under the form of unconverted heat from prime movers (stationary and mobile ones) or as waste heat from industrial processes. Forman et al. (2016) estimated the heat wasted worldwide in 2012 to be more than 68000 TWh. More recently, the wasted heat from industrial processes in Europe was computed by Bianchi et al. (2019) and found to be about 920 TWh per year. This enormous amount of thermal energy, if recovered, would offer a renewable equivalent energy sources to be exploited for power cycles. However, this path is not easy to pursue as the temperature levels at which this energy is usually available are often too low to be exploited by means of conventional power cycle, say steam Rankine cycles. On the other hand, the use of ORC technology, thanks to the possibility of selecting the working fluid, offers the opportunity to exploit these heat sources for power production purpose, usually referred to as *Waste Heat Recovery* (WHR).

The most relevant sources of waste heat are industrial processes and prime movers. Particularly, for what concerns the former, energy is generally available at various temperature and the lower the temperature the higher the available energy (Colonna, Casati, et al. 2015). Most relevant applications are cement industry with waste heat being up to 40% of the process thermal input, steel and glass industry.

Other relevant contributors to the overall thermal energy which is wasted worldwide are prime movers. These, however, show substantially different peculiarities depending on technologies they rely on and whether stationary (*genset*) or mobiles applications are considered. This, in fact, often determines the variability of the load conditions, and, hence, available heat for the bottoming ORC. From overall waste heat contribution point of view, reciprocating engines are the most appealing prime mover, (D'Auria 2020), although their exploitation is challenging since the unconverted heat is rejected through different systems, e.g., cooling jacket, lubrication oil, radiation and exhaust gases, and at different temperature levels, too (Rahbar et al. 2017). If automotive applications are considered, the picture is further complicated by the difficulties of accommodating on board additional components and, particularly, by the highly variable load imposed by the driving conditions. However, if cargo ship engines are considered the latter issue is relived, as they usually work most of the time at constant load (Tian and Shu 2017). Yet, over the years several Internal Combustion Engine (ICE) manufacturers investigated WHR via bottoming organic Rankine cycle, e.g., Toyota (Oomori and Ogino 1993), BMW -considering passenger cars- (Ringler et al. 2009) and Volvo (Espinosa et al. 2010), also highlighting room for economic profitability. In this regard, 7-10% appears as a realistic estimation of achievable ORC efficiency for WHR from reciprocating engines, leading to fuel economy improvements about 10% and, thus, payback periods about 2-5 years, (Sprouse and Depcik 2013). Apart from the simple ORC configuration, in recent years more complex cycle configurations have been considered, e.g., a dual loop ORC for a light duty engine (Zhang, E. Wang, and Fan 2013) -arguably as a consequence of more stringent emission regulations together with increased fuel prices- showing a potential increase of power output about 15% at best efficiency point and about 40% at low load conditions.

More recently, the interest towards the adoption of turbo-expanders for WHR from reciprocating engines raised, as witnessed by several works, focusing particularly on heavy-duty diesel engine, e.g., the experimental work by Alshammari, Pesyridis, et al. (2018), the work by Karvountzis-Kontakiotis et al. (2017) highlighting large room for fuel economy improvements and strong effect of working fluid on size and performance of the ORC unit; Alshammari, Kontakiotis, and Pesyridis (2018) showing a potential for 5.4 % reduction in the brake specific fuel consumption, as well as the work by Lang, Colonna, and Almbauer (2013), who carried out a feasibility study on the use of turbo-generators for long-haul trucks, forecasting an additional 9.6 kW power output from the ORC unit -for a 150 kW power output obtained from the reciprocating engine-, with overall clutter within acceptable limits.

Since turbine preliminary design and thermodynamic cycle are mutually influencing each other, the assumption of constant turbine efficiency for thermodynamic cycle determination would likely lead to sub-optimal conditions and the optimal working fluid selection would be affected too (Song, Gu, and Ren 2016). To overcome this issue, more refined design approaches have developed over the years, moving towards more and more integration of system-turbine and system-turbine-heat exchangers simultaneous design and optimization (Bahamonde, Pini, Servi, et al. 2017); as well as approaches also taking into account load conditions derived from drive cycles for heavy-duty diesel engine emission certification (Robertson et al. 2016).

Among power producing plants, Joule cycle-based plants cover a relevant share of the market, among which small and micro Gas Turbines (mGT) are a widespread solution for distributed power generation. In this regard, in spite of the limited contribution to the overall installed power, small and micro Gas Turbines are the most relevant contributors to the overall number of unit sold, (Slade and Palmer 2019).

Starting from the simple Joule cycle, several modifications have been proposed over the years aiming at improving cycle efficiency (Heppenstall 1998), with a particular focus on recovering the exhaust gas heat characterized by high temperature, (Najjar 2001). Among possible WHR solutions, the ORC technology is, of course, a viable one and its use has been first investigated by Najjar and Radhwan (1988). In this regard, L. Y. Bronicki and Schochet (2005) report about a pipeline compression station being the first installation of a bottoming ORC unit for a gas turbine plant.

Concerning small sized mGTs units, the implementation of a bottoming ORC unit has been observed to produce significant power output and efficiency increase, (Invernizzi, Iora, and Silva 2007). Moreover, the CO_2 emissions improvements have been documented by Ahmadi, Dincer, and Rosen (2012), who carried out energy and exergy analysis on a trigeneration mGT-ORC plant. Yet, the adoption of bottoming ORC units has been evaluated for more complex plants too, such as mGT with steam injection and bottoming ORC in CHP arrangement reported by Moradi et al. (2020), with improvements from emissions point of view; or the introduction of an ORC unit as bottoming plant to a solar-assisted mGT studied by Abagnale et al. (2017) and Cameretti et al. (2015c), who focused both on plant optimization (Cameretti et al. 2015a) and on expander requirements and critical aspects (Cameretti et al. 2015b).

Another promising application for ORC technology is the *solar energy.* In fact, the energy radiated by the sun can be exploited to produce electricity in a thermodynamic fashion by concentrating the solar radiation either by means of punctual (Central Solar Tower and heliostats, solar dish collector) or linear collectors (Fresnel or parabolic collectors), so to produce a high temperature heat transfer fluid (mineral oil or molten salt) to be exploited for a direct thermodynamic cycle, (Orosz and Dickes 2017). However, the maximum allowable temperature for an organic fluid generally prevents the use of Central Solar Tower systems, in which case temperature as high as 1000 °C can be reached. However, low temperature applications can be considered promising for downscaling solar-based thermodynamic energy production plants up to kW levels, reducing investment cost as the ORC system could work at lower temperatures, (Quoilin, Broek, et al. 2013), or in low-concentration manner, (Markides 2015). Published literature also reports about existing plants of about 1 MW_e (Canada et al. 2005), as well as kW_e scale plants at proof-of-concept stage, (Quoilin, Orosz, et al. 2011), and even low/medium temperature experimental investigations using planar collectors (originally intended for hot water production) with efficiency about 5% and technical feasibility, (J. Wang, Zhao, and X. Wang 2010).

Beside the well-established heat sources, other more challenging applications have been considered as potentially viable options for ORC technology, such as exhaust heat from *fuel cells*, e.g., Al-Sulaiman, Dincer, and Hamdullahpur (2010a,b), *data center cooling*, e.g., Capozzoli and Primiceri (2015), Ebrahimi, G. Jones, and A. Fleischer (2014), and Ebrahimi, G. F. Jones, and A. S. Fleischer (2017), *oceanic thermal gradient* exploiting the temperature difference existing at different depth levels in oceanic water as heat source and sink, e.g., Avery and Wu (1994), Bombarda, Invernizzi, and Gaia (2013), Ikegami and Morisaki (2012), and Vega (2010) and finally desalination plants via reverse osmosis, with the pump being driven by an ORC cycle exploiting solar energy, e.g., Bruno et al. (2008) and García-Rodríguez and Delgado-Torres (2007).

1.2 Organic Fluids

The main point which distinguishes the Organic Rankine cycle from its steam-based counterpart is clearly the working fluid, which in turn has a major impact on several fundamental and technical aspects, from thermodynamic performance up heat exchanger and turbine design.

Typical organic fluids employed in ORC applications are *hydrocarbons*, *alkanes*, *siloxanes*, *alcohols* and *refrigerants*. Very often organic fluids are characterized by a large molecular mass, $\mathcal{M}$, leading to lower value of the speed of sound, a, with respect to air and other ideal gases, thus more easily leading to the insurgence of supersonic flows within turbine passages (Colonna, Casati, et al. 2015; Persico and Pini 2017). As an examples, Fig. 1.2 shows the molecular mass and speed of sound values at ambient temperature for some organic fluids, in comparison to those of air, showing how relevant these changes can be. As one can see, organic fluids are generally characterized by larger molecular mass values than air, while ethanol is the only exception of the plot, showing a comparable molecular mass with respect to the one of air. Conversely, particularly relevant are the differences of molecular mass featured by two of the siloxanes in Fig. 1.2, i.e., MD_3M and D6. Likewise, with the only exception of ethanol, all organic fluids in the histogram show substantially lower speed of sound values than the one of air. Again, the most notable fluids in figure appear to be MD_3M and D6 with a speed of sound at ambient conditions below 100 m/s.

Typical ORC working fluids cannot be modelled as ideal gases as a consequence of the thermodynamic state usually encountered in ORC applications, consequently, several Equations of State (EoS) have been developed over the years. Particularly widespread are the cubic EoS, such as those by Peng and Robinson (1976), Soave (1972), and Van Der Waals (1873). Also, more complex equations of states have been developed, such as the multiparameter EoS, (Span 2013). Alternatively, thermodynamic libraries, such as REFPROP (E. W. Lemmon, Huber, and McLinden 2010) or CoolProp (I. H. Bell et al. 2014), can be used.

Many other differences exist between organic fluids and steam, although one of the most notable concerns the shape of the saturation curve. Based on this consideration one can subdivide fluids into three classes, namely *dry*, *isentropic* and *wet*, according to the slope of the vapor saturation line; in this regard, Fig. 1.3 provides examples of the above-mentioned classes of fluids showing the saturation curve in the $(T - s)$ thermodynamic plane. More specifically, dry fluids exhibit a positive value of the quantity dT/ds, contrary to wet fluids, of which probably the most notable example is water,

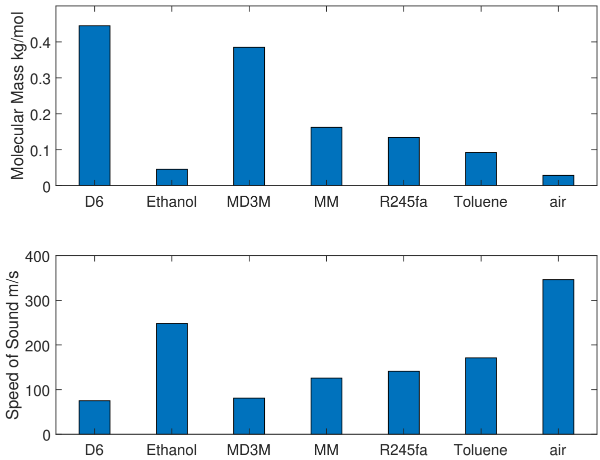

Figure 1.2: Molecular mass and speed of sound values at ambient temperature for some organic fluids and air

which show $dT/ds < 0$. Finally, for isentropic fluids exhibit an intermediate behaviour, with dT/ds tending to infinity, (Chen, Goswami, and Stefanakos 2010; Györke, Groniewsky, and Imre 2019).

The latter issue is related to the so-called *molecular complexity*, defined as the number of active degrees of freedom of a molecule (Colonna and Guardone 2006), which can be computed as in Eqn. 1.1, Harinck, Guardone, and Colonna (2009), in which $c_{v,idealgas}$ represents the specific heat at constant volume computed at critical temperature, T_c, by taking into account only the ideal gas contribution. The latter parameter influences both the fluid dynamic behaviour of the fluid and the shape of the saturation curve. For what concerns the second aspect, the higher the molecular complexity, the more the saturation curve tends to dry behaviour (Macchi 2017a). Additionally, more complex fluids are generally more suited to higher temperature applications, often leading to sub-atmospheric condensation, and usually allowing non-extractive regeneration, relieving the complexity of the expander design.

$$\sigma = \frac{2\mathcal{M}c_{v,idealgas}(T_c)}{\mathcal{R}} \tag{1.1}$$

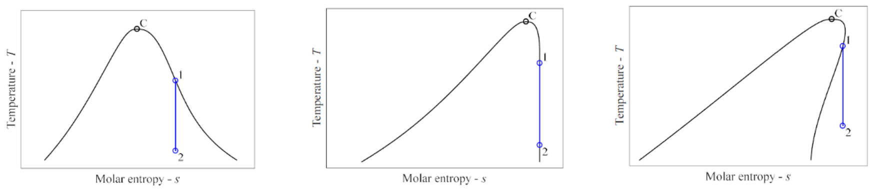

(a) R22 (b) R11 (c) Isopentane

Figure 1.3: Examples of wet (a), isentropic (b) and dry (c) fluids saturation curve (Györke, Groniewsky, and Imre 2019)

From a thermodynamic viewpoint, the working fluid also determines operating pressures levels, and hence the cycle expansion ratio, via the matching with heat source and sink. From basic thermodynamics it is known that having an heat exchange occurring under a larger temperature difference between hot and cold fluid results in a larger entropy generation, larger irreversibility and, hence lower cycle efficiency. Thus, it comes without saying that the chance of selecting the working fluid opens up the opportunity for improving the matching of temperature profiles with heat sources, so improving the thermodynamic efficiency. Even better matching opportunity can be achieved by means of transcritical cycles and fluid mixture, e.g., zeotropic mixtures, (Ho, Mao, and Greif 2012). In this context, the working fluid can then be regarded as an additional design variable available for the designer. As such, several procedures have been documented in published literature for the selection of the optimal working fluid, e.g., the work by Lampe et al. (2019). Nevertheless, the possibility to select the working fluid opens up wide opportunity to access low temperature heat sources, whose exploitation by means of conventional power cycles, say steam Rankine cycle, would be impractical. Anyhow, it is worth mentioning that the fluid selection should also meet other constraints, among which the environmental performance -expressed by the Global Warming Potential (GWP) and the Ozone Depletion Potential (ODP)-, flammability and toxicity levels and fluid price, with their relative weight been very much dependent on the application considered.

Besides the thermodynamic performance and other relevant criteria, upon selecting the optimal working fluid, one should bear in mind that different organic fluid may exhibit different gasdynamic behaviours, which severely impacts the fluid dynamic design of the expander, which, from cycle efficiency point of view, is known to be the most critical component (Quoilin, Orosz, et al. 2011).

In the forthcoming a short overview of the main thermodynamic properties affecting the gasdynamic behaviour of the flow, which also leads to flow features that are peculiar of the so-called *dense gases*, together with the modeling requirements and design implications, is provided.

1.2.1 Non-Ideal Effects in Compressible Flows

As mentioned previously in this chapter, organic fluid behaviour may substantially depart from the one of a perfect gas. Probably the most notable distinction in the dense gas region concerns the behaviour in compressible flow regime, that is ruled by the *Fundamental Derivative of Gasdynamics*, Γ, and particularly by its sign, i.e., along the expansion process occurring within turbine passages. Equation 1.2 provides a general expression for the fundamental derivative of gas dynamic, from Colonna, Nannan, et al. (2009):

$$\Gamma = 1 + \frac{\rho}{a}\left(\frac{\partial a}{\partial \rho}\right)_s \tag{1.2}$$

As it appears clearly, the fundamental derivative expresses the rate of change of the speed of sound with respect to density along an isentropic transformation.

If a perfect gas is considered, i.e., an ideal gas with constant specific heats c_p and c_v, the fundamental derivative can be expressed as in Eqn. 1.3, with γ being the ratio of the specific heats (Thompson 1971).

$$\Gamma = \frac{1}{2}(\gamma + 1) \tag{1.3}$$

As such, the fundamental derivative of a perfect gas can only be greater than 1, as γ is always a positive quantity. In this regard it is worth mentioning that the condition $\Gamma > 1$ is required for the existence of conventional compression shocks, (Thompson 1971). Additionally, $\Gamma > 1$ means that for a perfect gas the speed of sound always decreases through an isentropic expansion.

If the perfect gas assumption is relieved, Γ is allowed to assume any values, and, depending on its sign and value, different inviscid gasdynamic behaviour can be identified, namely the *non-ideal* and the *non-classical* gasdynamic behaviour. When $\Gamma < 1$ the speed of sound increases along an isentropic expansion, although the gasdynamic behaviour remains classical. In such conditions, Mach number may decrease through an expansion and shock losses might be reduced. When $\Gamma < 0$, non-classical behaviours, characterized by compression fans and the rarefaction shock waves, become admissible; also, under quasi-one dimensional assumption an opposite trend of area variation would be required for transitioning from $Ma < 1$ to $Ma > 1$, (Thompson 1971). As an examples, Fig. 1.4, shows the contour plots of Γ for some organic fluids in the $(T - s)$ diagram, focusing on the region in which $\Gamma < 1$, namely where non-ideality takes place. As one can see, all fluids presented in Fig. 1.4 show a region were $\Gamma < 1$ and, depending on the fluid, regions of $\Gamma < 0$ may exist, although very tight. Particularly, this is the case of MD_3M, Fig. 1.4f, and D6, Fig. 1.4e, which show regions of negative Γ in the proximity of the critical point.

Colonna and Guardone (2006) investigated the reasons at molecular scale for the non-ideal and non-classical gasdynamic behaviours exhibited by organic fluids by means of the van der Waals model. This model, despite not being quantitatively accurate provides direct link between the equation of state parameters and attractive and repulsive force at molecular scale. The model was then used to budget the contribution of molecular forces on the speed of sound, as well as the effect of molecular complexity, identifying minimum level of molecular complexity to allow non-ideal and non-classical behaviour.

After the first speculations of Bethe, Zel'dovich and Raizer, who were the first to hypothesize the existence of fluids characterized by $\Gamma < 0$, nowadays referred as Bethe-Zel'dovich-Thompson (BZT) fluids, only computational observations of rarefaction shock wave have been gathered so far, e.g., the work by Hoarau, Cinnella, and Gloerfelt (2021). Also, BZT fluids have been analyzed in cascade configuration by Monaco, M. S. Cramer, and Watson (1997) and the exact solutions of steady BZT flows through convergent-divergent nozzles have been provided by Guardone and Vimercati (2016).

For what concerns turbomachinery, the effect of the fundamental derivative on turbine losses has been scarcely addressed in published literature. Notable exceptions are the work by Baumgärtner, Otter, and A. P. S. Wheeler (2020) and Giuffre' and Pini (2020).

Different approaches have been presented in published literature to measure the effect of the average value of Γ along the expansion. Particularly, some authors use the average value of the polytropic exponent, k, which can be determined via a linear regression of the logarithms of Eqn. 1.4, (Baumgärtner, Otter, and A. P. S. Wheeler 2020); other authors use the average value of the pressure-volume isentropic exponent, γ_{pv}, expressed as in Eqn. 1.5 and linked to Γ via Eqn. 1.6, (Giuffre' and Pini 2020). Furthermore, it is worth mentioning that, when the diluted gas region is approached, γ_{pv}

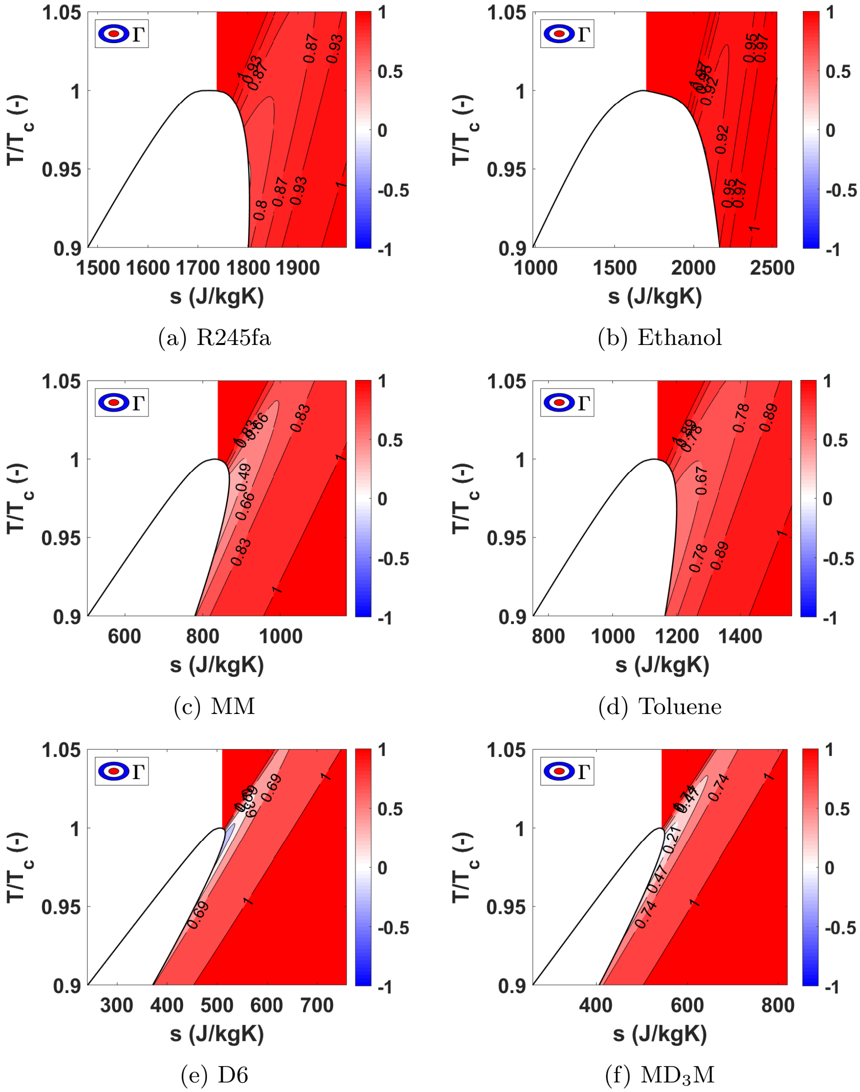

(a) R245fa (b) Ethanol

(c) MM (d) Toluene

(e) D6 (f) MD_3M

Figure 1.4: Γ contour in $(T - s)$ thermodynamic plane

approaches the value of the specific heat ratio γ.

$$\left(\frac{\partial p}{\partial \rho}\right)_s = k\frac{p}{\rho} \tag{1.4}$$

$$\gamma_{pv} = -\frac{v}{p}\left(\frac{\partial p}{\partial v}\right)_s \tag{1.5}$$

$$\Gamma = \frac{1}{2}\left[k + 1 - \frac{v}{k}\left(\frac{\partial k}{\partial v}\right)_s\right] \tag{1.6}$$

Baumgärtner, Otter, and A. P. S. Wheeler (2020) investigated experimentally and numerically for various fluids the effect of polytropic exponent k on axial turbine vane losses for a series of profiles designed for various discharge Mach number from 0.9 to 1.7, while keeping the *Re* number constant by varying upstream and downstream boundary conditions, and found that the lower the exponent the higher the losses and the larger the flow turning at the vane Trailing Edge (TE), increasing the value of the base pressure. Dense gas effects on TE losses and wake profile were investigated numerically and experimentally by F. J. D. Galiana, A. P. Wheeler, and Ong (2016), both on flat plate and RIT supersonic vanes, who found that dense gas effects at TE increase losses and that, lowering the fundamental derivative, the size of the base region and the base pressure are reduced and so is the wake size. More recently, this aspect was investigated by Baumgärtner, Otter, and A. P. S. Wheeler (2021b) who observed that when the average polytropic exponent is lowered, the Prandtl-Meyer expansion around the Trailing Edge is larger, and so the flow turning, reducing the size of the separated base region and, eventually leading to narrower wake profile. Nevertheless, losses are seen to increase.

The effect of the working fluid on axial turbine losses was investigated by Giuffre' and Pini (2020), too, who analysed different parameters for describing the similarity concept in non-ideal conditions and proposed to use the volumetric expansion ratio as a similarity parameter.

The polytropic exponent is also known to affect the value of the Prandtl-Meyer function, ν, required to accelerate the flow up to a target Ma number. Particularly, the lower the value of k, the higher the value of ν, and hence the flow deviation, required to reach a target Ma number, (A. P. S. Wheeler and Ong 2013). Also, the lower the k, the larger the size of the divergent portion of the nozzle resulting from the Method of Characteristics (MoC), both for sharp-edged nozzles (Cappiello and Tuccillo 2021b) and for smoothly contoured throat (A. P. S. Wheeler and Ong 2013).

The non-ideality of the flow has also been seen to affect the choking behaviour of a compressible swirling flow, leading the total Mach number, Ma_0, at which chocking occurs to be strongly influenced by the pressure-volume isentropic exponent, γ_{pv}. Hence Ma_0 at which chocking occurs increases for increasing values of γ_{pv} (Tosto et al. 2021).

Additionally, concerning MM expansion process in non-ideal conditions, ($\Gamma < 1$), quantitative and qualitative changes with respect to dilute-gas behaviour have been observed by Romei et al. (2019) for MM supercritical expansion to supersonic conditions, with strong influence of the total inlet conditions.

Finally, M. T. White (2021) investigated the validity of the fundamental derivative in equilibrium and non-equilibrium two-phase expansion.

Another relevant parameter contributing to determine the non-ideality of the flow is the so-called compressibility factor, Z, defined as in Eqn. 1.7, which actually measures the departure of the fluid behaviour from the ideal-gas law, (I. Bell and E. Lemmon 2017). As such, the compressibility factor is equal to 1 in ideal-gas conditions, while it progressively reduces as the non-ideality increases and the fluid departs from ideal-gas behaviour. Figure 1.5 provides some examples of the compressibility factor contours in $(T - s)$ thermodynamic plane –only showing regions of $Z < 1$– for typical organic fluids, highlighting the substantial departure from ideal gas behaviour ($Z \neq 1$).

$$Z = \frac{p}{\rho R T} \tag{1.7}$$

The effect of compressibility factor on non-ideal compressible flows was investigated by Spinelli et al. (2018), performing experiments on convergent-divergent nozzles for two working fluids (air and MDM) at various levels of compressibility factor. They observed that for a given geometry the pressure ratio is higher in non-ideal conditions, with increasing pressure ratio differences for increasing non-ideality, and that, in turn, the centreline Mach number decreases.

More recently, the compressibility factor has been seen to play a relevant role in turbine performance by Baumgärtner, Otter, and A. P. S. Wheeler (2021a), who observed that lower losses occur at lower compressibility factor, which has a beneficial effect both on shock losses, TE losses and boundary layer losses, although via different mechanisms. Particularly, the boundary layer losses appear to be relieved as, when Z is reduced, a larger density change occurs across the boundary layer, leading to have less mass flow rate flowing in the higher strain region and hence less dissipation. Concerning

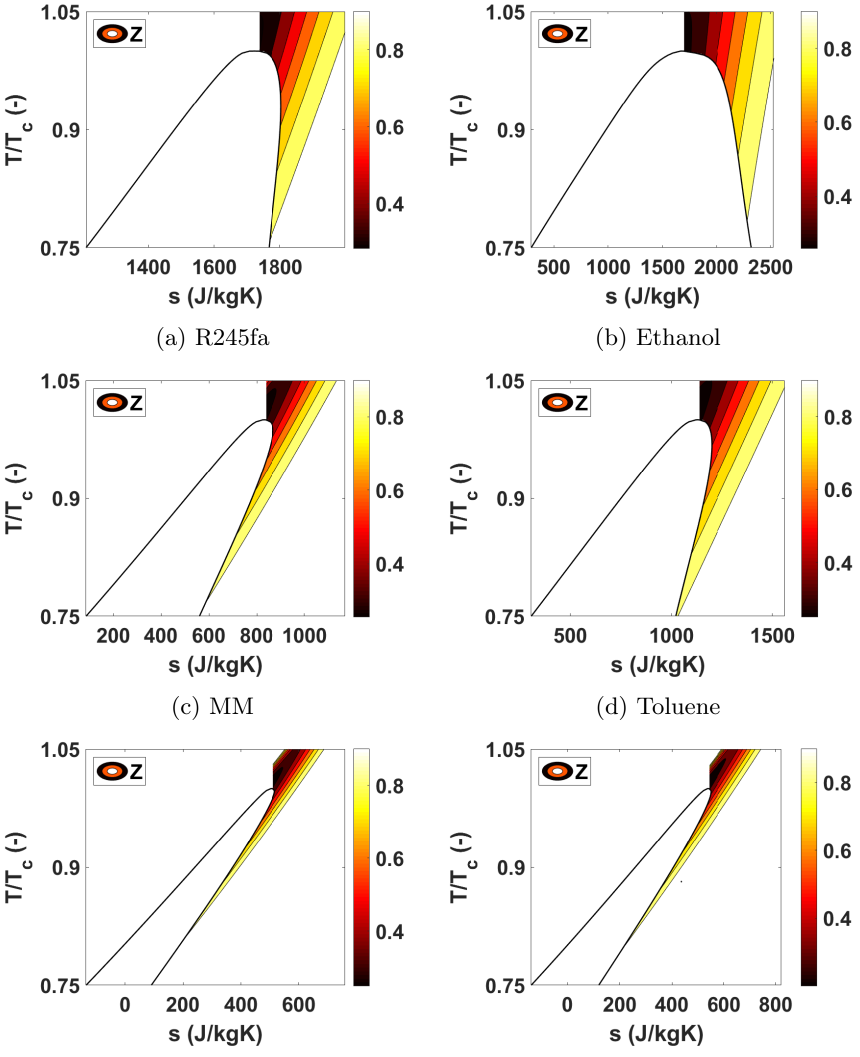

(a) R245fa (b) Ethanol

(c) MM (d) Toluene

(e) D6 (f) MD_3M

Figure 1.5: Z contour in $(T - s)$ thermodynamic plane

TE losses, the authors observed that, as a consequence of the change in boundary layer shape factor, when the compressibility factor is reduced the trailing edge separation occurs earlier, leading to higher base pressure and lower TE losses.

Finally, with respect to the combined effect of compressibility factor and fundamental derivative some work has been carried out by Otter, Baumgärtner, and A. P. S. Wheeler (2021) who investigated the losses of transonic axial turbine vane profiles by means of a generic working fluid approach, accounting for the variability of average polytropic exponent, k, inlet compressibility factor, Z, at various level of discharge Ma number, while maintaining the same Re number. Results showed that compared to air, losses are higher at low k and high Z particularly at high Ma number.

1.3 Plant and Components

Despite the Organic Rankine Cycle and the steam Rankine Cycle share the same working principle and –at least in the simplest configuration of the plant– main components, in practice the working fluid change entails relevant modifications, leading to different peculiarities and technical solutions, making the two suited for different applications. The present paragraph reviews the main repercussions of working fluid change from the viewpoint of plant and components, referring to simple and recuperated organic Rankine cycles.

From the point of view of plant components, Fig. 1.1, a particularly relevant difference with respect to steam Rankine cycle concerns the slope of the vapour saturation line, that has major implications in the expander selection and design. In fact, its slope determines whether an expansion starting from saturated vapour (or mildly superheated vapour) leads to the formation of liquid droplets along the expansion line, and, hence whether or not a liquid-tolerant machine has to be adopted.

In contrast to steam Rankine, superheating in not generally beneficial from ORC cycle efficiency point of view, as a result of the different slope of the isobars in the $(T - s)$ diagram; but non-extractive regeneration is often possible (Colonna, Casati, et al. 2015).

Another peculiarity of organic fluids, which has strong implications on the expander design, concerns the enthalpy drop, Δh, corresponding to a given expansion ratio Π. For typical cycle configurations, despite the matching with heat source and sink determines rather large expansion ratios, the enthalpy drop attaining to organic Rankine cycles is generally lower than the one attaining to steam Rankine cycles. This occurrence, in case of organic fluids, often makes possible to adopt single stage expanders. However, the adoption of single stage machines, in combination with the low speed of sound values that characterize organic fluids, frequently leads supersonic flows within stator passages to arise, making the design of single stage machines challenging.

An additional difference of the organic fluids with respect to water concerns the latent heat of vaporization, that is substantially smaller than the one attaining to water, (Quoilin, Broek, et al. 2013). As a consequence, for a given thermal input power, a larger mass flow rate is required when the thermodynamic cycle is designed to operate with typical organic mediums, entailing various effects: on the one hand, a larger mass flow rate leads to larger expansion machines, with beneficial effect on the efficiency; on the other hand, a larger mass flow rate also entails a large power consumption required by the pump.

When turboexpanders are considered, if designed to work under the same conditions, ORC turbines show a rotational speed from 2 to 10 times smaller than the one attaining to steam turbines, though the advantage is reduced if simpler molecules are considered (Colonna, Casati, et al. 2015).

Furthermore, ORC-based systems also show much lower maximum operative pressure and temperature with respect to conventional water based Rankine cycles, which makes their use for domestic application safer (Qiu, Liu, and S. Riffat 2011). Some of organic fluids are also good lubricant and electrical insulators.

Based on the above observations, some conclusions can be drawn concerning the suitability of ORC and steam Rankine cycle. Particularly, for power output ranging from few kW to few MW the ORC represents a better choice than the conventional steam Rankine cycle, which is unlikely to be efficient and cost effective in this scale (Colonna, Casati, et al. 2015). More specifically, from the turbomachinery point of view in the small power range the selection of a steam Rankine cycle would result in a small multistage machine, hence with high cost and limited efficiency. Conversely, the adoption of an organic Rankine cycle, often allows the use of single stage machine of larger size.

However, it shall be mentioned that the adoption of organic fluids often results in an increased complexity of the expander design. One of the first issues arising from the adoption of organic fluids concerns the large density change occurring across the expansion. This density change can be so relevant that, when a turbomachinery is selected as a suitable expander, the centrifugal turbine, in spite of its kinematic disadvantage and work exchange penalty, may be regarded as viable option. In fact, centrifugal turbines, despite the growth of the blade peripheral speed from inlet to outlet of the rotor and hence the work exchange penalty, feature a natural increase of the flow area along the streamwise direction (Pini, Persico, Casati, et al. 2013; Spadacini and Rizzi 2017). This allows compensating the strong density change while maintaining a low meridional velocity, also avoiding excessive blade height growth.

When small power output are considered, volumetric expanders, such as screw, scroll or piston expanders may be regarded as viable and cheap alternative to turbomachines (Lemort et al. 2013; Weiß 2015), particularly if they can be achieved via reversed operation of compressors from refrigeration sector (Zanelli and Daniel 1994). Nevertheless, refrigeration compressors generally exhibit lower compression ratios, making this option not generally viable. Additionally, the expansion ratio handled by volumetric machines is determined by the so-called built-in volume ratio, which is fixed for a given geometry, and additional losses occur, either by over- or under-expansion, when the built-in volume ratio does not match the cycle expansion ratio. If ad hoc designs are considered, the economic profitability is lowered and either multistage arrangement (e.g., for scroll expanders) is often necessary or excessively long stroke may result (as for instance for reciprocating expanders), leading to too large clutter and low foreseeable efficiency (Clemente et al. 2013). Also, an oil separator and additional pumps may be necessary as a result of contact surface lubrication typically required by volumetric expanders.

Conversely, turboexpanders present easier lubrication, better compactness and power density, as well as lightweight and are hence considered promising for small scale applications too (Rahbar et al. 2017), particularly if Radial-Inflow Turbines (RIT) are considered, which are known to provide larger efficiency under larger expansion ratios and were found by Bahamonde, Pini, C. De Servi, et al. (2017) to be the preferred option for small scale ORC applications. In this regard, similar conclusions were also found by Da Lio, Manente, and Lazzaretto (2017) who compared the efficiency map of RIT against the axial turbine one.

This has led to numerous studies investigating ORC turboexpanders for small power applications within 30 kW, e.g., the work by Cappiello and Tuccillo (2020), Fiaschi, Innocenti, et al. (2016), Li et al. (2013), Nguyen, Doherty, and S. B. Riffat (2001), Pei et al. (2011), Pini, Servi, et al. (2017), Robertson et al. (2016), and Turunen-Saaresti, Uusitalo, and Honkatukia (2017) and in 30-50 kW range, e.g., the works by Fiaschi, Manfrida, and Maraschiello (2012) and Kang (2012).

However, the low speed of sound values, which usually characterize organic fluids, often lead supersonic flows within blade passages to arise, often requiring the adoption of convergent divergent vanes (Anand, Vitale, et al. 2018; Cappiello and Tuccillo 2021b; A. P. S. Wheeler and Ong 2013; M. T. White, Markides, and A. I. Sayma 2018), which are unfortunately less flexible than purely converging vanes. Nevertheless, considered the large variability of fluid behaviour, as well as the dependency of optimal working fluid on the heat source to be exploited, the availability of multi-fluid machines would enhance ORC technology penetration in small scale market. This aspect has been investigated by M. T. White, Markides, and A. I. Sayma (2018) who developed a model to predict the margin for working fluid replacement in RIT supersonic nozzles.

Taken into account the large density change occurring along the expansion, the low values of speed of sound and its implications, as well as the non-ideality of the working fluid, it appears clearly that conventional design practice and guidelines developed for turbines operating with ideal gases do not generally hold when ORC applications are considered (Colonna, Casati, et al. 2015; Macchi 2017a). If one also takes into account that the expander is the most critical component from cycle efficiency point of view (Quoilin, Broek, et al. 2013), it appears clearly the need to carry out intensive research on design methods for ORC turbines, so to develop comprehensive design guidelines for turbines operating with organic fluids.

The next chapters of this thesis are devoted to present the design work flow develop in this PhD, ranging from *meanline design* to *3D stator vane* and *3D rotor blade design*, together with the in-house codes developed for these tasks, as well as the analyses conducted by means of Computational Fluid Dynamics (CFD) codes, to answer some research questions concerning design guideline which should be adopted for small scale Radial Inflow Turbines for ORC applications. Finally, conclusions concerning the effect of some design parameters on single components and overall turbine stage efficiency are drawn, also highlighting some knowledge gaps that emerge by the present research activity, which are left as recommended future developments.

CHAPTER 2

Meanline Design

2.1 Introduction

Turbomachinery design is known to be a complex and highly multidisciplinary task characterized by a very large design space with many design variables and constraints.

Nowadays, despite the rapid growth of computational resources occurred over the last years, investigating the effect of each design variable on the turbine performance by means of high accuracy tools –which also have high computational cost– still represents an unbearable effort, because of too large design space. To overcome this issue, the use of so-called *low order* or *low-fidelity* tools in the initial design phase has established itself over the years. This approach relies on neglecting many design variables in the early design steps and evaluating only some design variables. This allows bounding the design, excluding poor or unfeasible designs.

After narrowing down the design space, additional complexity can be added while moving towards higher accuracy tool, in which more features are considered. This procedure also allows to converge faster to a good baseline design, to be optimized in subsequent detailed design phases.

The established design practice is conventionally started by means of the so-called *meanline design*, in which only inlet and outlet sections to each component along the mean streamline are regarded (Dixon and Hall 2013).

At the other end of the design workflow, the high-fidelity tools are present, represented by the CFD-based methods, which can be further subdivided into Euler, RANS, LES and DNS solvers, of increasing computational costs. In this regard, it is worth pointing out that not all of them are applicable to industrial problems because of excessive computational cost.

To bridge from meanline design to CFD, several tools of increasing complexity and accuracy have been developed over the years. These were particularly popular in the past, when computational resources were much more limited than today. Examples of these tools are those based on S1 and S2 surfaces, like streamline curvature methods e.g., the work by Katsanis (1964, 1965, 1966) which also led to the so-called quasi-three-dimensional methods (Bosman and El-Shaarawi ; Fransson et al. 1999) and Bindon and Carmichael (1971), or the so called throughflow methods (Pini, Persico, Casati, et al. 2013).

The major outcomes of meanline codes consist in the velocity triangles together with static and total properties at the inlet and the outlet of each row, as well as the sizing of the blade heights required to handle the design mass flow rate.

However, in order to achieve low computational cost and being the detailed blade shape generally not known at this stage of the design, meanline codes rely on correlations for the loss estimation. On the one hand, this allows the code to achieve a loss evaluation very quickly –without developing a complete blade design. That also makes them particularly suited for the initial bounding of the design space. On the other hand, resorting to correlation can also be regarded as a weakness, as the reliability of the evaluation depends on the appropriate selection of the correlation to use and to the closeness of operative conditions with respect to those of the database used to develop the correlation.

Many different meanline design methods for ideal gases have been presented over the years, both for radial-inflow turbines, e.g., the design and analysis routines by Aungier (2006b,d), and axial turbines, e.g. (Aungier 2006a,c).

Among the very first efficiency prediction methods dealing with RITs working with non-ideal fluids, Perdichizzi and Lozza (1987) proposed a 1D method combined with Radial Equilibrium for the turbine outlet, that was used to investigate the design space via an optimization algorithm. Since then, many other meanline design methods for dense gases have been presented in published literature, e.g., (Fiaschi, Innocenti, et al. 2016; M. White and A. Sayma 2015). Da Lio, Manente, and Lazzaretto (2017) developed a 1D meanline design code, mainly based on the one by Aungier (Aungier 2006b,d), for the preliminary design of an ORC turbine, only accounting for purely convergent blades. The code was exploited to investigate the effect of the specific speed (N_s), velocity ratio, volumetric expansion ratio and size parameter on turbine geometry and total-to-static efficiency, for R245fa only. The optimum N_s does not appear to be a function of the volumetric expansion ratio, but it is much lower (about 25%) than that found for ideal gases, which is in agreement with the results presented by Mounier, Olmedo, and Schiffmann (2018). Moreover, the optimum velocity ratio is found to be a function of volumetric expansion ratio. More specifically, at low volumetric expansion ratio, the optimal velocity ratio is consistent with optimum values for ideal gases. Also, an optimum volumetric expansion ratio was found for a given size parameter, close to onset of choking.

The use of non–dimensional maps for turbine design, such as the one developed by Balje for ideal gases (Balje´ 1962), have been particularly widespread in the past. However, they may arguably not hold for turbomachines expanding dense gases like organic vapours. This issue was investigated by Mounier, Olmedo, and Schiffmann (2018), by means of a 1D code that was used to build ($N_s - D_s$) maps for organic fluids, similarly to the Balje diagram. The iso-efficiency surfaces obtained by Mounier et al. for R134a, R245fa, R152a, R600a, in spite of a similar shape, showed different values with respect to the Balje's one; also resulting in a different fit for optimal specific speed and optimal isentropic efficiency as a function of pressure ratio and specific speed, highlight a change of design requirements when organic fluids are considered.

Another relevant aspect to be considered during the design phase is the off-design operation, which appears particularly relevant for renewable energy-based power plants, as a result of the non-programmable nature of the source. In fact, several meanline code capable to deal with off-design operation have been presented over the years, e.g., the work by Alshammari, Karvountzis-Kontakiotis, et al. (2018) and Meroni et al. (2018).

As mentioned earlier in this section meanline code relies on correlations for loss computation. Hence, if one seeks for an accurate and reliable meanline code, the adopted set of loss correlations is probably one of the most important points to consider. In fact, as shown by Klonowicz et al. (2014), who investigated the influence of loss models choice for an axial turbine stage using different expansion ratios and size parameters, predicted efficiency can differ up to 15 % (especially for low specific speed) and for certain loss models also different trends are predicted. On the other hand, it should also be kept in mind that loss correlations are usually developed on empirical or semi-empirical basis, fitting the results of laboratory tests. Hence, these models strongly depend on test conditions and particular care should be taken upon selecting a suitable loss model.

Despite the fidelity of the loss models is lively to the reliability of the preliminary design, in practice all loss correlation sets have been developed for air, and ideal gases in general, expanding through modest pressure ratios. This makes their applicability to dense vapours doubtful.

To overcome this shortcoming, several attempts have been made to extend well known correlations –originally developed for ideal gases, e.g., air and exhaust gases– to organic fluids expanding through high pressure ratios. To this aim, Persky and Sauret (2019) have reviewed most of the existing correlations for RIT rotor losses – including six components, namely: *incidence, passage, clearance, leaving kinetic energy, trailing edge and windage* losses– and found that the Wei (2014) model outperforms the others. Nonetheless, the authors also proposed a new method obtained as a combination of existing loss correlations, by examining all possible loss model combinations (about 1.5 million). However, the outcome is limited to two working fluids only, namely R134a and CO_2 only.

Despite being applicable only to purely converging nozzle vanes, the most detailed loss model applicable to dense vapours that was found in published literature is the one by Meroni et al. (2018), who tuned calibration coefficients introduced in existing correlations –selected from published literature– via a multi-objective optimization aimed at matching data from open designs from literature characterized by pressure ratios up to 5.8 and air as working fluids. The results were then validated against other test cases including two turbines for ORC power plants. At design point, the method provides an accuracy within 3%, whereas at off-design conditions it diminishes to 5%. Thus, in the present work the methodology proposed by Meroni et al. (2018) is the one adopted for loss evaluation, as it was deemed the one covering most of the requirements for ORC applications, say applicability to different organic fluids, on- and off-design conditions and to higher expansion ratios than other loss models available in literature.

The remaining part of this chapter presents the meanline design code developed in this work, Section 2.2; subsequently, its application to some test cases is shown together with the main results achieved, Section 2.3. Finally, some conclusions are drawn in Section 2.4. The results presented in this chapter provide novel contributions, giving insight into the design space of single stage high expansion ratio – up to about 20 – RITs for ORC application in tens of kW scale. Indeed, for this class of turbines, still scarce information can be found in literature concerning the distributions of the main quantities in the design space, such as absolute and relative Mach numbers, rotor flow turning and rotational speed. The work shown in this chapter resulted in a conference paper (Cappiello and Tuccillo 2020), presented at the 75$^{\text{th}}$ National ATI Congress, and subsequently in an article published in *La Termotecnica* (Cappiello 2021).

2.2 Algorithm Implementation

To investigate the RIT design space and to perform RITs preliminary design, a meanline design code, of which a schematic representation is provided in Fig. 2.1, was implemented in MATLAB environment. While the code computes losses by means of a correlation set from literature (Meroni et al. 2018), the methodology used to perform the turbine sizing has been developed by the author of the present thesis. Particularly, the global structure of the code is similar to the one presented by the author in a previous publication (Cappiello, Tuccillo, et al. 2019), in which potential advantages of axial turbines for turbocharging applications are investigated. However, to account for the different turbine layout, additional design variables have been introduced, as well as other replaced to fit the application considered, say specific speed instead of rotational speed. Additionally, to cope with real gas applications, the program was linked to CoolProp thermodynamic library (I. H. Bell et al. 2014) for the computation of fluid properties.

The code loads the list of turbine boundary conditions, Eqn. 2.1 and decision variables, Eqn. 2.2, and performs the preliminary design of the inlet volute (which is treated as isentropic), vaned stator, stator–rotor interspace gap and rotor; computing thermo–fluid–dynamic properties at mid-span for five stations, namely volute inlet, stator inlet, stator outlet, rotor inlet and rotor outlet.

In a first step, the turbine stage isentropic sizing is performed starting from the rotor and moving upstream towards the volute. This allows to set the intermediate static pressure values, say stator outlet and rotor inlet pressure, which remain fixed during the iterations. Subsequently, a non-isentropic sizing is performed –keeping static pressure values unchanged– based on first-guess loss coefficients for stator, interspace gap and rotor, ζ_N, ζ_{INT} and ζ_R. This approach is preferred to the direct evaluation of losses via correlations as it was found to provide convergence on a larger number of turbine candidates. To understand this one should consider that the very high Mach numbers that arise in the isentropic sizing may lead to dramatically large enthalpy loss coefficients. When the enthalpy loss becomes greater than the available isentropic kinetic energy the calculation is stopped and the design under investigation is scrapped. Conversely, the approach adopted in this work makes this circumstance less likely to arise and hence avoids to unnecessarily scrap design candidates.

Once the first non-isentropic sizing has been performed, losses are computed according to the correlations by Meroni et al. (2018), allowing the estimation of kinetic loss coefficients for each component. These are then compared to the first guess values and, if convergence is not achieved on the the three coefficients, an iterative loop is established up to convergence on ζ_N, ζ_{INT} and ζ_R. Finally, once convergence is achieved, the code allows to determine stator and rotor flow and metal angles, together with radius and passages heights, blade and vane counts, as well as thermo-fluid-dynamic properties at each station, such as velocity, pressure, temperature, density, Mach numbers, power and efficiency values.

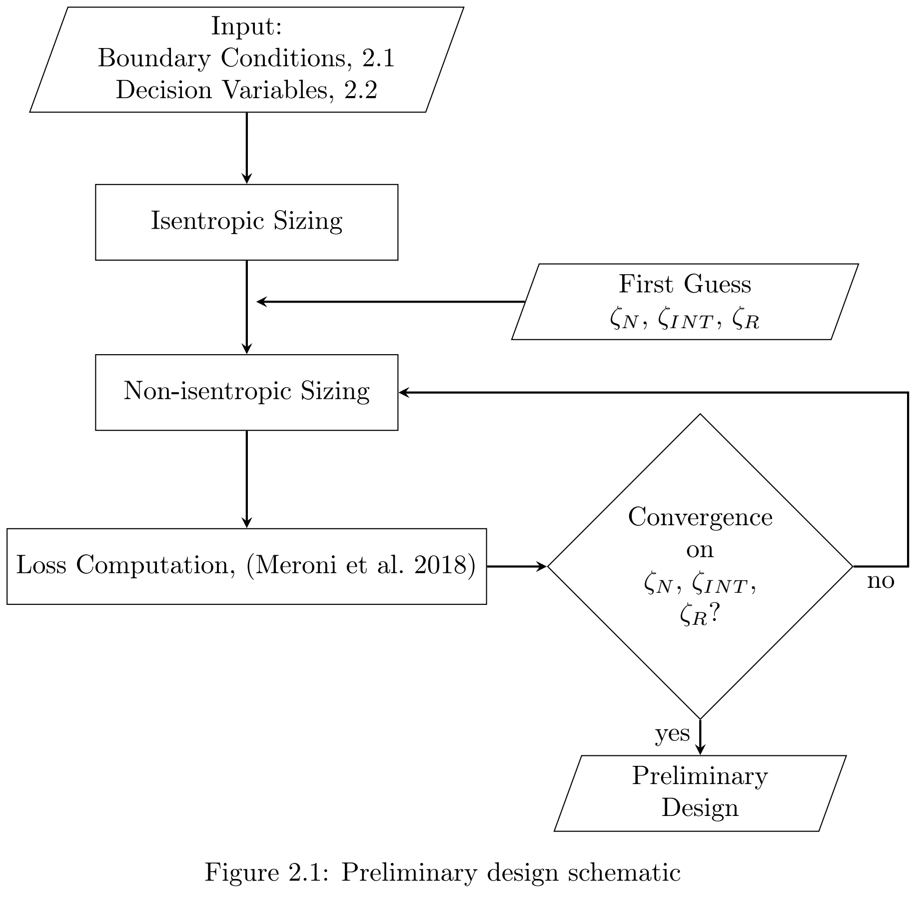

Figure 2.1: Preliminary design schematic

$$\text{Boundary Conditions} = \Big\{\dot{m}, \quad p_{01}, \quad T_{01}, \quad p_5, \quad \text{Fluid}\Big\} \tag{2.1}$$

$$\begin{aligned}\text{Decision Variables} = \Big\{ & R_p = \frac{p_4 - p_5}{p_{01} - p_5}, \quad \frac{c_{m,5}}{c_{m,4}}, \quad \frac{R_{5,mid}}{R_4}, \\ & N_s = \omega \frac{\sqrt{\dot{V}_{5,is}}}{\left(h_{01} - h_{5,is}\right)^{3/4}}, \quad \alpha_2, \quad \alpha_4, \\ & \Delta \left(U_4/c_4\right)_{opt} = \Delta \left(\frac{\sin\alpha_4}{2} + \frac{R^*}{2 + (1 - R^*)\sin\alpha_4}\right), \\ & N_N, \quad \frac{R_2}{R_3}, \quad \frac{R_3}{R_4}\Big\}\end{aligned} \tag{2.2}$$

Concerning the construction of a 3D geometry, it shall be reminded that the meridional channel contour and camberline are required at least at hub and shroud. Therefore, metal angles are needed at these two spans. For radial turbines, while rotor leading edge metal angle is often taken constant along the blade span, the same cannot be said for the trailing edge metal angle. Thus, once a converged preliminary design is achieved, Isentropic Simple Radial Equilibrium (ISRE) is applied at rotor exit imposing a free-vortex distribution for tangential velocity component. This allows the computation of flow angles at hub and shroud, which in turn provide the metal angles via the deviation angles.

Following, the main steps of *Isentropic* and *Non-Isentropic Sizing* are presented in Sects. 2.2.1. and 2.2.2

2.2.1 Isentropic Sizing

First of all, to enable the non-isentropic sizing, static pressure values at stations 4, 3 and 2 (i.e., rotor inlet, stator outlet and stator inlet, respectively) must be determined. For this purpose, different approaches are used in the work. The computation of the static pressure at rotor inlet, p_4, is rather straightforward, as it can be computed directly from Boundary Conditions, Eqn. 2.1, and Decision Variables, Eqn. 2.2, via Eqn. 2.3:

$$p_4 = p_5 + R_p \cdot (p_{01} - p_5) \tag{2.3}$$

The rotational speed, ω, can also be computed directly from Boundary Conditions and Decision Variables by means of Eqn. 2.4, in which the entropy s_1 is defined as in Eqn. 2.5

$$\omega = N_s \cdot \frac{\left[\, h_{01} - h(\, p_5,\ s_1\,)\,\right]^{3/4}}{\left[\frac{\dot{m}}{\rho(\, p_5,\ s_1\,)}\right]^{1/2}} \tag{2.4}$$

$$s_1 = s(\, h_{01},\ p_{01}\,) \tag{2.5}$$

Subsequently, the well-known relationship to compute the optimal value of the ratio (U_4/c_4), that is, the one that minimizes the kinetic energy loss at rotor outlet, is adopted, Eqn. 2.6. For this equation the isentropic degree of reaction, R^*, can be found via Eqn. 2.7.

$$(U_4/c_4)_{opt} = \left(\frac{\sin\alpha_4}{2} + \frac{R^*}{2 + (1 - R^*)\sin\alpha_4}\right) \tag{2.6}$$

$$R^* = \frac{h(\, p_4,\ s_1\,)\ - h(\, p_5,\ s_1\,)}{h_{01} - h(\, p_5,\ s_1\,)} \tag{2.7}$$

Therefore, the actual value of (U_4/c_4) to be used can be computed as in Eqn. 2.8, based on the deviation from the optimal value, $\Delta\,(U_4/c_4)_{opt}$, prescribed as a decision variable.

$$(U_4/c_4) = (U_4/c_4)_{opt} + \frac{\Delta\,(U_4/c_4)_{opt}}{100} \cdot (U_4/c_4)_{opt} \tag{2.8}$$

Being the isentropic absolute velocity at rotor inlet, $c_{4,is}$, defined as in Eqn. 2.9, the rotor inlet peripheral speed, $U_{4,is}$, and the corresponding radius, R_4, can be computed by means of Eqs. 2.10 and 2.11, respectively.

$$c_{4,is} = \sqrt{2 \cdot (h_{01} - h(\, p_4,\ s_1\,))} \tag{2.9}$$

$$U_4 = (U_4/c_4) \cdot c_{4,is} \tag{2.10}$$

$$R_4 = U_4/\omega \tag{2.11}$$

Finally, the rotor inlet blade height, b_4, can be found by means of Eqn. 2.12:

$$b_4 = \frac{\dot{m}}{2\pi R_4 \rho(\, p_4,\ s_1\,) c_{4,is} \cos\alpha_4} \tag{2.12}$$

At this point, the isentropic sizing of the stator-rotor interspace can be performed, so as to retrieve the static pressure at stator outlet, p_3. First of all, the vane outlet radius, R_3, is computed by means of the decision variable $\frac{R_3}{R_4}$, according to Eqn. 2.13, whereas the vane outlet height, b_3, is set equal to the one at rotor inlet, Eqn. 2.14.

$$R_3 = \frac{R_3}{R_4} \cdot R_4 \tag{2.13}$$

$$b_3 = b_4 \tag{2.14}$$

This allows the computation of $c_{\theta 3,is}$, according to Eqn. 2.15.

$$c_{\theta 3,is} = c_{4,is} \sin \alpha_4 \cdot \frac{R_4}{R_3} \tag{2.15}$$

To retrieve the static pressure p_3, an iterative procedure on the value of the ρ_3 is adopted, following the schematic depicted in Fig. 2.2. The process is started by means of a guess value for the static density at station 3, ρ_{guess}. This value is used to solve the system of Eqns. 2.16, which provides a value of the static enthalpy h at station 3. At this point, a new value of the static density, ρ_{New}, –corresponding to the static enthalpy, h, and the inlet entropy s_1– is computed. The value of ρ_{New} is compared against the one found in the previous iteration and, if convergence is not reached, the system of Eqns. 2.16 is solved again using the latest value of ρ_{New}. This establishes an iterative loop on the value of the static density. Once convergence on density value ρ is achieved, the static pressure at station 3, p_3, is computed by means of the last ρ_{New} and the inlet entropy s_1.

Similarly to the computation of the static pressure p_3, the static pressure at nozzle inlet, p_2, is determined iteratively. First of all, the vane height at nozzle inlet is set according to Eqn. 2.17, determining a constant vane height from inlet to outlet of the row.

$$b_2 = b_3 \tag{2.17}$$

The nozzle inlet radius, R_2, is instead computed by means of the design variable $\frac{R_2}{R_3}$, according to Eqn. 2.18.

$$R_2 = R_3 \cdot \frac{R_2}{R_3} \tag{2.18}$$

This allows to start the iterative procedure for p_2 computation. In this regard, the same procedure drawn in Fig. 2.2 is adopted, although, being α_2 a decision variable, c_2 is computed according to Eqn. 2.19:

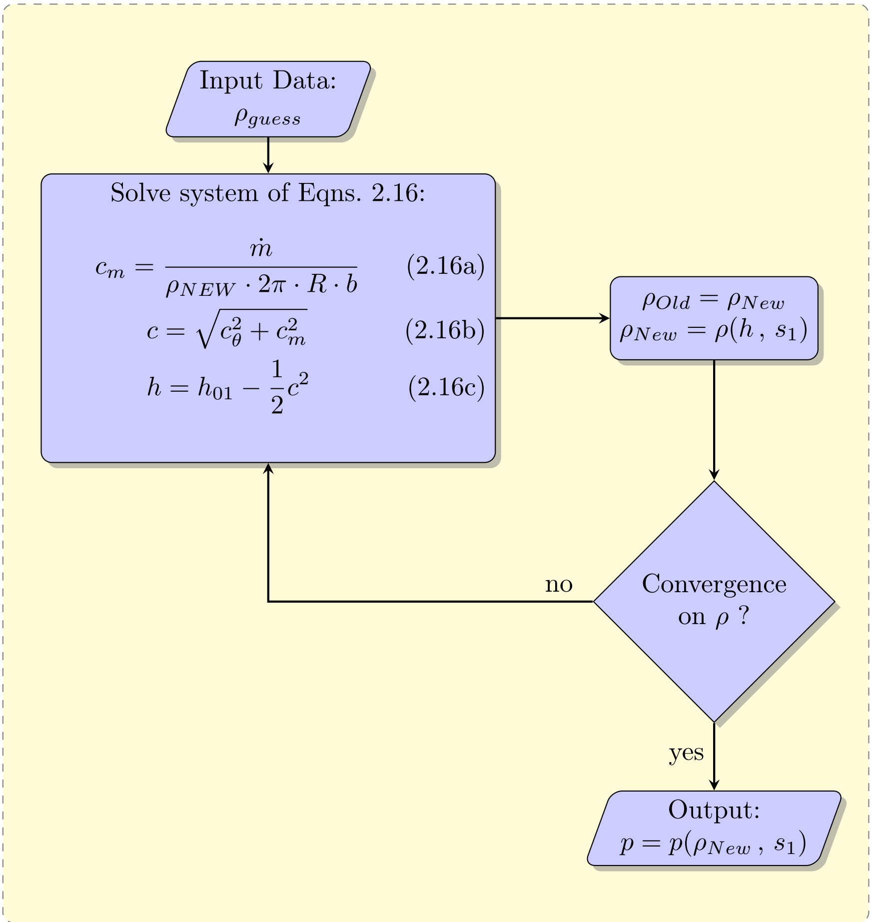

Figure 2.2: Iterative procedure used to retrieve the static pressure at stator-rotor gap inlet and stator inlet

$$c_2 = \frac{c_{m2}}{\cos \alpha_2} \tag{2.19}$$

Once again, the procedure is started providing a first guess static density value, that is used for the solution of the system of Eqns. 2.16, modified to account for Eqn. 2.19. The solution of the system provides a static enthalpy value, h, that is used to compute a new value of the static density, ρ_{New}. This value can be used to establish an iterative loop up to convergence on the static density. Once convergence is reached, the static pressure at station 2, p_2 is computed by means of the last ρ_{New} and s_1.

2.2.2 Non-Isentropic Sizing

Once the static pressure values at each of turbine stations are known, the static enthalpy values at nozzle outlet and interspace gap outlet –reached after the real expansion process– can be computed by means of the kinetic loss coefficients, ζ_N and ζ_{INT} (Eqns. 2.20), according to Eqns. 2.21.

$$\zeta_N = \frac{h_3 - h(p_3, s_2)}{0.5 \cdot c_{3,is}^2} \tag{2.20a}$$

$$\zeta_{INT} = \frac{h_4 - h(p_4, s_3)}{0.5 \cdot c_{4,is}^2} \tag{2.20b}$$

$$h_3 = h(p_3, s_2) + 0.5\ \zeta_N \cdot [2\ (h_{01} - h(p_3, s_2))] \tag{2.21a}$$

$$h_4 = h(p_4, s_3) + 0.5\ \zeta_{INT} \cdot [2\ (h_{01} - h(p_4, s_3))] \tag{2.21b}$$

Depending on whether the first or a subsequent design iteration is considered, the kinetic loss coefficients are either first guess values or computed by means of the correlation set by Meroni et al. (2018), respectively.

It is also worth recalling that the volute is treated as isentropic, therefore:

$$h_2 = h(p_2, s_1) \tag{2.22a}$$

$$s_2 = s1 \tag{2.22b}$$

With reference to the velocity triangles schematic and nomenclature reported in Fig. 2.3, the rotor inlet velocity triangle is built first. The absolute velocity at rotor inlet, c_4, can be computed via total enthalpy conservation as in Eqn. 2.23, from which the blade peripheral speed at rotor inlet is computed by means of Eqn. 2.24, considering $\left(\frac{U_4}{c_4}\right)$ found in the isentropic sizing, Eqn. 2.8.

$$c_4 = \sqrt{2\,(h_{01} - h_4)} \tag{2.23}$$

$$U_4 = c_4 \left(\frac{U_4}{c_4}\right) \tag{2.24}$$

Therefore, the rotor inlet and outlet radii R_4 and $R_{5,mid}$ were computed according to Eqns. 2.25 and 2.26.

$$R_4 = \frac{U_4}{\omega} \tag{2.25}$$

$$R_{5,mid} = R_4 \left(\frac{R_{5,mid}}{R_4}\right) \tag{2.26}$$

Subsequently, the rotor inlet relative velocity was computed according to Eqns. 2.27.

$$w_{\theta 4} = c_4 \sin\alpha_4 - U_4 \tag{2.27a}$$

$$w_{m4} = c_4 \cos\alpha_4 \tag{2.27b}$$

$$w_4 = \sqrt{w_{\theta 4}^2 + {w_{m4}}^2} \tag{2.27c}$$

To compute the static enthalpy at rotor outlet, h_5, the rotor inlet rothalpy, I_4, was computed according to Eqn. 2.28. Therefore, by means of rothalpy conservation, $I_4 = I_5$, one can write $w_{5,is}$ as in Eqn. 2.29, that enables the computation of h_5 by means of Eqn. 2.30 as a function of the rotor kinetic loss coefficient ζ_R.

$$I_4 = h_4 + \frac{1}{2}\,w_4^2 - \frac{1}{2}\,U_4^2 \tag{2.28}$$

$$w_{5,is} = \sqrt{2 \cdot \left(I_4 - h(p_5, s_4) + \frac{1}{2}\,(R_5 \cdot \omega)^2\right)} \tag{2.29}$$

$$h_5 = h(p_5, s_4) + \frac{1}{2} \cdot \zeta_R \cdot w_{5,is}^2 \tag{2.30}$$

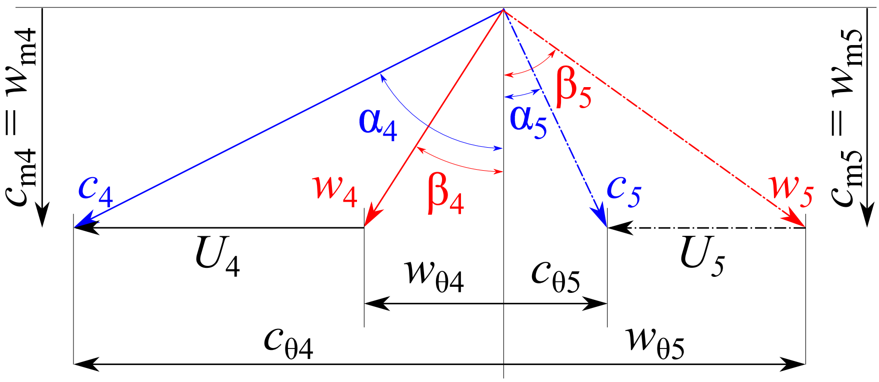

Figure 2.3: Schematic representation of velocity triangles and velocity components

Thus, the rotor outlet velocity triangle at mid-span can be built by means of Eqns. 2.31.

$$w_5 = \sqrt{2\left(I_4 - h_5 + \frac{1}{2}\left(R_5 \cdot \omega\right)^2\right)} \tag{2.31a}$$

$$c_{m5} = c_4 \cdot \cos\alpha_4 \cdot \left(\frac{c_{m5}}{c_{m4}}\right) \tag{2.31b}$$

$$w_{m5} = c_{m5} \tag{2.31c}$$

$$\beta_5 = -\arccos\frac{w_{m5}}{w_5} \tag{2.31d}$$

$$w_{\theta 5} = w_5 \sin\beta_5 \tag{2.31e}$$

$$c_{\theta 5} = w_{\theta 5} + U_5 \tag{2.31f}$$

$$c_5 = \sqrt{c_{\theta 5}^2 + c_{m5}^2} \tag{2.31g}$$

Therefore, the rotor inlet and outlet blade heights, shown in the meridional channel schematic provided in Fig.2.4, can be computed by mass conservation, as in Eqns. 2.32, which also allows to compute tip and hub radii at rotor outlet, Eqns. 2.33.

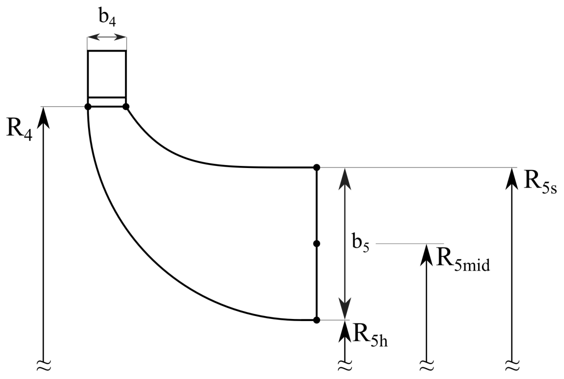

Figure 2.4: Meridional channel schematic

$$b_4 = \frac{\dot{m}}{2\pi \cdot R_4 \cdot \rho_4 \cdot c_{m4}} \tag{2.32a}$$

$$b_5 = \frac{\dot{m}}{2\pi \cdot R_{5,mid} \cdot \rho_5 \cdot c_{m5}} \tag{2.32b}$$

$$R_{5h} = R_{5,mid} - \frac{b_5}{2} \tag{2.33a}$$

$$R_{5s} = R_{5,mid} + \frac{b_5}{2} \tag{2.33b}$$

Rotor outlet velocity triangles at hub and shroud are subsequently computed to determine the blade angles at these sections. To do so, the Isentropic Simple Radial Equilibrium (ISRE) –that implies $\frac{ds}{dR} = 0$– is used for the rotor outlet, imposing a free-vortex distribution. The $\frac{ds}{dR} = 0$ assumption allows to neglect the meridional velocity component change over the blade span at rotor outlet. However, if very long blade heights are considered, larger discrepancies can arise toward the blade hub and tip. The free-vortex constant κ is computed at mid-span, by means of Eqn. 2.34, and the velocity components at hub and shroud are then calculated according to Eqns. 2.35, while standard trigonometry is used to determine the flow angles.

$$\kappa = c_{\theta 5} \cdot R_{5,mid} \tag{2.34}$$

$$c_{\theta 5s} = \kappa / R_{5s} \tag{2.35a}$$
$$c_{\theta 5h} = \kappa / R_{5h} \tag{2.35b}$$

$$U_{5s} = R_{5s} \cdot \omega \tag{2.35c}$$
$$U_{5h} = R_{5h} \cdot \omega \tag{2.35d}$$

$$w_{\theta 5s} = c_{\theta 5s} - U_{5s} \tag{2.35e}$$
$$w_{\theta 5h} = c_{\theta 5h} - U_{5h} \tag{2.35f}$$

$$c_{5s} = \sqrt{c_{\theta 5s}^2 + c_{m5}^2} \tag{2.35g}$$
$$c_{5h} = \sqrt{c_{\theta 5h}^2 + c_{m5}^2} \tag{2.35h}$$

$$w_{5s} = \sqrt{w_{\theta 5s}^2 + w_{m5}^2} \tag{2.35i}$$
$$w_{5h} = \sqrt{w_{\theta 5h}^2 + w_{m5}^2} \tag{2.35j}$$

Typically, an output of the preliminary design is an estimation of the optimal rotor blade count. The latter is computed in the code by means of a correlation proposed by Rohlik (1968), Eqn. 2.36 (adapted to the sign convention and reference system adopted in the present thesis), based on the empirical work by Jamieson (1955). The value obtained from Eqn. 2.36 should be rounded to the closest integer.

$$Z_R = 12 + 0.03 \cdot [33 - (90 - \alpha_4)]^2 \tag{2.36}$$

Once the rotor has been sized, the code proceeds upstream, sizing the stator-rotor interspace gap. Radial gap inlet width b_3 and inlet radius R_3 are computed as for the isentropic sizing, Eqns. 2.14 and 2.13, whereas for the non-isentropic absolute tangential velocity component $c_{\theta 3}$ a more complex approach is followed. In this regard, Eqn. 2.37 –in which C_f is the skin friction coefficient– was used. This equation is base on the analysis by Stanitz (1952), as reported by Meroni et al. (2018).

$$c_{\theta 3} = c_{\theta 4} \cdot \left(\frac{R_4}{R_3} + \frac{2\pi \cdot C_f \cdot \rho_4 \cdot c_4 \cdot \sin\alpha_4 \cdot (R_3^2 - R_3 R_4)}{\dot{m}} \right) \tag{2.37}$$

The skin friction coefficient C_f was computed according to the formulation proposed by Japikse (1982), Eqn. 2.38. The value of ι can vary in the range 0.005 – 0.02; however, the recommended value of 0.01 was used.

$$C_f = \iota \cdot \frac{1.8 \cdot 10^5}{Re_{INT}^{0.2}} \tag{2.38}$$

The Reynolds number at the exit of the stator-rotor interspace Re_{INT} was computed according to Eqn. 2.39, in which μ_4 is the dynamic viscosity at stator-rotor gap outlet and D_{h4} is the hydraulic diameter, computed as in Eqn. 2.40, according to Brown (1947).

$$Re_{INT} = \frac{\rho_4 \cdot c_4 \cdot D_{h4}}{\mu_4} \tag{2.39}$$

$$D_{h4} = \frac{4 \cdot (2\pi R_4 b_4 \sin\alpha_4)}{2 \cdot (2\pi R_4 \sin\alpha_4)} = 2 \cdot b_4 \tag{2.40}$$

Gap inlet meridional velocity c_{m3} is instead computed by means of mass conservation, Eqn. 2.41.

$$c_{m3} = \frac{\dot{m}}{2\pi \cdot R3b3\rho_3} \tag{2.41}$$

After the stator-rotor gap sizing, the code proceeds with the nozzle sizing, for which inlet vane height b_2 and inlet radius R_2 are computed as for the isentropic case, Eqn. 2.17 and 2.18. The knowledge of the nozzle inlet radius R_2 allows to compute the radial chord $Chord_R = R_2 - R_3$, from which the true chord can be estimated by means of Eqn. 2.42, using an approximate stagger angle, ϵ, found taking the average of inlet and outlet angles to the nozzle. Therefore, the nozzle spacing, o, and the vane count, Z_N, can be found by means of the true chord and the nozzle solidity N_N, that is a decision variable, Eqn. 2.43.

$$Chord = \frac{Chord_R}{\cos\epsilon} \tag{2.42}$$

$$o = \frac{Chord}{N_N} \tag{2.43a}$$

$$Z_N = \frac{2\pi R_2}{o} \tag{2.43b}$$

Finally, the absolute meridional velocity component at nozzle inlet c_{m2} is found by means of mass conservation, whereas the absolute velocity c_2 is computed by means of Eqn. 2.19, like in the isentropic case.

Once the nozzle has been sized, the code performs the volute sizing iteratively following the schematic representation provided in Fig. 2.5. To do so, a circular section, external volute is considered. First of all, a guess value for R_1 –the radius at which the volute inlet section center lays– is assumed. This value is used as input to solve Eqns. 2.44, retrieving the radius of the volute inlet section $R_{1\,Sec}$. This value is used to recompute the radius of the inlet section center R_1 and, if convergence on R_1 is not achieved, an iterative loop is established. After convergence, the R_1 value is provided and the turbine sizing is complete.

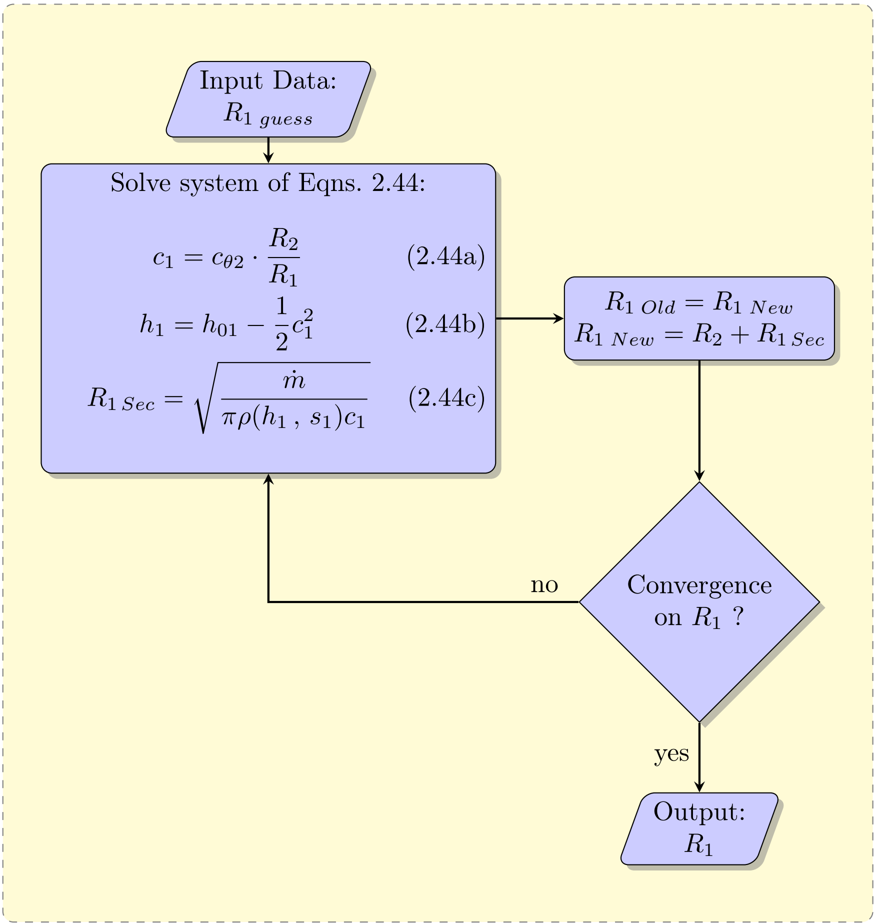

Figure 2.5: Iterative procedure used to perform the inlet volute section sizing

2.3 Application

The present section illustrates the results of a parametric analysis carried to investigate the design space of a Radial-Inflow Turbine for a bottoming ORC power plant for a Waste Heat Recovery application. Particularly, in Subsection 2.3.1 the test case boundary conditions and the results of the parametric analysis are presented, whereas in Subsection 2.3.2 the results of the meanline design are validated against 3D steady-state CFD calculation.

2.3.1 Meanline Design and Parametric Analysis

The meanline design code presented in Section 2.2 was used to investigate the design space of an ORC Radial-Inflow Turbine for WHR from a 30 kW solar assisted micro Gas Turbine (mGT). Within this scenario, three Test Cases (TC), reported in Tab. 2.1, featuring different operating conditions and fluids, are considered. These boundary conditions have been obtained by means of the thermodynamic model of the whole plant –implemented in THERMOFLEX software– aiming at overall plant power output maximization. As it can be noticed from Tab. 2.1, two different organic fluids are considered, particularly one refrigerant, i.e., the R245fa, and one siloxane, i.e., the MM. It is also worth noting that for the first and third cases, pressure and volume expansion ratios are very large, while the second test case shows milder expansion ratio, although still rather large if compared to more conventional applications like turbocharger turbines. In fact, the second test case was obtained from the first one reducing the total inlet pressure and temperature while increasing the design mass flow rate –so to provide the same isentropic power, P_{is}. This choice was done with the aim of providing data for comparing the effect of expansion ratios both on achievable turbine efficiency and turbine requirements in terms of thermo-fluid-dynamic properties and size.

For each one of the test cases in Tab. 2.1 a parametric analysis was carried out varying the most relevant decision variables in the ranges reported in Tab. 2.2, selected according to the usual range assumed by these quantities. Particularly, assuming the deviation from the optimal kinematic ratio equal to zero, $\Delta\left(U_4/c_4\right)_{opt} = 0$, despite narrowing the investigated portion of the design space, is not expected to compromise the results since optimal turbine designs are generally feature $\Delta\left(U_4/c_4\right)_{opt} \approx 0$.

Nevertheless, the range adopted for the Pressure-Based Degree of Reaction, R_p, was selected so as to allow the Degree of Reaction R^* to span its typical range. It is also worth pointing out that in the three test cases the rotational speed of the turbine was not constrained. Instead, it was retrieved from the specific speed, N_S. This approach is consistent with the assumption of the ORC turbine being connected to its own electrical generator and hence allowed to spin at a different rotational speed with respect to the turbine of the mGT. The remaining decision variables, Eqn. 2.2, have been set to values attaining to typical ranges assumed by these quantities.

Finally, the results have been used to build design maps as a function of Flow Coefficient, Φ, Eqn. 2.45, and Work Coefficient, Ψ, Eqn. 2.46, Figs. 2.6–2.20.

$$\Phi = \frac{c_{\mathrm{m,5\ is}}}{U_4} \tag{2.45}$$

$$\Psi = \frac{\Delta h_{\mathrm{TS,\ is}}}{U_4^2} \tag{2.46}$$

TC (-)	Fluid (-)	p_{01} (bar)	T_{01} (K)	p_5 (bar)	$\dot{m}$ (kg/s)	Π_{TS} (-)	ρ_{01}/ρ_5 (-)	P_{is} (kW)	$\Delta h_{TS,is}$ (kJ/kg)
1	R245fa	28.00	439.15	2.162	0.4920	12.95	14	26.89	54.65
2	R245fa	10.81	403.28	2.162	0.7690	5.00	5	26.89	34.97
3	MM	18.00	579.75	1.020	0.2460	17.65	21	18.24	74.16

Table 2.1: Turbine boundary conditions for the three test cases considered

Decision Variable	Symbol	Range
Pressure-Based Degree of Reaction	R_p	0.025 - 0.6
Rotor Radius Ratio	$R_4/R_{5,mid}$	0.3 - 0.7
Meridional Velocity Ratio	$c_{m,5,mid}/c_{m,4}$	1.0 – 1.4
Specific Speed	N_S	0.1 – 1.0
Deviation from Optimal Kinematic ratio	$\Delta\left(U_4/c_4\right)_{opt}$	0
Stator Inlet Flow Angle	α_2	45°
Rotor Inlet Flow Angle	α_4	75°
Nozzle Solidity	N_N	1.20
Stator Radius Ratio	R_2/R_3	1.10
Vaneless Interspace Radius Ratio	R_3/R_4	1.02

Table 2.2: Decision variable ranges for parametric analyses

Figure 2.6 shows for the three test cases the distribution of the total-to-static efficiency, η_{TS}, computed according to Eqn. 2.47, as a function of flow and work coefficients.

$$\eta_{TS} = \frac{h_{01} - h_{05}}{h_{01} - h(p_5,\, s_1)} \tag{2.47}$$

As one can notice, regular trends are achieved in the whole design space for the three test cases, with the η_{TS} values smoothly decreasing towards the edge of the investigated region. The largest total-to-static efficiency is achieved for the second test case, Fig. 2.6b, which also exhibits larger area of high total-to-static efficiency. Conversely, the lowest peak efficiency is detected for the third case, Fig. 2.6c, while the first test case, Fig. 2.6a, lays in between.

Likewise, similar trends can be detected in Fig. 2.7, which presents the total-to-total efficiency, η_{TT}, distribution within the design space, computed according to Eqn. 2.48.

$$\eta_{TT} = \frac{h_{01} - h_{05}}{h_{01} - h(p_{05},\, s_1)} \tag{2.48}$$

These trends appear consistent with the operating conditions of each of the three test cases, Tab. 2.1, as the second test case actually features the lowest volumetric expansion ratio, i.e., 5, and the larger mass flow rate, which inevitably results in a larger machine operating in less challenging conditions. On the other hand, the third turbine is characterized by the smallest mass flow rate and the highest volumetric expansion ratio, i.e., 21, establishing particularly challenging working conditions.

Figure 2.8 presents the contour of the Degree of Reaction, R^*, for the three test cases, together with the superposition of the locus of maximum of total-to-static efficiency with dash-dotted line. As one can notice, the optimal total-to-static efficiency ranges in the low-medium range of degree of reaction, namely $0.15 - 0.40$ for Test Case 1 and 3, while slightly larger values can be observed for the second test case, namely $0.2 - 0.45$.

Another relevant information that can be retrieved from the meanline design concerns the Mach number value reached at the entrance and exit of each row. This aspect is particularly crucial when single stage turbines for ORC power plant are considered as a consequence of several features presented in Sections 1.2–1.3, namely the the large molecular weight of organic fluids –that in turn leads to low speed of sound values– and the large expansion ratio. Particularly, the need to handle the entire expansion ratio

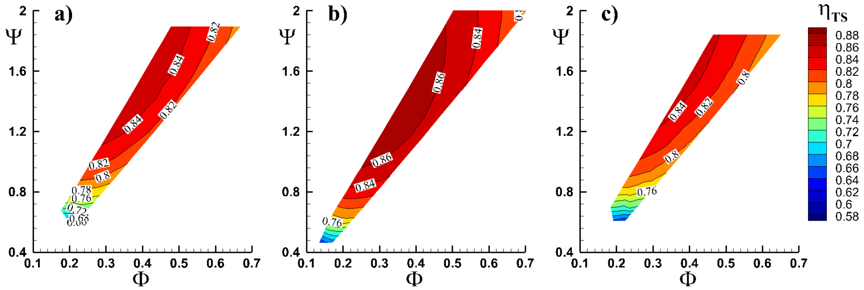

Figure 2.6: Total-to-Static efficiency contour: (a) Test Case 1; (b) Test Case 2; (c) Test Case 3.

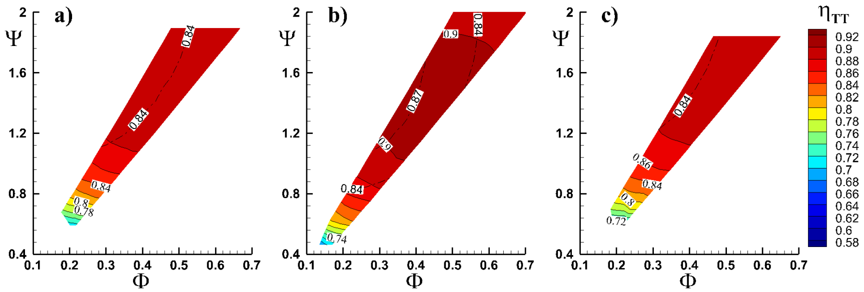

Figure 2.7: Total-to-Total efficiency contour: (a) Test case 1; (b) Test Case 2; (c) Test Case 3. Locus of maximum total-to-static efficiency with dash-dotted line.

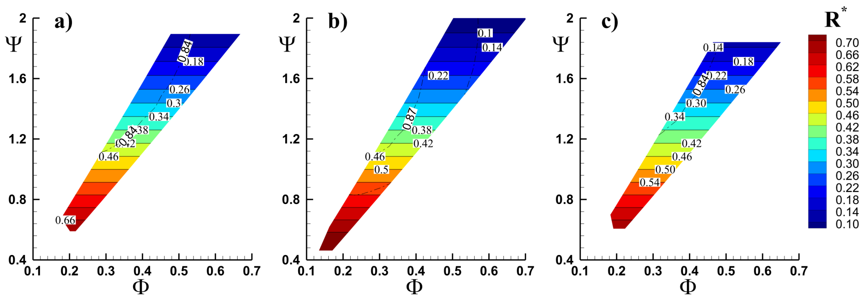

Figure 2.8: Degree of Reaction contour: (a) Test case 1; (b) Test Case 2; (c) Test Case 3. Locus of maximum total-to-static efficiency with dash-dotted line.

in a single stage pushes the design towards low reaction stages, which in turn results in high kinetic energy at stator discharge. The latter, combined with the low speed of sound values, generally determines high Mach number values at stator discharge and its values should be carefully checked from the early steps of the design in order to insure the feasibility of the project.

Figure 2.9 presents the contour of the absolute Mach number at rotor inlet as a function of flow and work coefficients, together with the superposition of the highest iso-η_{TS} curve with dash-dotted line. As it can be noticed, the absolute Mach, M_4, presents highly variable levels, both within the design space and from test case to test case. The best efficiency curves can be seen to cross very different levels of absolute Mach, M_4, ranging from low supersonic to high supersonic flow condition. Particularly, in test case 2 lower values are encountered –consistently with the lower expansion ratio, for which purely convergent vanes can be adopted. Conversely, much higher values are detected in the first and third test case, making the adoption of convergent-divergent vanes mandatory. These trends are substantially driven by those of the degree of reaction, Fig. 2.8, in fact, the lower the degree of reaction, the larger the absolute Mach number at rotor inlet, Fig. 2.9 –and hence at stator outlet– as a result of large enthalpy drop share being handled in the stator.

It is well known that a good turbine design practice consists in keeping the relative Mach number at rotor inlet subsonic. The latter allows to achieved a better efficiency at design point, gain larger flexibility in the off-design operation and simplify the rotor design. Figure 2.10 shows the contour of the relative Mach number at rotor inlet for the three test cases as a function of flow and work coefficients. First of all, for all the test cases investigated, most of the design space is characterized by subsonic rotor inlet conditions. Secondly, the superposition of the best efficiency curve allows to ensure that large margin exists, since several design candidates allows achieving the maximum efficiency while keeping a subsonic rotor inlet.

Figure 2.11 presents for the three test cases the relative Mach number at rotor outlet, $M_{5,R}$, with the superposition of the locus of maximum of the total-to-static efficiency with dash-dotted line. Once again, the trends are determined by those of the degree of reaction, Fig. 2.8: in fact, as the degree of reaction increases larger and larger shares of the enthalpy drop are handled in the rotor passages, therefore leading to higher expansion taking place in the rotor channels and larger relative Mach number at rotor discharge. However, for the test cases analysed the best efficiency regions attain to design candidates which provides rotor discharge conditions well within the subsonic flow regime.

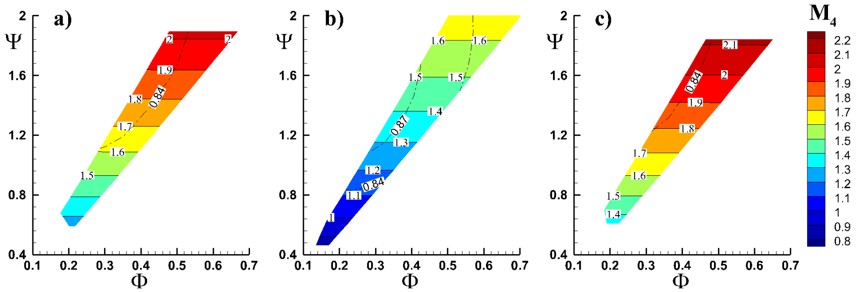

Figure 2.9: Rotor inlet absolute Mach number contour: (a) Test case 1; (b) Test Case 2; (c) Test Case 3. Locus of maximum total-to-static efficiency with dash-dotted line.

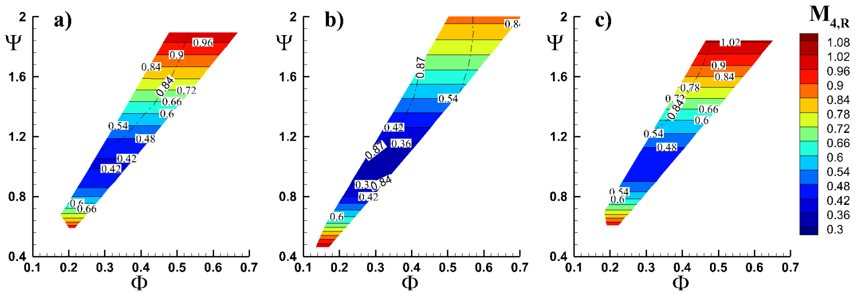

Figure 2.10: Rotor inlet relative Mach number contour: (a) Test case 1; (b) Test Case 2; (c) Test Case 3. Locus of maximum total-to-static efficiency with dash-dotted line.

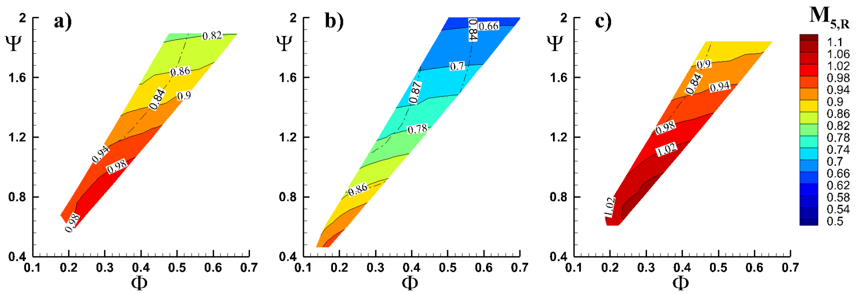

Figure 2.11: Rotor outlet relative Mach number contour: (a) Test case 1; (b) Test Case 2; (c) Test Case 3. Locus of maximum total-to-static efficiency with dash-dotted line.

Figure 2.12 presents the distribution of the rotor inlet flow angle in the relative frame of reference, β_4, for the three test cases with the superposition of the best efficiency curve with dash-dotted line. As one can see, β_4 mainly follows the trends of the degree of reaction, Fig. 2.8, although its values strongly affects the rotor inlet flow angle. In fact, for higher degree of reaction, $0.4 - 0.5$, the optimal inlet flow angles tend to the meridional direction, while $\beta_4 = 50 - 50°$ attains to low degree of reaction, $0.1 - 0.15$. Also, the minimum rotor inlet flow angle required for maximum efficiency increases as the expansion ratio increases, moving from about 0° for the second test case to about 30° for first and third test case. In other words, an increase of the expansion ratio shifts the best iso-efficiency line towards higher inlet flow angles.

Figure 2.13 shows the distribution of the rotor outlet flow angle in the relative frame of reference, β_5, once again with the superposition of the optimal total-to-static efficiency curve. The trend is a direct result of the assumption on the optimal kinematic ratio $\left(\frac{U_4}{c_4}\right)_{opt}$. More specifically, the assumption of zero deviation from the optimal kinematic ratio, $\Delta\left(\frac{U_4}{c_4}\right)_{opt} = 0$ Tab. 2.2, ensure that in the isentropic sizing the rotor outlet velocity in the absolute frame of reference is axial. To match this constraint, an increase of the flow coefficient Φ entails a reduction of the absolute value of the rotor relative outlet flow angle, $|\beta_5|$. In other words, an increase of the flow coefficient Φ leads the rotor relative outlet velocity to turn toward the meridional direction.

The combination of β_4 and β_5 trends determine the overall flow turning to be made within the rotor preliminary design, which is shown in Fig. 2.14, where one can see that low flow turning is required in the bottom part of the design space, while progressively larger values are needed moving towards high work coefficients.

Figure 2.15 shows the contour of turbine rotational speed, Ω, as a function of flow and work coefficients, together with the superposition of the optimal efficiency curve. In this regard, it is worth to remind that in the present parametric analysis the rotational speed was not constrained to a specific value, therefore, it is an outcome of the analysis itself. As one can see from Fig. 2.15, larger values are observed in the first and third test cases, 50-120 krpm and 60-130 krpm, respectively, while lower values are detected for the second test case, i.e., 30-65 krpm. Moreover, the optimal efficiency curves can be seen to span across very different rotational speed values depending on the test case considered: again, higher values are detected for first and third test cases, while lower values can be seen for the second one.

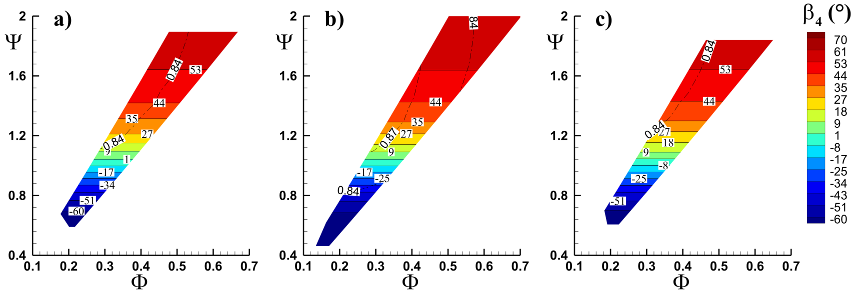

Figure 2.12: Contour of the rotor inlet flow angle in the relative frame of reference: (a) Test case 1; (b) Test Case 2; (c) Test Case 3. Locus of maximum total-to-static efficiency with dash-dotted line.

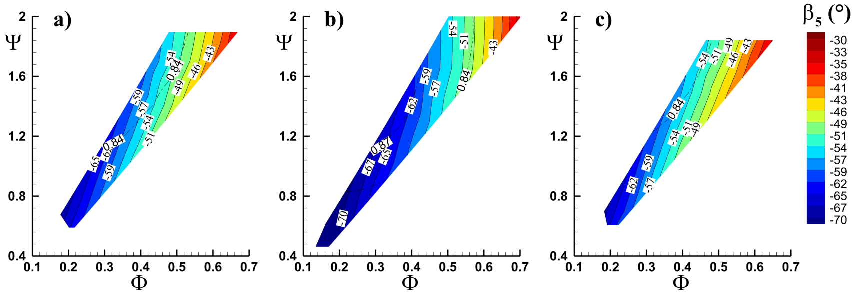

Figure 2.13: Contour of the rotor outlet flow angle in the relative frame of reference: (a) Test case 1; (b) Test Case 2; (c) Test Case 3. Locus of maximum total-to-static efficiency with dash-dotted line.

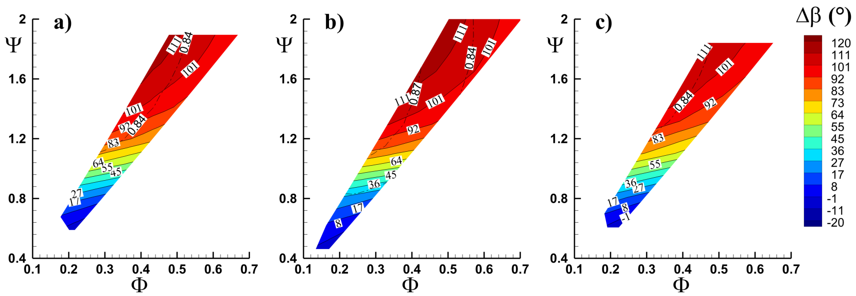

Figure 2.14: Contour of the flow turning (rotor inlet-rotor outlet): (a) Test case 1; (b) Test Case 2; (c) Test Case 3. Locus of maximum total-to-static efficiency with dash-dotted line.

These values, despite substantially lower than those found in other applications, e.g., turbocharging, are still relevant for some design candidates. Nevertheless, the practical feasibility of these designs is intrinsically connected to the rotor inlet radius, where the maximum blade peripheral speed occurs. The distribution of the rotor inlet radius, R_4, is shown in Fig. 2.16, together with the optimal efficiency curves. Rather similar values are observed for the first and third cases, while larger values occur in the second one. Furthermore, in the latter case the optimal efficiency curve is seen to span across non-monotone R_4 values.

The combination of the previous two quantities determines the blade peripheral speed, U_4, whose contour are presented in Fig. 2.17 together with the best efficiency line shown by dash-dotted line. As it can be noticed, the blade peripheral speed follows the same trends of the degree of reaction, Fig. 2.8, and the higher the degree of reaction, R^*, the higher the blade peripheral speed. However, rather safe values are detected, as in the most critical case the best efficiency line reaches 240 m/s.

Finally, the static enthalpy loss occurring in stator, vaneless interspace and rotor, Δh_N, Δh_{INT} and Δh_R, respectively, are presented in Figs. 2.18-2.20, and several conclusions can be drawn from their comparison.

First of all, a strong effect of the degree of reaction can be detected in the stator and rotor loss, Fig. 2.18 and 2.20. Moreover, the loss share between the two components is clearly driven by the distribution of the degree of reaction, Fig.2.8, with larger stator losses attaining to low degree of reaction, and the opposite scenario occurring at high degree of reaction. Particularly, when a low degree of reaction is selected, stator loss can be as high as the double of rotor loss. Furthermore, rotor loss variability in the design space is much larger than the stator loss. Concerning the losses occurring in the interspace gap, Fig. 2.19, despite one order of magnitude variability with the design space, they are always minor in comparison to those attaining to stator and rotor, being one or two order of magnitude smaller. Finally, if the lowest degree of reaction along the optimal η_{TS} curve is selected, stator losses account for about half –or even less– of the rotor losses, while the opposite condition is achieved at the high end of the best η_{TS} curve.

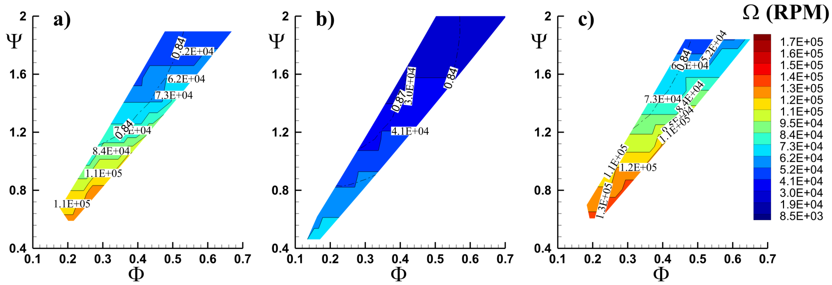

Figure 2.15: Contour of the turbine rotational speed: (a) Test case 1; (b) Test Case 2; (c) Test Case 3. Locus of maximum total-to-static efficiency with dash-dotted line.

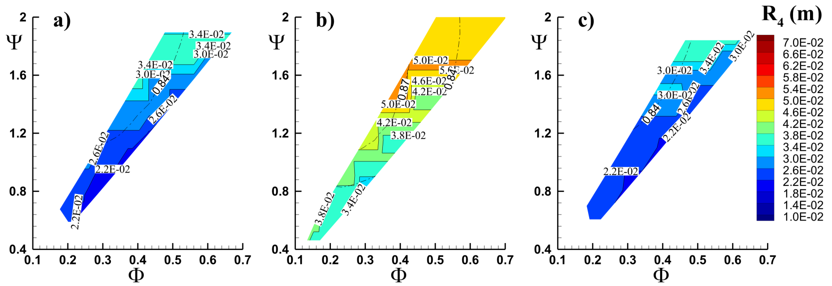

Figure 2.16: Contour of the rotor inlet radius: (a) Test case 1; (b) Test Case 2; (c) Test Case 3. Locus of maximum total-to-static efficiency with dash-dotted line.

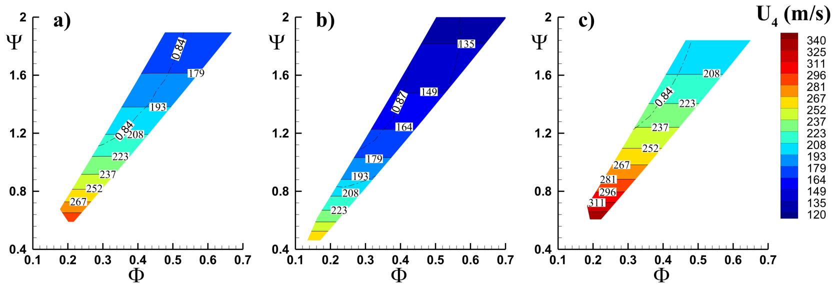

Figure 2.17: Contour of the blade peripheral velocity at rotor inlet: (a) Test case 1; (b) Test Case 2; (c) Test Case 3. Locus of maximum total-to-static efficiency with dash-dotted line.

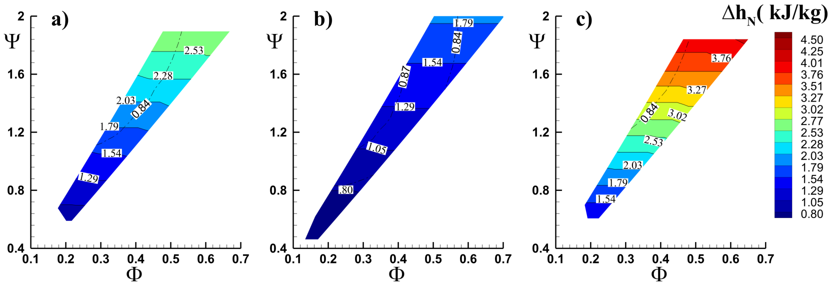

Figure 2.18: Contour of the stator static enthalpy loss: (a) Test case 1; (b) Test Case 2; (c) Test Case 3. Locus of maximum total-to-static efficiency with dash-dotted line.

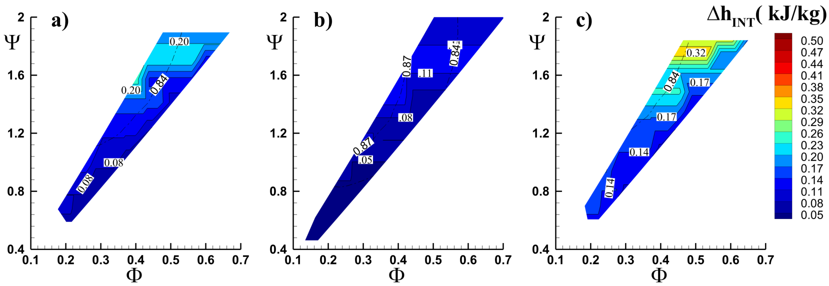

Figure 2.19: Contour of the vaneless interspace static enthalpy loss: (a) Test case 1; (b) Test Case 2; (c) Test Case 3. Locus of maximum total-to-static efficiency with dash-dotted line.

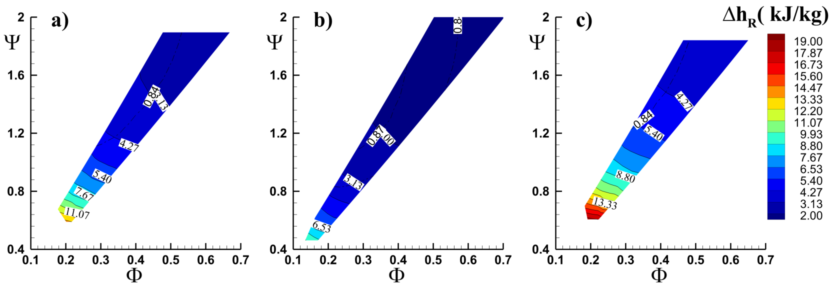

Figure 2.20: Contour of the rotor static enthalpy loss: (a) Test case 1; (b) Test Case 2; (c) Test Case 3. Locus of maximum total-to-static efficiency with dash-dotted line.

2.3.2 Validation and CFD Analysis

To assess the accuracy of the loss models and reliability of the meanline design code itself, a numerical validation of the meanline design results was performed by means of CFD calculations. However, the validation was restricted to the most promising candidates from turbine efficiency and feasibility points of view. For this purpose, one design candidate per test case was chosen selecting among the feasible designs, e.g., rotor inlet blade height larger than 2 mm, the optimal preliminary design from total-to-static efficiency point of view. Subsequently, first guess 3D stator geometries were built according to the method presented in Chapter 5, apart from the stator vanes of the second test case that, in view of the lower stator discharge Mach number, were shaped in ANSYS BladeGen directly so as to provide a purely converging channel. On the other hand, rotor first guess geometries were built by means of the Aungier's method (Aungier 2006d), as described in in Chapters 3.

The main features of each selected design candidate are presented in Tab. 2.3, whereas the corresponding velocity triangles (based on Mach number) are shown in Fig. 2.21. Finally, first guess 3D geometries built on these preliminary designs are shown in Fig. 2.22, in which the same scale is adopted for the three rotors.

3D steady-state RANS calculations were carried out in ANSYS CFX flow solver with fluid properties described by means Look-up Table (LuT) approach with table size 200x200. To reduce the computational cost, only one passage per row was simulated exploiting the geometrical periodicity via periodic boundary conditions. For turbulence closure k– ω SST turbulence model was used and Advection scheme was set to high resolution, whereas turbulence was set to first order.

TC	Φ	Ψ	R^*	Ma
R245fa – Test Case 1	0.31	1.2	0.41	1.67
R245fa – Test Case 2	0.26	0.91	0.54	1.17
MM	0.37	1.32	0.35	1.84

Table 2.3: Features of the selected turbine design candidates

$$r = h_{coarser}/h_{finer} \tag{2.49}$$

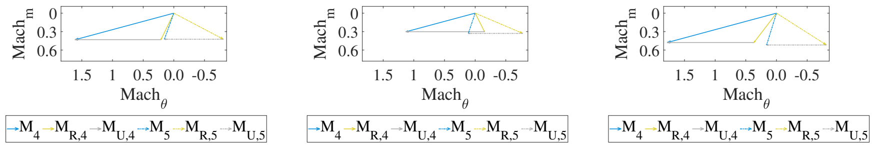

(a) R245fa – Test Case 1 (b) R245fa – Test Case 2 (c) MM

Figure 2.21: Mach-based velocity triangles of the selected turbine candidates

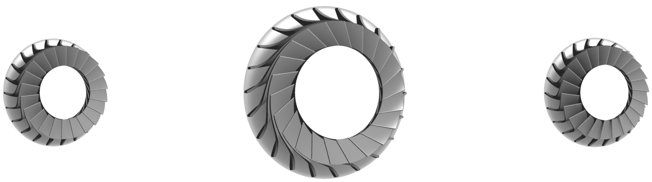

(a) Test Case 1: R245fa (b) Test Case 2: R245fa (c) Test Case 3: MM

Figure 2.22: First guess geometry for the selected turbine candidates

$$h = \sqrt[3]{\frac{Computational\ Domain\ Volume}{Cells\ Count}} \tag{2.50}$$

Also, to account for the different domain rotational speed between stator and rotor domains, a mixing-plane was implemented at their interface. All solid walls have been set to adiabatic with no-slip condition. Boundary conditions were provided in terms of inlet total pressure, $p_{0,In}$, and temperature, $T_{0,In}$, together with the inlet flow direction, whereas the downstream static pressure was set at the outlet boundary, p_{ous}, according to the values reported in Tab. 2.1. Finally, convergence was monitored by means of the RMS of the residuals together with several quantities at domains interfaces.

Firstly, a mesh sensitivity analysis was carried out for a geometry of the test case 1 (featuring intermediate characteristics with respect to the three design candidates investigated for the present validation) meshing the fluid domains by means of structured hexahedral meshes built in ANSYS TurboGrid. A first mesh, shown in Fig. 2.23a was built setting $y^+ = 1$ on vane and blade surfaces and $y^+ = 5$ at hub and shroud surfaces.

Subsequently, other two meshes, shown in Fig. 2.23b and 2.23c, have been built by progressively refining the mesh size so to ensure a refinement factor $r \geq 1.3$, Eqn. 2.49, as suggested by Roache (1997) and Roache, Ghia,

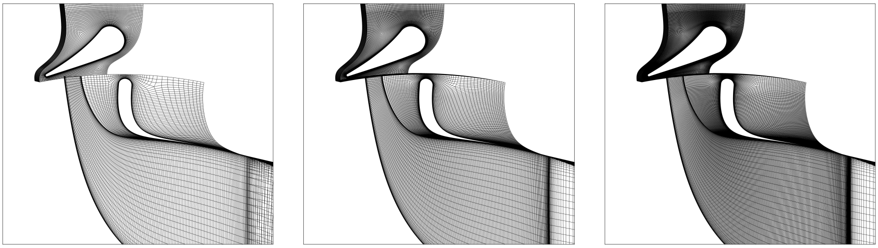

(a) Coarse Mesh (b) Medium Mesh (c) Fine Mesh

Figure 2.23: Meshes used for grid dependency analysis

and F. M. White (1986) –with h being the average mesh size defined as in Eqn. 2.50. This procedure resulted in the average mesh spacing and cell counts reported in Tab. 2.4. Finally, it is also worth mentioning that stator and rotor computational domains were enlarged upstream and downstream, respectively, so as to avoid forcing non-physical solution.

To perform the mesh dependency analysis of the results, the trends of several quantities, say total-to-static efficiency, stator discharge Mach number and rotor relative discharge Mach number, against the mesh size were monitored both as absolute values and percentage variation with respect to the results achieved on the finest mesh. Particularly, these trends are shown in Fig. 2.24 for the total-to-static efficiency, η_{TS}, and the stator discharge Mach number, Mach_3. As once can notice, quantities variation with mesh size is rather small, being within 3% for the coarse mesh, and within 1% for the medium mesh.

Concerning the rotor outlet relative Mach number, $\mathrm{Mach}_{5\,\mathrm{Rel}}$, despite not shown for brevity, extremely similar trends to Mach_3 were found, but at much smaller percentage differences always below 1%. Hence, in view of these results, the average mesh spacing corresponding to the medium mesh was deemed appropriate for the purpose of the meanline results validation and the computational mesh for the selected test cases, Tab. 2.3, whose 3D geometries are shown in Fig. 2.22, were built. However, considering the rather different sizes of the geometries, upon determining the required element count, the target average mesh spacing, h_{medium} Tab. 2.4, was correlated to the stator outlet and rotor inlet hydraulic diameters. Additionally, the tip gap region was included in the computational domain.

A comparison of the CFD results against the meanline results is provided in Tab. 2.5, in which one can notice that a generally good agreement is

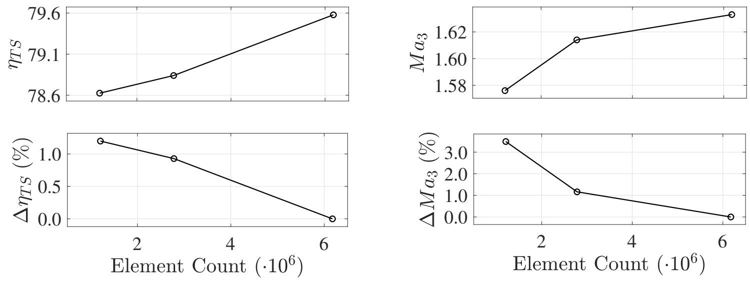

(a) η_{TS} (b) Mach_3

Figure 2.24: Results of the mesh sensitivity analysis

Mesh	y^+_{blade} (-)	y^+_{Endwall} (-)	Cells Count (-)	h 10^{-5} (m)	r Eqn. 2.49
Coarse	1	5	$1.21 \cdot 10^6$	9.32	-
Medium	1	5	$2.78 \cdot 10^6$	7.06	1.32
Fine	1	5	$6.18 \cdot 10^6$	5.41	1.30

Table 2.4: Mesh data used for grid sensitivity analysis

found concerning the total-to-total efficiency, η_{TT}, with a relative difference about 3% for the second and third test cases and within 5% for first test case. Conversely, larger discrepancies can be observed for the total-to-static efficiency, η_{TS}. This circumstance can arguably be ascribed to the effect of the tip leakage flow on the outlet flow angle, that is captured by the CFD calculations. In fact, the tip leakage vortex both affects the turbine efficiency and the outlet flow angle, although the blade span extent whose velocity triangles are affected by the tip leakage vortex is severely dependent on the blade height size and relative magnitude of the tip gap.

While the efficiency penalty ascribed to the tip leakage vortex is generally accounted for in all correlations used in meanline models, its effect on outlet velocity triangles is generally neglected, as in the correlation set adopted in the present meanline code. If a case with very small blade height, or a relatively large tip gap, is considered, the rotor outlet flow direction might be affected by the tip leakage vortex in a rather considerable portion of the blade span, although the meanline model cannot capture this effect. Therefore, a poor rotor outlet flow angle prediction by the meanline code

	η_{TT}		η_{TS}	
	1D	CFD	1D	CFD
R245fa – Test Case 1	88.05	83.82	84.46	76.40
R245fa – Test Case 2	88.29	87.69	85.14	80.01
MM	88.60	85.81	83.48	77.76

Table 2.5: Comparison of the CFD and meanline design results

may result.

This occurrence can be corroborated by looking at Fig. 2.25a in which a comparison between the rotor outlet velocity triangle from meanline and CFD results is provided. More specifically, CFD calculations have been carried out with and without tip gap and mass-weighted quantities at rotor outlet are presented for both cases. As one can notice, inaccuracy of the meanline prediction of the relative outlet velocity, w_5, becomes much smaller when compared to the no-tip gap CFD calculation. Conversely, when the tip leakage vortex is present, the w_5 vector is rotated clockwise, leading the absolute velocity component, c_5, to increase with respect to the no-tip gap calculation and the meanline prediction. Thus, the lack in the meanline model of any correction factor to account for the effect of the tip leakage vortex on the rotor relative outlet velocity leads the meanline code to underestimate the absolute outlet velocity and the leaving kinetic energy. In turn, this eventually affects the accuracy of the total-to-static efficiency prediction.

A further confirmation of the above-mentioned features can be found in Fig. 2.25b where the change of relative rotor outlet flow angle, β_5, over the blade span is presented, for both CFD calculations, with and without tip gap. As clearly visible, the rotor relative outlet flow angle is severely affected by the tip-leakage flow from about the 0.6 of the blade span up to the 1.

Finally, quantitative comparison of mass-weighted CFD results –with and without tip gap– against meanline prediction, Tab. 2.6, shows that the meanline prediction of the rotor relative outlet flow angle is substantially improved when the tip gap is not included in the computational domain, which confirms the above considerations.

Figure 2.26 presents the absolute Mach number contour at the mid-span surface for the three test cases investigated, and as it can be noticed, regular trends are achieved. However, in spite of a less critical expansion ratio and discharge Mach number, the second stator, whose distribution

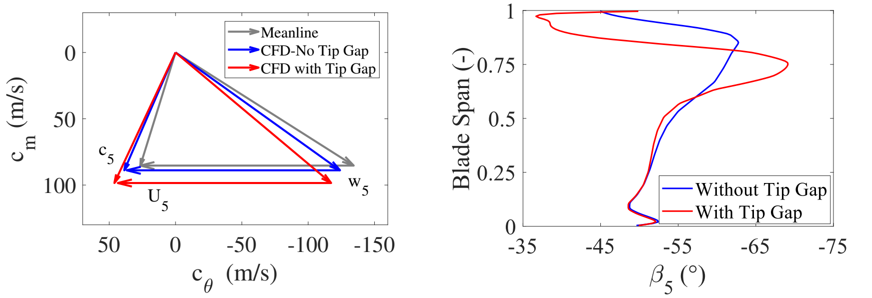

(a) Rotor outlet velocity triangles: meanline vs CFD with and without tip gap

(b) Rotor outlet relative flow angle change over the blade span with and without tip gap

Figure 2.25: Tip leakage flow effect on rotor outlet flow quantities

can be seen in the second case, Fig. 2.26b, exhibits less regular trends with an over-expansion in the front part of the suction side, followed by a re-compression, together with several waves in the rear suction side region, which can arguably be ascribed to an excessive curvature of suction side surface in the terminating region. Conversely, the two convergent-divergent stators, Fig. 2.26a and 2.26c, designed by means of the MoC, exhibit a rather regular flow field, both in the kernel and transition region. This occurrence can be verified in Fig. 2.27, which shows for both stators particularly smooth trends of the blade loading. The only exception is represented by the trace of a very small separation occurring at the terminating part of the suction side (above 0.9 streamwise coordinate), Fig. 2.27a, probably because of an impinging shock wave.

Figure 2.28 presents the blade loading for three blade span values, i.e.

	η_{TT}	η_{TS}	β_5	α_5	c_5	Mach_5
Meanline	88.60	83.48	-56.25	17.82	92.93	0.563
CFD - No Tip Gap	88.14	82.03	-54.70	23.60	100.50	0.608
CFD - Tip Gap	85.81	77.76	-51.00	24.57	113.30	0.6860

Table 2.6: Results comparison: Meanline code prediction vs mass-weighted CFD results with and without tip gap

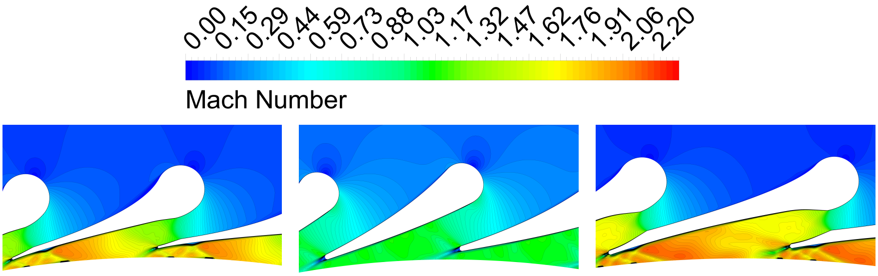

(a) Test Case 1: R245fa (b) Test Case 2: R245fa (c) Test Case 3: MM

Figure 2.26: Stator Mach number distributions at mid-span

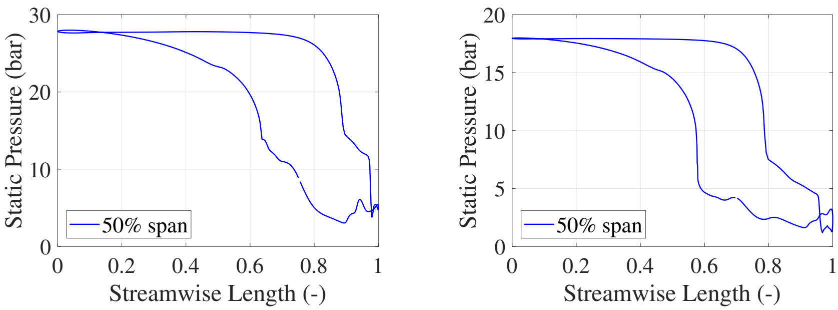

(a) Test Case 1: R245fa (b) Test Case 3: MM

Figure 2.27: Stator mid-span blade loading

20%, 50% and 70%, for the three test cases investigated. First and third cases, Fig. 2.28a and 2.28c, exhibit a larger blade loading within the first 40 % of the streamwise coordinate as a result of the large curvature and flow turning imposed by the highly cambered rotor profile of these two rotors. This eventually leads to a rather large flow separation, whose trace is clearly visible in the second half of the streamwise coordinate as a downward convexity in the suction side distribution. Conversely, rather regular and lighter loading is detected in the second case, Fig. 2.28b, as a consequence of the low blade curvature featured by this geometry. Interestingly, all the three test cases are characterized by a final pressure ripple in the blade loading

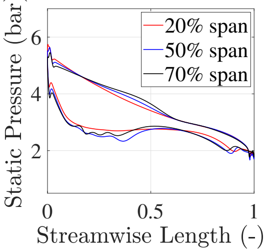

(a) Test Case 1: R245fa

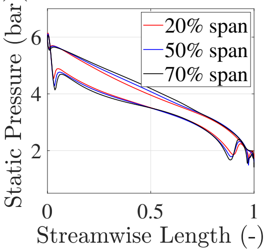

(b) Test Case 2: R245fa

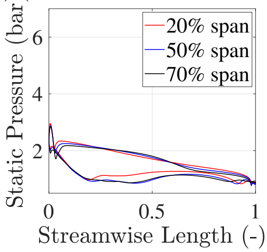

(c) Test Case 3: MM

Figure 2.28: Rotor blade loading at three blade span values: 20%, 50% and 70%

at the terminating part of the suction side. This feature can be ascribed to the adopted first guess thickness distribution (Aungier 2006d), which in fact leads to a sudden area ratio increase toward the end of the rotor channel. The latter leads to an undesired flow acceleration, strengthening the shock waves arising at the rotor TE.

As a final analysis the sensitivity of the rotor design to the rotational speed and to rotor blade count was assessed. To do so, additional CFD calculations were carried out to investigate these aspects. Particularly, the effect of a rotational speed change was assessed for the first test case by considering other two rotational speeds, 10 and 15 % larger than the design one and the effect on the rotor blade loading is shown in Fig. 2.29. As it can be noticed, at both blade spans smoother blade loading are obtained as the rotational speed is increased. In turn this also improves the total-to-total efficiency, as reported in Tab. 2.7.

To assess the effect of the blade count and to test the reliability of the correlation used to determine it, the rotor blade count of the second test case

	$1.00 \cdot \Omega_{Des}$	$1.10 \cdot \Omega_{Des}$	$1.15 \cdot \Omega_{Des}$
η_{TT}	83.82	86.55	86.73
η_{TS}	76.40	77.49	77.0

Table 2.7: Effect of rotational speed change over total-to-total and total-to-static efficiency

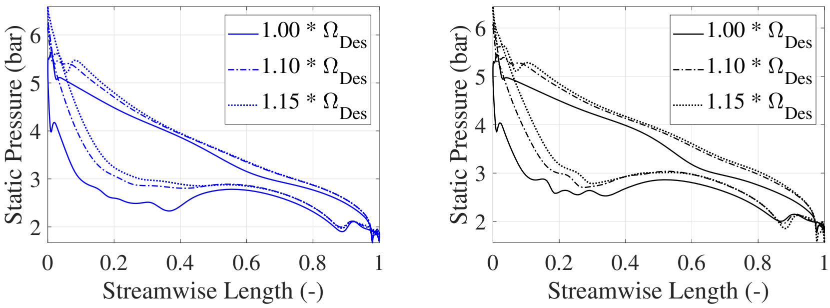

(a) 50% blade span

(b) 70 % blade span

Figure 2.29: Effect of the rotational speed on the rotor blade loading: test case 1

was a lowered from 22 to 17 blades and the effect was assessed by means of a CFD calculations. As one can notice from Fig. 2.30, that shows the rotor blade loading comparison at 50 and 70% of the blade span, the reduction of the blade count led to an increase of the blade loading and, interestingly, the total-to-total and total-to-static efficiencies increased as well, changing from 80.01 to 81.54 and from 87.64 to 88.59, respectively. The latter occurrence, in fact, suggests that the optimal blade count provided by the correlation, might be slightly overestimated.

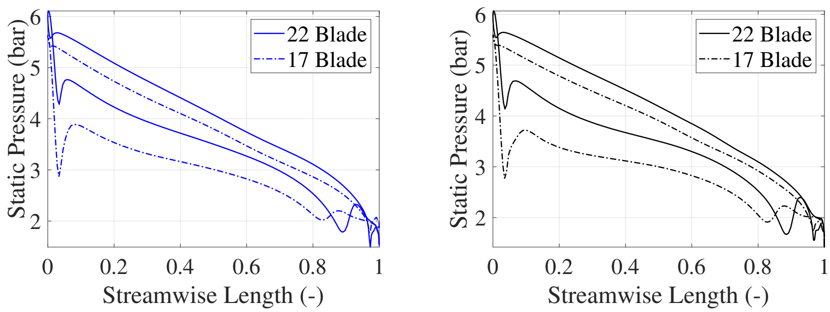

(a) 50% blade span

(b) 70 % blade span

Figure 2.30: Effect of the rotor blade count on the rotor blade loading: test case 2

2.4 Concluding Remarks

In the present chapter an overview on the meanline design, its purpose and integration into the turbine design workflow was provided. Subsequently, a meanline design code suited for ORC radial-inflow turbine design, which was developed by the author of the present thesis, was presented. The code was exploited to investigate the design space and the optimal design requirements of a RIT for tens of kW scale ORC power plant. To do so, a parametric analysis was carried out for several test cases, which differed by several parameters, such as working fluid, design mass flow rate and expansion ratio. The results of the test cases proved the sensitivity of the code to the operating conditions, highlighting different sizes of the optimal efficiency region and maximum achievable efficiency depending on the boundary conditions.

Furthermore, the results of validation – carried out against 3D CFD calculations– that was accomplished for selected turbine design candidates showed that the code provides a satisfactory accuracy for the total-to-total efficiency prediction, which is always within 3-5% difference with respect to the CFD results, even for the highest expansion ratio cases. Conversely, the lack of any rotor outlet velocity correction term to account for the effect of the tip leakage vortex led to an underestimation of the rotor leaving kinetic energy and, therefore, to a less accurate total-to-static efficiency prediction. In this regard, the introduction in the meanline code of corrective terms to account for the effects of tip leakage flow on rotor outlet flow angle is recommended as a future development.

The results of the unconstrained rotational speed test case highlighted that for the low expansion ratio test case weakly supersonic stator discharge conditions cannot be avoided if the optimal turbine efficiency region is targeted. Conversely, when higher expansion ratio cases are considered, highly supersonic stator discharge conditions are unavoidable if a single stage machine is sought. Also, the results showed that, despite a rather challenging design and rather large expansion ratio, the optimal efficiency requirement did not entail supersonic flows at rotor inlet in the relative frame of reference, as well as at rotor outlet. Furthermore, results showed that the total loss share between each row highly depends on the degree of reaction that is selected, eventually leading stator losses to account for more than the double of rotor losses for low degree of reaction values, as well as that stator-rotor interspace loss are generally minor compared to the other loss components.

Concerning the low expansion ratio case it is worth pointing out that, despite its higher efficiency and less challenging design might appear appealing, such a design would entail several drawbacks, such as higher fluid price as a consequence of larger mass flow rate, larger clutter, weight and pump consumption, which is generally not negligible in ORC power plant.

Finally, a possible future development consists in the coupling of the turbine meanline design code presented in this chapter to a thermodynamic cycle design code, to perform a simultaneous design. However, in view of the substantial complexity and number of design variables increase, the adoption of optimization algorithm would probably necessary.

CHAPTER 3

Rotor First Guess Geometry Methods

3.1 Introduction

Once the preliminary design is concluded and a successful turbine design candidate is found, the designer is asked to start the turbine aerodynamic design, thus, building a 3D geometry based on the design specifications coming from the preliminary design. This geometry could be either analyzed by means of 3D calculations, or by means of less sophisticated methods, such as two-dimensional models, e.g., throughflow and quasi-three-dimensional models. Subsequently, the geometry could either be improved by manual design iterations or by means of shape optimizations techniques.

Typically, in the preliminary design only inlet and outlet vane and blade angles are found, while the entire shape and blade angles laying between inlet and outlet stations should be determined to build a 3D blade shape. Therefore, building a first guess geometry on the design specifications retrieved in the preliminary design may pose a non-trivial challenge.

To overcome this issue, several methods have been developed over the years. Earlier in the past, when computational resources were very limited, the so-called *inverse methods*, were particularly popular. These, in fact, allowed the designer to determine a blade surface needed to provide a specified velocity distribution (Goldstein and Jerison 1947). However, these methods intrinsically rely on the experience of the designer and, when such a tool is used, the existence of a solution for the user-specified distribution is not guaranteed.

Nowadays, computational resources are more abundant, thus, design chains have moved towards more automated design approaches, at the price of larger number of 'function evaluations' required, say 3D CFD calculations.

However, regardless of the approach used to improve the design, namely manual iterations or optimizations algorithms, the quality of the first guess geometry is of paramount importance to the final solution and to the number of design iterations required.

Other methodologies to build a first guess geometry of RIT rotors, which rely on *direct methods*, rather than inverse ones, are available in published literature (Aungier 2006d; Glassman 1976). Nevertheless, these methodologies have been developed for ideal gases expanding through modest expansion ratios. Hence their applicability to ORC turbines is not straightforward.

For this reason, the present chapter provides an assessment of the performance of Aungier's and Glassman's methods when employed for the design of the first guess geometry of a RIT rotor for ORC plants. Actually, two different approaches to build a first guess geometry rotor are provided by the Aungier's method. The first one suited to alleviate mechanical stresses in the blade, i.e., the so-called radial-element blade method, and a second one, which instead gives priority to the aerodynamic performance, allowing to determine blade camberline angles at hub and shroud independently. Given the relatively low load of the present application, the latter approach was preferred to the former. Thus, it is the only one considered in the present work and it will be referred to as Aungier's method.

Aungier's and Glassman's methods were implemented in a simple program in MATLAB environment, which picks up a specific preliminary design candidate selected by the user and, according to the chosen method, computes hub and shroud meridional contours, as well as the camber lines, providing an input file to ANSYS BladeGen as output.

The two methods are presented in Sections 3.2 and 3.3, respectively, whereas their comparison is provided in Section 3.4. Finally, conclusions are drawn in Section 3.5.

The work shown in this chapter resulted in a poster that was presented at the ASME Turbo Expo 2020 (GT2020–16005) (Cappiello 2020).

3.2 Aungier's Method

Aungier's method (Aungier 2006d) provides guidelines to build the 3D geometry of the rotor at two spanwise stations, i.e., hub and shroud; and the contours of the meridional channel is built first. The hub contour is built connecting points P_{4h} and P_{5h}, Fig. 3.1, by means of a 90° circular arc whose radius of curvature is found as in Eqn. 3.1; in which the rotor axial length, L_x, is computed as in Eqn. 3.2, where R_{5h} and R_{5s} are the hub and shroud radii at rotor outlet station. The remaining part of the hub contour is made by a straight line placed either at the outlet, first case of Eqn. 3.1, or at the inlet, second case Eqn. 3.1.

$$R_C = \min \begin{cases} R_4 - R_{5h} \\ L_x \end{cases} \tag{3.1}$$

$$L_x = 1.5 \cdot (R_{5s} - R_{5h}) \tag{3.2}$$

The shroud contour is built connecting points P_{4s} and P_{5s} via a power law, Eqn. 3.3, of exponent n, where n is an integer value between 2 to 9, that should be chosen so at to provide the channel area at half of the meridional coordinate m, with m computed according to Eqn. 3.4, closer to the arithmetic average of rotor inlet and rotor outlet areas, A_4 and A_5, respectively.

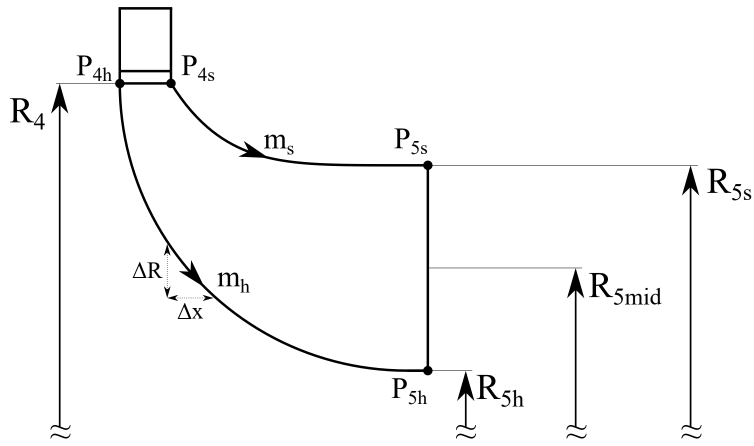

Figure 3.1: Meridional channel view schematic

$$R_{\mathrm{s}} = R_{5\mathrm{s}} + (R_4 - R_{5\mathrm{s}})\lambda^n \tag{3.3a}$$

$$\lambda = \frac{x - x_5}{L_x - b_4} \tag{3.3b}$$

$$\mathrm{d}m = \sqrt{\mathrm{d}R^2 + \mathrm{d}x^2} \tag{3.4a}$$

$$m = \int_{LE}^{TE} \mathrm{d}m \tag{3.4b}$$

The blade camber lines at hub and shroud are defined via a polynomial law expressing, the wrap angle θ as a function of the meridional coordinate m, Eqn. 3.4, computed for hub and shroud. The link between the meridional coordinate m and the wrap angle θ is expressed by Eqn. 3.5, in which the coefficients C_1, C_2, C_3, C_4, C_5 and C_6 are unknown. To close the system, the boundary conditions at LE and TE, together with the polynomial derivatives, can be used. To do so, the geometrical relation between the wrap angle θ and the blade metal angle β, Eqn. 3.6, can be exploited. This allows to match wrap angles equivalent to blade metal angles at hub and shroud LE and TE found in the preliminary design, as in Eqn. 3.7. In this regard it is worth mentioning that, while rotor metal angles at LE are constant throughout the blade span, their value at the TE hub and shroud will be determined as a consequence of the free-vortex distribution adopted in the preliminary design, Section 2.2.

Finally, the blade thickness distribution is found by assuming a constant value –equal to the leading edge thickness– from blade Leading Edge (LE) up to 90% of the meridional coordinate, m, whereas for the remaining 10% a linear distribution from leading edge thickness to Trailing Edge thickness is assumed. Both LE and TE thickness values have been determined by means of the Aungier's preliminary design method.

$$\theta_s(m) = \mathrm{C}_1 m_s + \mathrm{C}_2 m_s^3 + \mathrm{C}_3 m_s^4 \tag{3.5a}$$

$$\theta_h(m) = \mathrm{C}_4 m_h + \mathrm{C}_5 m_h^2 + \mathrm{C}_6 m_h^3 \tag{3.5b}$$

$$\theta = \int \frac{tan\beta}{R} \mathrm{d}m \tag{3.6}$$

$$\frac{\mathrm{d}\theta_{\mathrm{s}}}{\mathrm{d}m}(m_s = 0) = \frac{\tan\beta_{met,\mathrm{LE,s}}}{R_{\mathrm{LE,s}}} \tag{3.7a}$$

$$\frac{\mathrm{d}\theta_{\mathrm{h}}}{\mathrm{d}m}(m_h = 1) = \frac{\tan\beta_{met,\mathrm{TE,h}}}{R_{\mathrm{TE,h}}} \tag{3.7b}$$

$$\frac{\mathrm{d}\theta_{\mathrm{s}}}{\mathrm{d}m}(m_s = 1) = \frac{\tan\beta_{met,\mathrm{TE,s}}}{R_{\mathrm{TE,s}}} \tag{3.7c}$$

3.3 Glassman's Method

The first guess geometry guideline proposed by Glassman (1976) is actually simpler than the one presented in the Section 3.2 and does not provide guidelines concerning the blade angle and thickness distributions. For this reason it was complemented with reasonable assumptions that will be presented in the forthcoming.

Concerning the meridional channel shape, Glassman's method proposes to build the hub contour by means of a 90° elliptical arc, so as to connect the points P_{4h} and P_{5h}, Fig. 3.1. Conversely, the shroud contour is built by means of a 90° circular arc, whose radius is given by Eqn. 3.8, connecting P_{4s} and P_{5s}. As a results, the Glassman's method leads the rotor axial length, L_x, to be defined as in Eqn. 3.9.

$$R_{C\mathrm{s}} = R_{4\mathrm{s}} - R_{5\mathrm{s}} \tag{3.8}$$

$$L_x = b_4 + (R_{4\mathrm{s}} - R_{5\mathrm{s}}) \tag{3.9}$$

Differently from the approach followed for Aungier's method, the blade shape was determined prescribing a blade angle distribution, β, directly, and subsequently retrieving the wrap angle θ needed to locate the points of the blade in the 3D space. Particularly, a linear distribution from $\beta_{met,\mathrm{LE}}$ to $\beta_{met,\mathrm{TE}}$ was prescribed. Likewise, the thickness distribution, necessary to pass from a zero-thickness blade, i.e. the blade camber surface obtained interpolating hub and shroud camber lines, to the real pressure and suction surfaces of the blade, was given as a linear distribution from LE to TE thickness values.

3.4 Comparison of Aungier and Glassman Methods

A preliminary design from the first test case presented in Section 2.3 was selected choosing a suitable compromise between turbine efficiency, stator outlet absolute Mach number, rotor inlet relative Mach number and rotor flow turning. Particularly, a low rotor flow turning design was chosen, so as to reduce the risk of flow separation at the rotor suction side, resulting in an almost radial blade angle at rotor inlet. The main features of the selected turbine design are presented in Tab. 3.1, together with the velocity triangles, computed in the meanline design, shown in Fig. 3.2. Two rotor geometries were generated based on the specifications from the same preliminary design, by means of Aungier's and Glassman's methods, obtaining the meridional channel shapes presented in Fig. 3.3a, which clearly led to two difference blade shapes shown in Fig. 3.3b and 3.3c.

As one can notice, rather different meridional channel shapes have been obtained with the two methods. Particularly, a much shorter channel is obtained by means of the Glassman's method, therefore leading to a much more rapid area change from inlet to outlet of the rotor.

To assess the effects of different channel and blade shape on the fluid dynamic performance of the turbine, CFD calculations were carried out on the two rotor that had been matched to the same stator –designed in Ansys BladeGen. Computational meshes were built in Ansys TurboGrid, according to the results of the mesh sensitivity analysis presented in Section 2.3.2. Furthermore, CFD calculations have been carried out with the numerical setup described in the same Section.

Figure 3.4 presents the mid-span relative Mach number distributions for the two rotors obtained from the CFD calculations. As one can notice, the marked differences between the two rotors result in substantially different Mach number distributions. Particularly, more regular trends can be detected for the Aungier rotor, Fig. 3.4a, with small supersonic regions in proximity of the TE region. Conversely, the Glassman rotor exhibits much more irregular distribution with considerably higher Mach numbers in the front part of the suction side. These notable differences are also reflected in the rotor blade loading which are shown for the mid-span section in Fig. 3.5.

As a matter of fact, the pressure side distributions of the two configurations are rather comparable, whereas the suction side pressure distributions differ substantially, leading to a much larger loading of the Glassman rotor blade, consistently with the much large Mach number that can be seen in

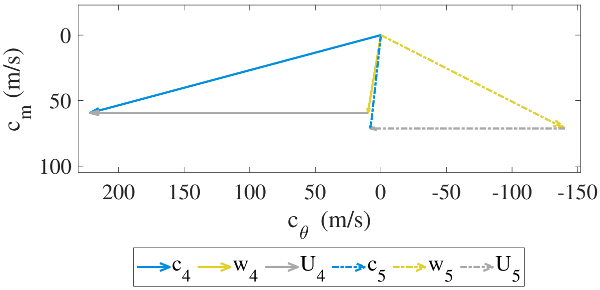

Figure 3.2: Velocity triangles of the selected turbine

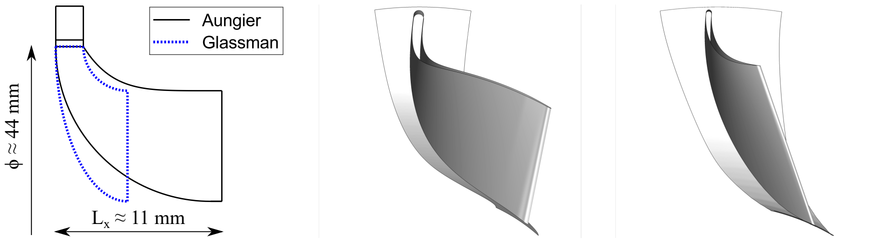

(a) Meridional channels (b) Aungier blade (c) Glassman blade

Figure 3.3: Comparison of Aungier's and Glassman's methods

the mid-span contour of Fig. 3.4b.

The area enclosed by the pressure distributions in Fig. 3.5 and, therefore, the force acting on the blade, appear much larger for the Glassman blade. However, this occurrence is not to be ascribed only to the different pressure distributions, but also to the fact that the distributions are shown as a function of the non-dimensional streamwise length. The dimensional streamwise length is indeed much shorter for the Glassman blade, as result of the shorter axial length featured by this configuration, Fig. 3.3a. Nonetheless, the much

Fluid	R^*	N_s	D_s	Φ	Ψ	η_{TS}	η_{TT}
R245fa	0.48	0.6	3.12	0.34	1.14	82.9	87.6

Table 3.1: Turbine characteristics

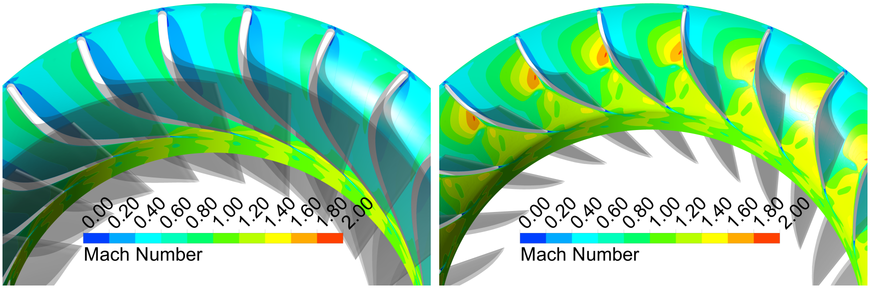

(a) Aungier rotor (b) Glassman rotor

Figure 3.4: Mid-span relative Mach number distributions

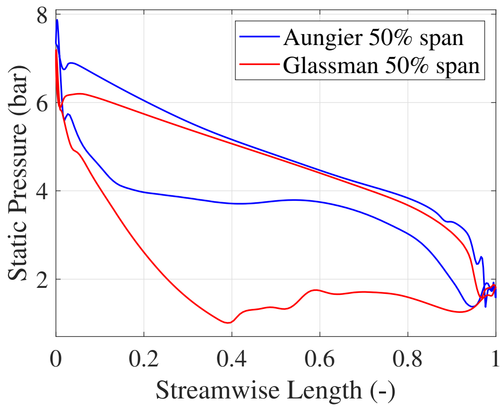

Figure 3.5: Comparison of mid-span blade loading for Aungier and Glassman rotors

higher Mach number achieved by the Glassman rotor together with a more rapid area change leads this configuration to feature lower total-to-total and total-to-static efficiency than the Aungier one, as reported in Tab. 3.2.

	η_{TT}	η_{TS}
Aungier	84,6	78,6
Glassman	81,0	72,4

Table 3.2: Comparison of the efficiency values achieved by the two turbines obtained with Aungier's and Glassman's methods

3.5 Concluding Remarks

In this chapter two 3D rotor blade geometries have been designed based on the same preliminary design by means of two different RIT rotor first guess geometry methods, i.e., the one by Aungier and the one by Glassman.

The comparison of the two methods highlighted that the Glassman one produces a much shorter rotor, featuring a more rapid area change, which in turn leads to a completely different Mach number distribution with respect to the Aungier's method. Conversely, the rotor design obtained by the Aungier's method provides more regular trends with considerably smaller maximum Mach number, leading to a smaller blade loading. As a result, the turbine equipped by the rotor designed by means of the Aungier's method exhibits larger total-to-total and total-to-static efficiency values.

In view of the above-mentioned considerations, the Aungier's method is the one that will be used to design the rotor blade geometries presented in the present thesis.

CHAPTER 4

Supersonic Nozzle Design by Means of Method of Characteristics

4.1 Introduction

Upon designing converging-diverging nozzles, the assumption of a sonic line shape allows the sizing of the divergent nozzle section independently of the converging one (Argrow and Emanuel 1988). The subsonic part of the nozzle, i.e., the converging one, can then be designed accordingly, so as to provide the assumed sonic line shape (Argrow and Emanuel 1991). Alternatively, the definition of suitable boundary conditions for the sizing of the divergent nozzle portion can be achieved by means of approximate methods, such as the one by Sauer (1947).

A well-established design practice consists in shaping the divergent section of the nozzle by means of the well-known Method of Characteristics (MoC) (Shapiro and Edelman 1947a; Shapiro and Edelman 1947b), that is a *marching-type* mathematical method, suitable for solving problems whose governing equations are a set of quasi-linear (i.e., when the highest order derivative depends linearly on the unknown (Quarteroni 2009)) non-homogeneous *hyperbolic Partial Differential Equations* (PDEs). As such, the MoC can be applied to supersonic flows.

Following the derivation provided by Zucrow and Hoffman (1977a), under the assumption of *steady*, *irrotational* flow, one can see that the governing equations are hyperbolic when the flow is supersonic. Particularly, the continuity equation can be written as in Eqn. 4.1, while the scalar product of $\mathbf{V}$ and the Euler's moment equation yields the Eqn. 4.2

$$(\mathbf{V} \cdot \nabla)\, p + \rho a^2 \nabla \cdot \mathbf{V} = 0 \tag{4.1}$$

$$(\mathbf{V} \cdot \nabla)\, p + \rho\, (\mathbf{V} \cdot \nabla) \left(\frac{V^2}{2} \right) \tag{4.2}$$

The combination of Eqns. 4.1 and 4.2, expressed in Cartesian coordinates gives Eqn. 4.3, where u, v and w are the x, y and z velocity components, and a is the speed of sound, while the subscripts $_x$, $_y$ and $_z$ stand for the partial derivative with respect to the subscript.

$$\begin{aligned}(u^2 - a^2)u_x + (v^2 - a^2)v_y + (w^2 - a^2)w_z + uv(u_y + v_x) + \\ uw(w_x + u_z) + vw(w_y + v_z) = 0\end{aligned} \tag{4.3}$$

If a *planar* flow is considered, Eqn. 4.3 reduces to Eqn. 4.4

$$(u^2 - a^2)u_x + (v^2 - a^2)v_y + 2uvu_y = 0 \tag{4.4}$$

Being the flow irrotational ($u_y - v_x = 0$), a velocity potential, ϕ, such that $u = \phi_x$ and $v = \phi_y$, exists. Therefore, Eqn. 4.4 can be expressed in terms of a velocity potential ϕ, yielding Eqn. 4.5

$$({\phi_x}^2 - a^2)\phi_{xx} + ({\phi_y}^2 - a^2)\phi_{yy} + 2\phi_x\phi_y\phi_{xy} = 0 \tag{4.5}$$

Equation 4.5 is a second order quasi-linear PDE, that belongs to the general equation type presented in Eqn. 4.6 and can be classified according to the sign of the quantity ($B^2 - 4AC$), similarly to quadratic algebraic equations, in *elliptic*, *parabolic* and *hyperbolic* equations.

$$Au_{xx} + Bu_{xy} + Cu_{yy} + Du_x + Eu_y + Fu = 0 \tag{4.6}$$

Dividing by $-a^2$ and rearranging Eqn. 4.5 yields Eqn. 4.7

$$\left(1 - \frac{u^2}{a^2}\right)\phi_{xx} - \frac{2uv}{a^2}\phi_x\phi_y + \left(1 - \frac{v^2}{a^2}\right)\phi_{yy} = 0 \tag{4.7}$$

It is easy to show that for Eqn. 4.7 the quantity $(B^2 - 4AC)$ is equal to $(\mathrm{Ma}^2 - 1)$. Therefore, according to the value of the Mach number, three scenarios are possible:

- $\mathrm{Ma}^2 < 1$, the flow is subsonic and the quantity $(B^2 - 4AC)$ is < 0. Therefore, the equations are *elliptic*
- $\mathrm{Ma}^2 = 1$, the flow is sonic and the quantity $(B^2 - 4AC)$ is $= 0$. Therefore, the equations are *parabolic*
- $\mathrm{Ma}^2 > 1$, the flow is supersonic and the quantity $(B^2 - 4AC)$ is > 0. Therefore, the equations are *hyperbolic*

As mentioned earlier, the MoC is marching-type method, therefore, it is well suited to supersonic flows, for which a certain portion the flow field is not affected by the downstream one. This allows an initial condition to be propagated in space downstream.

The method relies on the concept of *characteristic curves*, that are suited to various interpretations (Zucrow and Hoffman 1977b). From a mathematical point view, these are curves along which the original PDEs can be manipulated to yield a *total differential equation*, called *compatibility equation*, that is valid *only* along the characteristic curve. Also, these are the curves along which the solution at a point is propagated in the downstream region of influence. It is also worth noting that, while the quantities remain continuous along the characteristics, their derivative can be discontinuous. From a physical point of view, the characteristics are curves on which the disturbances propagate and, as such, are the Mach lines, inclined with respect to the streamline of μ, Eqn. 4.8.

$$\mu = \arcsin\left(\frac{1}{\mathrm{Ma}}\right) \tag{4.8}$$

For a 2D steady supersonic irrotational flow, the slope of the characteristic lines $m_\pm$, can be computed as in Eqn. 4.9, where the $\pm$ sign refers to the two values of the square root. Thus, if the flow is subsonic, the characteristics are imaginary; if the flow is sonic, only one characteristic exists at a point; while, if the flow is supersonic, two real characteristics exist at a given point, corresponding to the two values of the square root and each of them belongs to one family of characteristics. Alternatively, the characteristics slopes can be computed as in Eqn. 4.10, in which φ is the streamline angle.

$$m_\pm = \left(\frac{\mathrm{d}y}{\mathrm{d}x}\right)_\pm = \frac{uv \pm a^2\sqrt{\mathrm{Ma}^2 - 1}}{u^2 - a^2} \tag{4.9}$$

$$m_{\pm} = \tan(\varphi \pm \mu) \tag{4.10}$$

A remarkable case is what is called a *simple wave flow*, of which the Prandtl-Meyer expansion fan is an example. In such a case, the characteristics, i.e., the Mach lines, of one of the two families become straight lines. Particularly, for a clockwise flow turning, the C_+ characteristics, namely, the *left-running* characteristics, are straight lines; conversely, for a counterclockwise rotation, *right-running*, or C_-, characteristics are straight lines.

If a 2D steady supersonic irrotational flow is concerned, the method of characteristics, therefore, allows to replace the original PDEs with a simpler total differential equation, valid only along the characteristic lines. The characteristic and total differential equations can then be solved together by means of finite difference methods in a simpler manner with respect to the original PDEs.

However, the original formulation of the MoC assumes the fluid to be a perfect gas, making it not suitable for dense vapor applications. A first adaptation to non-ideal gas was provided by Aldo and Argrow (1993); since then, several methods have been developed, e.g., the one by A. P. S. Wheeler and Ong (2013), under the assumption of polytropic transformation, as well as other methods using thermodynamic libraries (Anand, Vitale, et al. 2018).

The present chapter is concerned with types of nozzles that provide a uniform flow and exhibit a minimum inner throat-to-exit length ratio. As such, they are commonly referred to as *Minimum Length Nozzles* (MLNs). While both *sharp-edged throat* and *smoothly contoured* nozzles exist, Fig. 4.1a and 4.1b, respectively, only the first kind is considered in this chapter.

In the forthcoming, an existing algorithm for the design of a planar (hence 2D) sharp-edged throat minimum length nozzle based on the Method of Characteristics is reviewed and its extension to dense gases is provided.

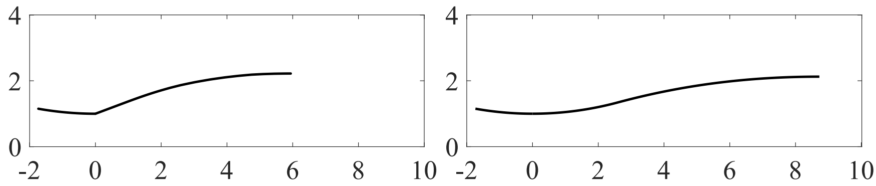

(a) 2D half sharp-edged nozzle (b) 2D half smoothly contoured nozzle

Figure 4.1: Examples of nozzle shapes. Throat location at $x = 0$

Subsequently, the code is applied to some illustrative test cases and the effect of fluid properties is assessed.

4.2 Algorithm implementation

In the present work the extension to dense vapors of an existing Method of Characteristics (MoC) algorithm developed for perfect gases, i.e., the one by Vanco and Goldman (1968), is provided. More specifically, the selected algorithm allows to perform the sizing of a *sharp-edged* Minimum Length Nozzle (MLN) with straight sonic line, under the assumption of steady, inviscid, isentropic 2D flow. The resulting geometry delivers at its outlet section a uniform flow, parallel to the nozzle axis, at a desired target Mach number, $\mathrm{Ma}_{\mathrm{tg}}$. Furthermore, the present algorithm is implemented in MATLAB and uses CoolProp thermodynamic library (I. H. Bell et al. 2014) for the computation of dense vapor properties. Furthermore, it is worth mentioning that the original algorithm, differently from other reported in published literature, say Goldman and Vanco (1971), no correction is applied to the computed shape to account for the flow blockage introduced by the boundary layer thickness.

In the forthcoming the algorithm implementation will be presented, also pointing out the modifications adopted in the present work in order to allow the extension to fluid flows not obeying to the perfect gas model.

The MoC algorithm developed in the present work, of which a schematic representation is provided in Fig. 4.2, requires the definition of some input data, that are the *working fluid*, target Mach number to be reached at nozzle outlet, $\mathrm{Ma}_{\mathrm{tg}}$, total temperature and pressure in the throat, $T_{0,\mathrm{tg}}$ and $p_{0,\mathrm{tg}}$, and, finally, the Prandtl-Meyer step, $\Delta\nu$, which define the accuracy of the discretization. Subsequently, the static pressure at the throat and at discharge section must be computed, Fig. 4.2. The former represents the static pressure reached after an isentropic expansion from $p_{0,\mathrm{In}} = p_{0,\mathrm{tg}}$ to $\mathrm{Ma} = 1$, while the latter correspond to an isentropic expansion from the same total pressure $p_{0,\mathrm{tg}}$ to $\mathrm{Ma} = \mathrm{Ma}_{\mathrm{tg}}$. Additionally, in the present code, the two static pressures are computed via bracketing method, that is to say, for each of the two static pressure, the search interval is progressively halved, while, at each iteration, the error with respect to the target is computed at the two bounds of the interval via Eqns. 4.11, up to the error, Eqn. 4.11g, becomes smaller than a user specified threshold.

$$h_0 = EoS(T_0, p_0) \tag{4.11a}$$

$$s = s_0 = EoS(T_0, p_0) \tag{4.11b}$$

$$h_{guess} = EoS(p_{guess}, s_0) \tag{4.11c}$$
$$a_{guess} = EoS(p_{guess}, s_0) \tag{4.11d}$$

$$c_{guess} = \sqrt{2 \cdot (h_0 - h_{guess})} \tag{4.11e}$$
$$\mathrm{Ma}_{guess} = \frac{c_{guess}}{a_{guess}} \tag{4.11f}$$

$$\mathrm{Error} = \mathrm{Ma} - \mathrm{Ma}_{guess} \tag{4.11g}$$

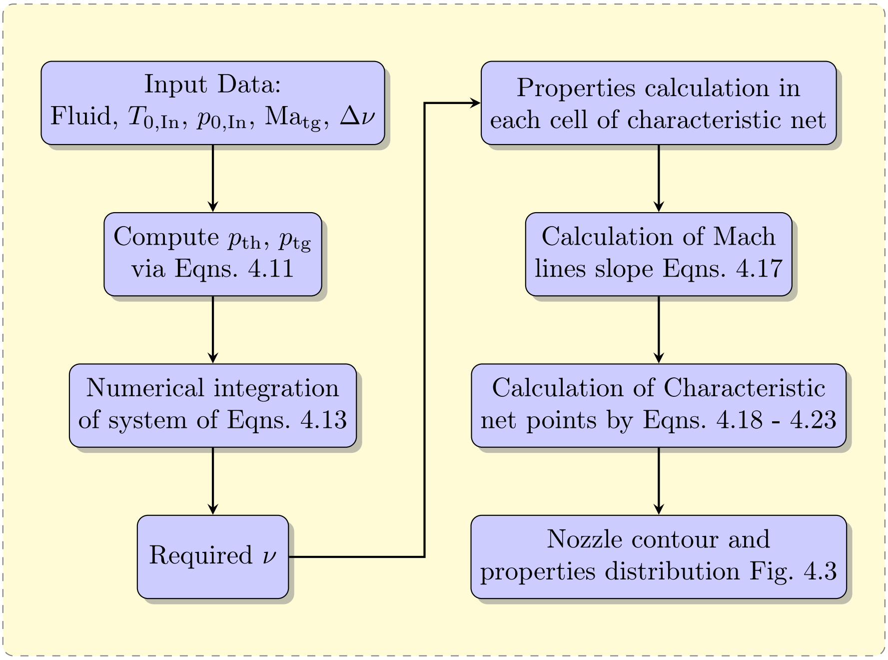

Figure 4.2: Schematic representation of the Method of Characteristic algorithm

The second step of the algorithm, Fig. 4.2, consists in the computation of the Prandtl-Meyer function, ν. The latter is required for the solution on the characteristics net and represents the angle through which the flow must be turned so as to bring it from Ma = 1 to a $\mathrm{Ma_{tg}}$. For a perfect gas the Prandtl-Meyer function can be computed as in Eqn. 4.12 as a function of the specific heat ratio, γ, and the target Mach number, $\mathrm{Ma_{tg}}$.

$$\nu = \sqrt{\frac{\gamma+1}{\gamma-1}} \arctan \sqrt{\left(\frac{\gamma-1}{\gamma+1}\right)\left(\mathrm{Ma}_{\mathrm{tg}}^2 - 1\right)} - \arctan \sqrt{\mathrm{Ma}_{\mathrm{tg}}^2 - 1} \qquad (4.12)$$

However, this expression is not applicable to dense vapor flows and is therefore replaced in the present algorithm implementation by the system of differential equations, Eqns. 4.13, adapted from M. Cramer and Crickenberger (1992). The latter system of differential equations is integrated numerically taking as initial flow properties those evaluated at the throat.

$$\frac{\mathrm{d}\nu}{\mathrm{d}V} = \frac{\left(\mathrm{Ma}^2 - 1\right)^{1/2}}{V\mathrm{Ma}^2} \qquad (4.13a)$$

$$\frac{\mathrm{dMa}}{\mathrm{d}V} = -\frac{\mathrm{Ma}}{V}J \qquad (4.13b)$$

$$J = 1 - \Gamma - \mathrm{Ma}^{-2} \qquad (4.13c)$$

$$\Gamma = 1 + \frac{\rho}{a}\left(\frac{\partial a}{\partial \rho}\right)_s = EoS(V, s_{\mathrm{th}}) \qquad (4.13d)$$

Once the overall flow turning required to bring the flow to the $\mathrm{Ma_{tg}}$ is known, that is the Prandtl-Meyer function ν, it is possible to proceed to the subsequent algorithm step, Fig. 4.2.

The *Right-Running* (RR) characteristics in which the expansion fan centred at the nozzle sharp edge is discretized, blue lines in Fig. 4.3, meet the nozzle centreline and are reflected as *Left-Running* (LR) characteristics, red lines in Fig. 4.3. The latter then meet the nozzle contour, that must be shape so as to cancel them. The intersection of the RR and LR characteristics forms the characteristic net, subdividing the nozzle flow into small cells in which the flow properties are assumed to be constant.

Being dependent on the overall Prandtl-Meyer function ν and user specified Prandtl-Meyer step used for discretization, $\Delta\nu$, the number of RR and LR characteristics is known, and therefore so is the number of cells of the characteristics net. Although their size, position and properties value are still unknown.

In order to build the nozzle contour, one should solve for the streamline angle, φ, Mach angle, μ, and properties values in each cell. φ, ν and μ value in each cell can still be computed as for a perfect gas flow, Eqn. 4.14; in which k and n are the indexes for the RR and LR characteristics, respectively. However, the computation of the Mach angle requires the knowledge of the local Mach number in the cell of the characteristic net, Eqn. 4.14c. For a perfect gas the latter can be computed via Eqn. 4.15, $\mathrm{Ma}^*_{k,n}$ being the ratio of the local flow velocity to the sonic velocity in the throat, which can be computed iteratively from Eqn. 4.16. Unfortunately, Eqns. 4.15 and 4.16 are not suitable for a dense vapors. Thus, in the present algorithm implementation they are replaced by the link between ν and Ma provided by the system of Eqns. 4.13, which is instead of general validity.

$$\varphi = (k-1)\cdot\Delta\nu \tag{4.14a}$$

$$\nu = 2\Delta\nu\cdot(n-1)+(k-1)\cdot\Delta\nu \tag{4.14b}$$

$$\mu = \arcsin\left(\frac{1}{\mathrm{Ma}_{k,n}}\right) \tag{4.14c}$$

$$\mathrm{Ma}_{k,n} = \sqrt{\frac{\left(\frac{2}{\gamma+1}\right)\cdot {\mathrm{Ma}^*}^2_{k,n}}{1-\left(\frac{\gamma-1}{\gamma+1}\right)\cdot {\mathrm{Ma}^*}^2_{k,n}}} \tag{4.15}$$

$$\nu_{k,n} = \frac{\pi}{4}\cdot\left(\sqrt{\frac{\gamma+1}{\gamma-1}}-1\right)+$$
$$\frac{1}{2}\left\{\sqrt{\frac{\gamma+1}{\gamma-1}}\arcsin[(\gamma-1)\cdot {\mathrm{Ma}^*}^2_{k,n}-\gamma]+\arcsin\left(\frac{\gamma+1}{{\mathrm{Ma}^*}^2_{k,n}}-\gamma\right)\right\} \tag{4.16}$$

The following step of the algorithm Fig. 4.2 consists in the computation of the characteristic lines slope, m, Eqn. 4.17, for which average values of adjacent cells are used as in the original algorithm.

$$m_{\mathrm{LR}} = \tan\left(\frac{\mu_{k,n}+\mu_{k-1,n+1}}{2}+\frac{\varphi_k+\varphi_{k-1}}{2}\right) \tag{4.17a}$$

$$m_{\mathrm{RR}} = -\tan\left(\frac{\mu_{k,n}+\mu_{k+1,n}}{2}-\frac{\varphi_k+\varphi_{k+1}}{2}\right) \tag{4.17b}$$

The knowledge of the characteristic lines slope allows to move to the subsequent step of the algorithm, Fig. 4.2, computing x and y coordinates of nozzle centreline points, nozzle contour points and characteristic lines intersection points, each of them requiring specific equations.

- For *interior points*, $2 \leq k \leq k_{\max} - 1$, two cases can be encountered:
  - When $n = 1$, x and y coordinates are given by Eqn. 4.18
  - When $2 \leq n \leq n_{\max} - 1$, x and y coordinates are given by Eqn. 4.19
- For nozzle *centreline points*, $k = 1, m_{\mathrm{LR}} = 0$, two cases can be encountered:
  - When $n = 1$, x and y coordinates are given by Eqn. 4.20
  - When $2 \leq n \leq n_{\max} - 1$, x and y coordinates are given by Eqn. 4.21
- For nozzle *contour points*, $k = k_{\max}$, two cases can be encountered:
  - When $n = 1$, x and y coordinates are given by Eqn. 4.19, with Eqn. 4.22 replaced in Eqn. 4.19a.
  - When $2 \leq n \leq n_{\max} - 1$, x and y coordinates are given by Eqn. 4.22 and Eqn. 4.18

Finally, the throat coordinates are given by Eqn. 4.23.

$$x_{k,n} = \frac{(y_{k+1,n-1} - m_{\mathrm{RR}} \cdot x_{k+1,n-1}) - (y_{k-1,n} - m_{\mathrm{LR}} \cdot x_{k-1,n})}{m_{\mathrm{LR}} - m_{\mathrm{RR}}} \tag{4.18a}$$

$$y_{k,n} = y_{k-1,n} + m_{\mathrm{LR}} \left(x_{k,n} - x_{k-1,n}\right) \tag{4.18b}$$

$$x_{k,1} = \frac{1 - (y_{k-1,1} - m_{\mathrm{LR}} \cdot x_{k-1,1})}{m_{\mathrm{LR}} - m_{\mathrm{RR}}} \tag{4.19a}$$

$$y_{k,1} = y_{k-1,1} + m_{\mathrm{LR}} \left(x_{k,1} - x_{k-1,1}\right) \tag{4.19b}$$

$$x_{1,1} = -\frac{1}{m_{\mathrm{RR}}} \tag{4.20a}$$

$$y_{1,1} = 0 \tag{4.20b}$$

$$x_{k,n} = -\frac{y_{k+1,n-1} - m_{\mathrm{RR}} \cdot x_{k+1,n-1}}{m_{\mathrm{RR}}} \tag{4.21a}$$

$$y_{k,n} = 0 \tag{4.21b}$$

$$m_{\mathrm{RR}} = \tan\left(\varphi_{k_{\max},n}\right) \tag{4.22}$$

$$x = 0 \tag{4.23a}$$

$$y = 1 \tag{4.23b}$$

4.3 Application

The procedure described in Section 4.2 allows building the characteristic net, as well as provides the properties distribution from a straight sonic line, $\mathrm{Ma} = 1$, up to a uniform $\mathrm{Ma}_{\mathrm{tg}}$ at nozzle discharge together with the nozzle contour made non-dimensional by half inlet width. Figure 4.3 shows the results of the Method of Characteristics algorithm implementation described in the present chapter, obtained for R245fa fluid, and the boundary conditions reported in Tab. 4.1. Particularly, Fig. 4.3a shows the characteristic net obtained as a result of the MoC algorithm –with blue and red lines being RR and LR waves, respectively– although, for legibility reasons the number of Mach lines plotted has been reduced with respect to those used for computation; Fig. 4.3b instead shows the distribution of the Mach number on the cells bounded by the characteristic net (shown in Fig. 4.3a), from the sonic line in the throat, where $\mathrm{Ma} = 1$, up to a uniform discharge Mach number.

To assess the effect of the working fluid on nozzle size and shape, the MoC algorithm was run for a series of working fluids, i.e., R245fa, Toluene, Pentane and Ethanol, for two target Mach number values, namely 1.6 and 2.0, at the same reduced total pressure, $p_{0,\mathrm{In,r}}$, and temperature, $T_{0,\mathrm{In,r}}$, of those considered in the previous test case, Tab. 4.1. The results are presented in Fig. 4.4, which shows the upper halves of the nozzle divergent sections, made non-dimensional by the inlet width.

First of all, the effect of the target Mach number on the nozzle shape is clearly visible. In fact, for a given working fluid and inlet thermodynamic state, the larger the target Mach number, the larger nozzle length and exit width, consistently with the increasing expansion ratios required

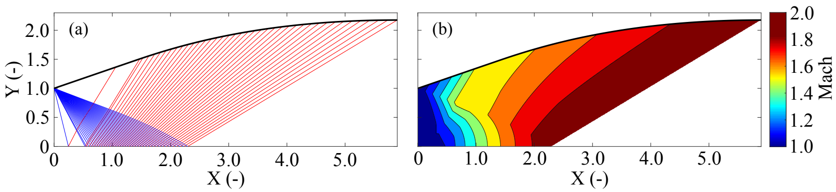

Figure 4.3: Result of Method of Characteristics algorithm: (a) Characteristic net (reduced number of waves plotted) –blue lines: Right-Running Waves, red lines: Left-Running Waves; (b) Mach number distribution on the divergent nozzle portion from the MoC algorithm

Working Fluid	$T_{0,\mathrm{In}}$ (K)	$T_{0,\mathrm{In,r}}$ (-)	$p_{0,\mathrm{In}}$ (bar)	$p_{0,\mathrm{In,r}}$ (-)	$\mathrm{Ma_{tg}}$
R245fa	439	1.028	28	0.767	1.89

Table 4.1: MoC boundary conditions used for the sample nozzle shown in Fig. 4.3.

as the target Mach number increases.

Secondly, a change in nozzle length and exit width arises as a result of a working fluid change. The latter can be even better visualized in the close-up view of the outlet section provided in Fig. 4.4a for the lower Mach target case. Interestingly, the change in nozzle dimensions that occurs when the design is accomplished for different fluids increases when the target Mach number increases, Fig. 4.4b, while the size ranking from fluid to fluid ranking remains unaltered as the target Mach number increases, Fig. 4.4.

The effect of the fluid change on nozzle size and length can be explained characterizing the expansion process of each fluid, under the assumption of *polytropic process*, Eqn. 4.24, by means of the average polytropic exponent k, which can be computed taking the linear regression of the quantities $\log(\rho/\rho_0)$ and $\log(p/p_0)$ along the expansion. Whilst this approach leads to larger inaccuracy as the critical point is approached, it provides an effective understanding of the working fluid effect of nozzle geometry.

$$\left(\frac{p_0}{p}\right) = \left(\frac{\rho_0}{\rho}\right)^k \tag{4.24}$$

For the present application the linear regressions of $\log(\rho/\rho_0)$ vs $\log(p/p_0)$

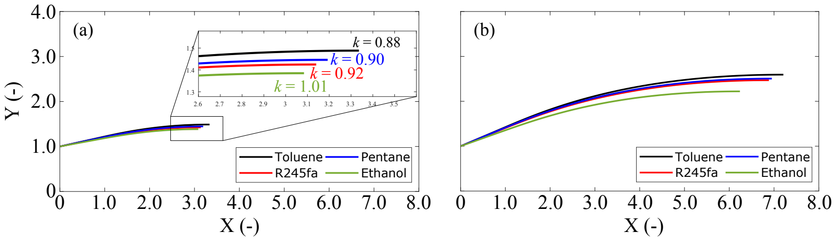

Figure 4.4: Effect of working fluid on the upper half contour of the nozzle divergent section from MoC at $p_{0,\mathrm{r}} = 0.767$ and $T_{0,\mathrm{r}} = 1.028$, for: $\mathrm{Ma_{tg}} = 1.6$ (a), $\mathrm{Ma_{tg}} = 2.0$ (b)

	Ethanol	R245fa	Pentane	Toluene
$\mathrm{Ma_{tg}} = 1.6$	1.01	0.92	0.90	0.88
$\mathrm{Ma_{tg}} = 2.0$	1.02	0.96	0.94	0.93

Table 4.2: Results of the linear regressions of $\log(\rho/\rho_0)$ vs $\log(p/p_0)$ along the eight expansions corresponding to the nozzle shown in Fig. 4.4

have been performed taking 1000 couples along each expansion line of all the eight expansions corresponding to the nozzles in Fig. 4.4. The results of the regressions are shown in Tab. 4.2, while the regression themselves are presented in Fig. 4.5 and 4.6, for $\mathrm{Ma_{tg}} = 1.6$ and 2.0, respectively.

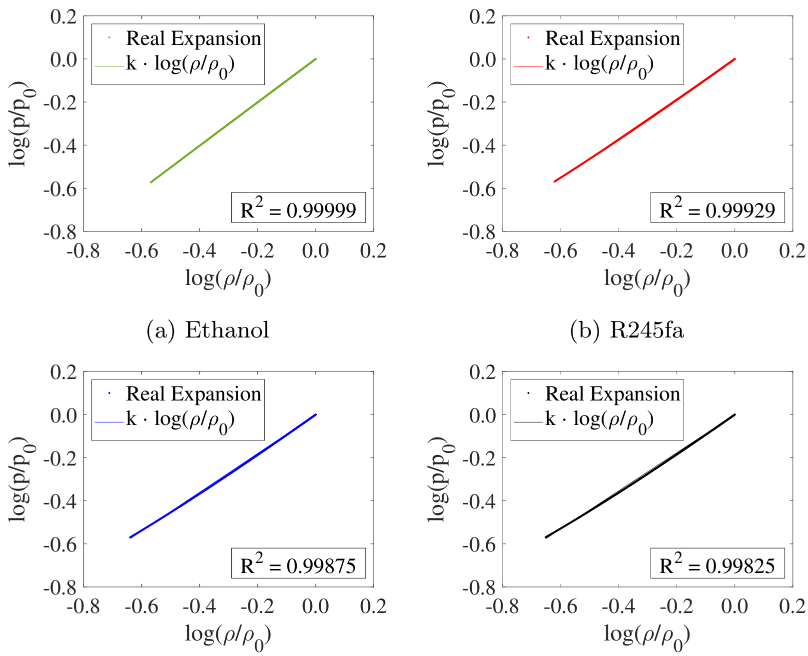

(a) Ethanol (b) R245fa

(c) Pentane (d) Toluene

Figure 4.5: Results of the linear regressions of $\log(\rho/\rho_0)$ vs $\log(p/p_0)$ along the expansions corresponding to the nozzle shown in Fig. 4.4a corresponding to $\mathrm{Ma_{tg}} = 1.6$

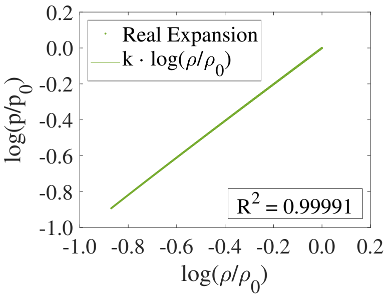

(a) Ethanol

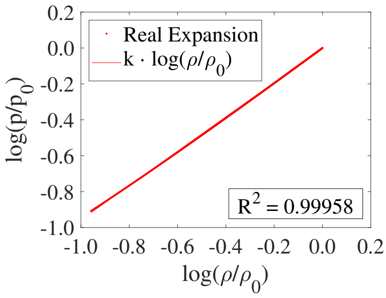

(b) R245fa

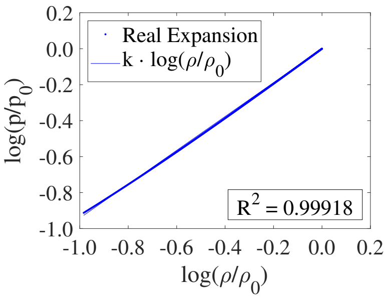

(c) Pentane

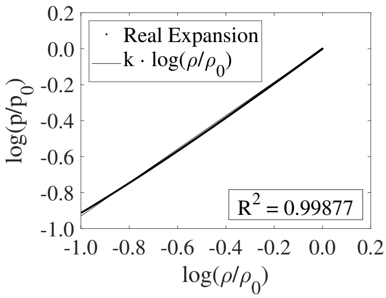

(d) Toluene

Figure 4.6: Results of the linear regressions of $\log(\rho/\rho_0)$ vs $\log(p/p_0)$ along the expansions corresponding to the nozzle shown in Fig. 4.4a corresponding to $\mathrm{Ma_{tg}} = 2.0$

First of all as reported in the charts of Fig. 4.5 and 4.6, for all the analyzed cases the R^2 of the linear regression is always higher than 0.998, highlighting the quality of the regression. As one can notice from Fig. 4.4a, nozzle length and outlet width increase as the average value of k reduces. This behaviour can be ascribed to the increase in the Prandtl-Meyer function, ν, –required to reach a given Mach number– that occurs when the average value of the polytropic exponent reduces, (A. P. S. Wheeler and Ong 2013). Likewise, large influence of working fluid and operative conditions on nozzle shape and size have been observed by Uusitalo et al. (2021).

4.4 Concluding Remarks

In the present chapter an existing Method of Characteristics-based algorithm for the design of the divergent portion of a sharp-edged minimum length supersonic nozzle expanding a perfect gas was reviewed and an extension to dense vapour flows was provided restoring to differential equations of general validity available in published literature. The new algorithm was implemented in MATLAB environment and coupled with CoolProp thermodynamic library for fluid properties evaluation.

The method was applied to several test cases and the effect of the working fluid on nozzle geometry was investigated at two target Mach number values. Particularly, it was observed that the working fluid affects both nozzle outlet width and length and that the effect is amplified as the target Mach number increases. These observations have been explained by means of the average polytropic exponent k of each transformation, computed by means of linear regressions. As a matter of fact, it was observed that as the average value of k along the expansion reduces, nozzle length and outlet width increase. The latter is consistent with the known effect of the average value of the polytropic exponent k on the Prandtl-Meyer function ν required for a target Mach number, which increases as k reduces.

In the next chapter the method will be used to build prismatic 3D stator vanes for RIT nozzles. Particularly, the outcome of the adapted MoC algorithm will represent the core of the divergent section of the 2D profiles that are stacked to build the 3D stator vane.

CHAPTER 5

RIT Supersonic Vane: Efficiency and Downstream Flow Field Uniformity

5.1 Introduction

As seen in Section 2.3, single stage RITs for small scale ORC power plants are usually characterized by considerably high stator discharge Mach number, introducing in the expander design special challenges, which are rarely encountered in the design practice of more conventional turbomachines.

For what concerns the design of convergent-divergent vanes in axial arrangement, larger knowledge derived from ideal gas applications (Goldman 1972; Goldman 1994; Moffitt 1958; Ohlsson 1964), highly loaded stages (Johnston and Dransfield 1959), auxiliary power turbines and rocket turbopumps (Fu et al. 2016) is available. Conversely, extremely scarce information can be found in published literature concerning supersonic RITs operating with ideal gases. A remarkable exception is the work by Reichert and Simon (1997) who presented a design methodology for convergent-divergent RIT stators, that exploits the well-known Method of Characteristics (Shapiro and Edelman 1947a; Shapiro 1953; Shapiro and Edelman 1947b), that allows to design the core of the divergent section to be arranged into a nozzle row.

Over the years considerable research efforts have been spent on topics related to convergent-divergent vanes expanding non-ideal flows, e.g., the extension of CFD RANS flow solver to real gas applications (Hoffren et al. 2002), the comparison of different flow solvers, turbulence and fluid models (Colonna, Rebay, et al. 2006; Harinck, Turunen-Saaresti, et al. 2010), as well as some optimization studies (Harinck, Pasquale, et al. 2013; Pasquale, Ghidoni, and Rebay 2013; Pini, Persico, Pasquale, et al. 2014). Furthermore, some authors have addressed the topic of design methods for convergent-divergent ORC stators (Anand, Colonna, and Pini 2020; Anand, Vitale, et al. 2018; A. P. S. Wheeler and Ong 2013), as well as the working fluid replacement in ORC convergent-divergent stators (M. T. White, Markides, and A. I. Sayma 2018).

Also, for axial turbine vanes, the effect of working fluid on losses has been investigated, both focusing on the link with the fundamental derivative of gas dynamics (Baumgärtner, Otter, and A. P. S. Wheeler 2020) and the compressibility factor (Baumgärtner, Otter, and A. P. S. Wheeler 2021a), as well as the effect of fluid ideality on turbine performance for purely convergent vanes (Giuffre' and Pini 2020).

Nevertheless, design guidelines for convergent-divergent stators operating with non-ideal fluids, particularly in radial arrangement, are still very limited. Likewise, the requirements that should lead the choice towards convergent-divergent vanes are still vague, recommending their adoption for stator discharge Mach ≥ 1.4 –regardless of the working fluid– (Deich 1956), so as to limit downstream mixing loss growth.

It is known that at supersonic discharge expansion fan and shock waves are emanated from the vane TE (F. J. D. Galiana, A. P. Wheeler, and Ong 2016). These waves impinge on the rear suction side of the adjacent vane, and interact with the boundary layer, to be eventually reflected. For this reason the shape of the rear suction side plays a crucial role, as it can reflect and/or generate additional waves, disturbing the downstream flow field in pitch-wise direction and increasing flow non-uniformity. The latter would inevitably increase downstream mixing losses, which may be the predominant loss contributor when complex molecules are considered (Tosto et al. 2021). Moreover, a high downstream non-uniformity, besides promoting the stator-rotor interaction and unsteady loss generation, might also be of structural concern. In fact, as shown by Rinaldi, Pecnik, and Colonna (2016), who performed unsteady calculations on highly supersonic ORC radial turbine, rotor blade can experience very large fluctuations of torque –with sign change– as a result of the highly variable blade loading.

With respect to the stator design, one relevant design parameter is the Mach number achieved within the bladed region, which in turn determines the level of *post-expansion*, that is, the share of the row expansion ratio achieved in the semi-bladed region. A larger post-expansion might lead to larger downstream flow field non-uniformity, which is known to be a possible issue for this class of turbines, and, therefore, mixing loss. While on the one hand a lower post-expansion may reduce the downstream mixing losses, on the other hand it could sharpen the off-design loss growth.

Concerning the vane count, on the one hand, increasing its value may increase flow guidance, but on the other hand it also increases the wetted area and arguably flow losses.

Concerning the outlet flow angle, a high value is desirable to achieve high stage efficiency, particularly at low specific speed, (Rohlik 1968). Nevertheless, for the axial configuration an increase of the outlet flow angle was observed to increase the downstream flow field non-uniformity, because of the wake staying closer to the vane suction side (Anand, Colonna, and Pini 2020).

The purpose of the present chapter is to assess the effect of vane count and outlet metal angle on losses and downstream flow field uniformity for convergent-divergent stators for small scale ORC RITs, making a step towards the derivation of comprehensive design guidelines for ORC supersonic stators. To do so, several stators are designed and analyzed by means of 3D CFD RANS calculations and the results are compared to gain additional insight into the design requirements of these unconventional turbine components.

The work shown in this chapter was presented at the 14$^{\text{th}}$ European Turbomachinery Conference and was published in the *International Journal of Turbomachinery, Propulsion and Power* (Cappiello and Tuccillo 2021b).

5.2 Methodology

To perform the investigation nine 3D stator geometries have been designed by varying the outlet metal angle β_{m} and the vane count Z_N, by means of the vane parametrization presented in section 5.2.1 and implemented in MATLAB environment. Furthermore, the stator geometries have been developed based on the same preliminary design, that is the one considered in Section 2.3 for the first test case using R245fa as working fluid. Subsequently, the stator fluid domains have been meshed in ANSYS TurboGrid and CFD calculations have been run according to the setup described in section 5.2.2. After a mesh sensitivity analysis, described in section 5.2.3, the results are presented in section 5.3. Finally, conclusions are drawn, section 5.4.

5.2.1 Vane Parametrization

The vane parametrization method developed in this work, Fig.5.1, allows to build a convergent-divergent Radial-Inflow Turbine (RIT) nozzle around the non-dimensional divergent nozzle core shaped by means of the Method of Characteristics (MoC) presented in Section 4.2.

First of all, a suitable Mach target, $\mathrm{Ma}_{\mathrm{tg}}$, to be reached at the external throat –end of bladed section, A_{E} in Fig. 5.1, must be chosen. The $\mathrm{Ma}_{\mathrm{tg}}$ value should be lower than Ma_3, the one to be reached at R_3. Hence the $\mathrm{Ma}_{\mathrm{tg}}$ value defines the level of post-expansion, $\Pi_{\mathrm{E}-3} = p_{\mathrm{E}}/p_3$. Once the non-dimensional half nozzle core has been obtained by means of the MoC, Fig. 4.3, it can be scaled up to the right size, in order to accommodate the design mass flow rage, $\dot{m}$. This portion will later constitute the divergent nozzle core, i.e. from section A_{th} to section A_{E}, Fig. 5.1.

The dimensional inner throat width of the nozzle A_{th}, can then be obtained according to Eqn. 5.1, in which ρ_{th} and a_{th} are the density and the speed of sound at the inner throat, while b is the vane height. The dimensional half nozzle contour can be computed from non-dimensional one by means of the scale factor $A_{\mathrm{th}}/2$. Subsequently, the dimensional half nozzle can be mirrored about the horizontal axis, so as to build its specular half.

At this point, the TE of vane 1 is built by drawing half circle of radius R_{TE} equal to half of the desired TE thickness, setting its center at coordinates $(0, R_3 + T_{\mathrm{TE}})$ and aligning it to the desired outlet metal angle, β_{m}.

$$A_{\mathrm{th}} = \frac{\dot{m}}{Z_N \cdot \rho_{th} \cdot a_{th} \cdot b} \tag{5.1}$$

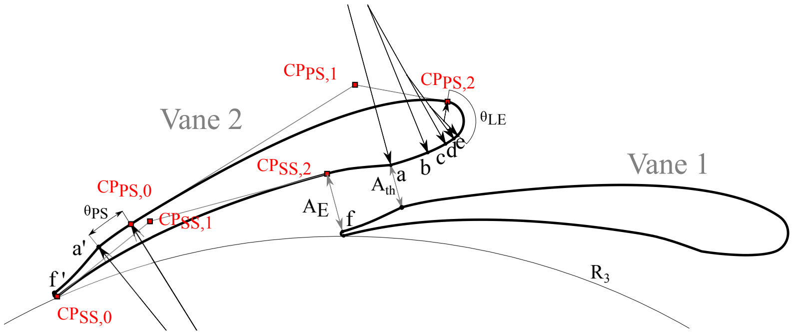

Figure 5.1: Vane parametrization method

The dimensional nozzle is then shifted, so as to make the last point of the right-hand side branch lay at point f, and rotated to make it tangent to the first point of the TE circle.

The right-hand side of the divergent nozzle core and the TE circle of vane 1 are rotated about of an angular pitch $(2\pi/Z_N)$, building the supersonic portion of the pressure side of Vane 2 –from a' to f', Fig. 5.1.

The rear suction side of Vane 2 is built by means of a 2nd order Bezier polynomial, of which the control points $\mathrm{CP_{SS,\,0}}$, $\mathrm{CP_{SS,\,1}}$ and $\mathrm{CP_{SS,\,2}}$ are chosen so as to make $\mathrm{CP_{SS,\,0}}$ coincident with the first point of Vane 2 TE and $\mathrm{CP_{SS,\,2}}$ coincident to the last point of the left-hand side contour of the nozzle divergent section. The Bezier polynomial legs tangency at these two points is insured prescribing the slope of the two legs, computed as the reciprocal of Vane 2 TE diameter slope, in the first case; and the slope of the line passing through the last two points of the left-hand side contour of the nozzle divergent section, in the second case. $\mathrm{CP_{SS,\,1}}$ is then determined as the intersection point of the two legs.

The vane Leading Edge (LE) and the subsonic portion of the vane suction side are built by means of series of circular arcs of decreasing radius from A_{th} to the LE, ($\widehat{\mathrm{ab}}$, $\widehat{\mathrm{bc}}$, $\widehat{\mathrm{cd}}$, $\widehat{\mathrm{de}}$ and $\widehat{\mathrm{eCP_{PS,\,2}}}$) with a similar approach to those used by Reichert and Simon (1997), that allows to have lower curvature where the flow gradients are higher. Finally, the subsonic part of the vane pressure side is built by means of a 2nd order Bezier polynomial, whose construction is similar to the one of the uncovered suction side, and a circular arc $(\widehat{\mathrm{a'CP_{PS,\,0}}})$ with radius and angular extension, θ_{PS}, equal to those of the first circular arc of the subsonic suction side in proximity of the throat $(\widehat{\mathrm{ab}})$.

5.2.2 CFD Setup

Figure 5.2 shows a schematic representation of a sample computational domain investigated in this chapter, together with the boundary conditions adopted for the CFD analysis. Particularly, exploiting the geometrical periodicity of the system, only one passage per row was modelled by means of periodic boundary conditions, depicted in red in Fig. 5.2. Furthermore, all computational domains investigated in this section have been enlarged downstream with respect to the rotor inlet radius found in the meanline design –shown in green in Fig. 5.2– not to constrain the flow solution at that location. The computational domain was further bounded by hub and vane surfaces, shown in grey in Fig. 5.2 and shroud surface (not shown in the schematic), that were treated as adiabatic, with no-slip condition. Flow boundary conditions, at blue surfaces in Fig. 5.2, have been provided by means of inlet total pressure, p_0, total temperature, T_0, and inlet flow direction, while the outlet boundary condition has been provided via the static pressure p.

As mentioned at the beginning of the present section, the stator geometries analysed in the present work have been built based on the preliminary design specifications from the first test case of section 2.3, that considered R245fa as working fluid. Consequently, the values of the inlet flow boundary conditions have been set accordingly. Conversely, the outlet static pressure was set to about 3.25 bar, so to reach at R_4 a static pressure as close as possible to the one found at rotor inlet in the preliminary design. Furthermore, strong averaging option was selected at the outlet flow boundary to avoid wave reflections. Table 5.1 summarizes the boundary conditions adopted for the stators CFD analysis.

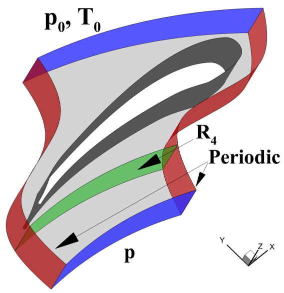

Figure 5.2: CFD setup schematic

Fluid	$p_{0,\mathrm{In}}$	$T_{0,\mathrm{In}}$	α_{In}	p_{Out}
-	(bar)	(K)	(°)	(bar)
R245fa	28	439	45	3.25

Table 5.1: Boundary conditions for stators CFD analysis

All geometries have been analysed by means of viscous 3D CFD RANS calculation carried out in ANSYS Fluent v17.1, by means of density-based flow solver with implicit formulation.

For flux scheme the Roe-FDS method was selected. Concerning the spatial discretization, gradients have been computed via least square cell based scheme, while second order upwind was used for flow and turbulence. Turbulence problem closure was obtained by mean of the $k-\omega$ SST model. Fluid thermodynamic properties have been obtained by REFPROP (E. W. Lemmon, Huber, and McLinden 2010), via Fluent built-in routines.

Finally, a Courant number equal to 5 was used, however, to improve convergence a first order solution was obtained before switching to second order.

5.2.3 Mesh Sensitivity Analysis

A mesh sensitivity analysis was carried out on a single geometry with intermediate features with respect to those of the profiles investigated in the present chapter, Tab. 5.2. Four meshes, whose main features are summarized in Tab. 5.3, have been generated starting from a baseline mesh and progressively refining the average mesh spacing, h Eqn. 2.50, so as to provide a mesh refinement r Eqn. 2.49, always above 1.3 (Roache 1994, 1997; Roache, Ghia, and F. M. White 1986). Furthermore, to reduce the computational effort all meshes have been built with an average y^+ equal to 25, therefore, resorting to wall functions.

Re_c	Ma_4	c (mm)	Z_N	β_m (°)	A_{th} (mm)	R_3 (mm)
$5.86 \cdot 10^6$	1.66	12.8	15	75	1.36	≈ 22

Table 5.2: Characteristic features of the convergent-divergent vane used for the mesh sensitivity analysis

Mesh #	Volume (m^3)	Cells Count ($\cdot 10^{-6}$)	h (m)	r
1	$1.54 \cdot 10^{-7}$	0.122	$1.08 \cdot 10^{-4}$	-
2	$1.54 \cdot 10^{-7}$	0.287	$8.12 \cdot 10^{-5}$	1.33
3	$1.54 \cdot 10^{-7}$	0.679	$6.10 \cdot 10^{-5}$	1.33
4	$1.54 \cdot 10^{-7}$	1.604	$4.58 \cdot 10^{-5}$	1.33

Table 5.3: Characteristic features of computational meshes used for mesh sensitivity analysis

The main results of the mesh sensitivity analysis are presented in Tab. 5.4, that shows several mass-weighted quantities of interest (e.g., static pressure, p, absolute flow angle, α, entropy, s, kinetic energy, E_k, and Mach number, Ma), together with some of the most important performance index (e.g., kinetic loss coefficient, ζ, and stator efficiency, η), all expressed as percentage deviation with respect to the finest mesh. As one can notice, apart from the entropy variation at rotor inlet radius, Δs_4, the deviation with respect to finest mesh results are extremely tight. Nevertheless, despite the average mid-span pitch-wise distributions at R_4 of static pressure and outlet flow angle, shown with dash–dotted line in Fig. 5.3a and b, appear extremely close, the mid-span pitch-wise distributions, shown with solid line, unveil

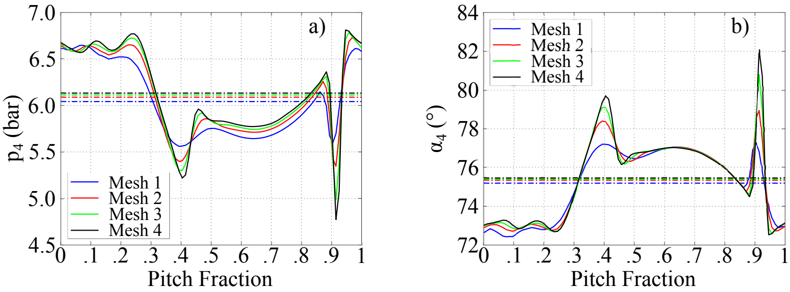

Figure 5.3: Mid-span pitch-wise distribution at R_4, solid line, and arithmetic average, dash-dotted line: static pressure a) outlet flow angle b).

that coarser meshes provide dramatically smoothed out trends, with differences between coarsest and finest mesh that peaks up to 20%.

This occurrence can be explained by a poor resolution of the expansion fans and shock waves provided by the coarsest mesh. This can be clearly seen in Fig. 5.4 and 5.5, in which it is also possible to appreciate the improvements of TE patter resolution obtained with finer meshes.

	Mesh #			
	1	2	3	4
$\Delta p_4(\%)$	2.2710	1.0476	0.4601	0
$\Delta\alpha_4(\%)$	0.2484	0.0786	0.0418	0
$\Delta s_4(\%)$	-12.031	-3.8900	0.0304	0
$\Delta E_{\mathrm{k}4}(\%)$	-0.7188	-0.3013	-0.0959	0
$\Delta \mathrm{Ma}_4(\%)$	-0.3212	-0.2014	-0.1476	0
$\Delta\zeta_4(\%)$	-8.4196	-2.3310	0.6954	0
$\Delta\eta_{\mathrm{s}}(\%)$	0.6587	0.1997	-0.0247	0

Table 5.4: Main results of the Mesh sensitivity analysis expressed as percentage deviation with respect to the finest mesh result

Considering that the focus of work is also on the downstream flow field non-uniformity, to which the expansion fans and shock waves appear to contribute largely, an average mesh spacing h corresponding to the third mesh was deemed appropriate to provide a sufficient resolution of expansion/compression waves. As an example, the computational mesh of the geometry featuring 15 vanes and 75° outlet metal angle, obtained with an

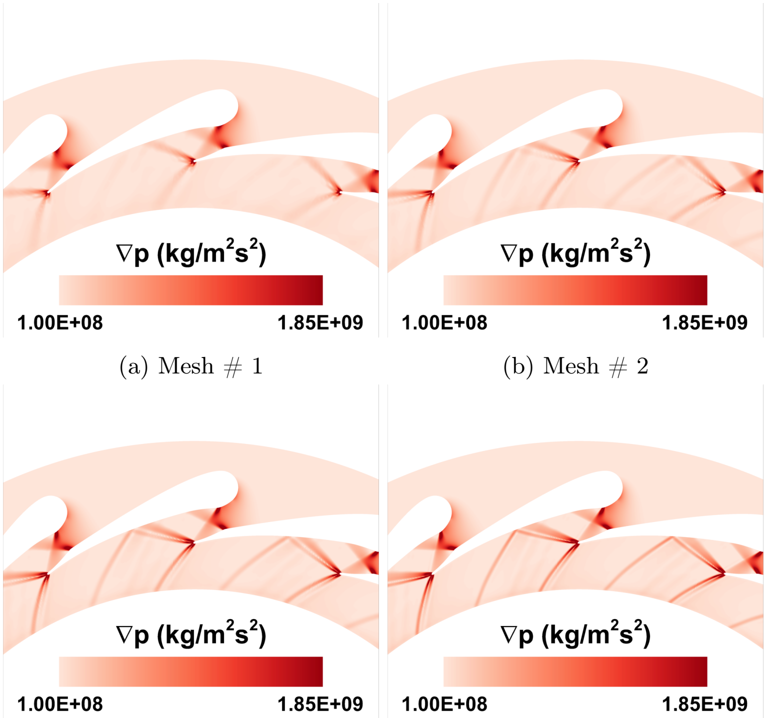

(a) Mesh # 1 (b) Mesh # 2

(c) Mesh # 3 (d) Mesh # 4

Figure 5.4: Mid-span pressure gradient distribution obtained by means of the four meshes used for the mesh sensitivity analysis

average mesh spacing $h = 6.10 \cdot 10^{-5}$ m is presented in Fig. 5.6.

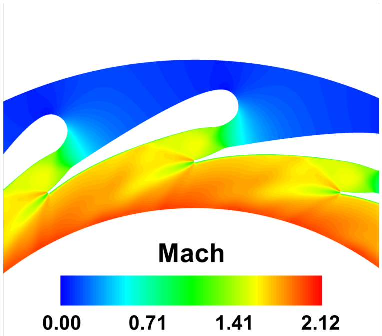

(a) Mesh # 1

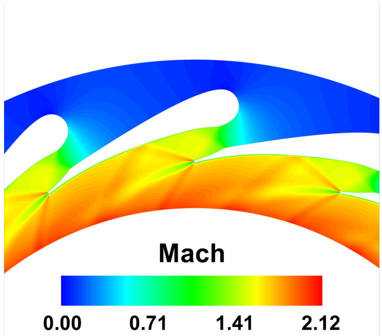

(b) Mesh # 2

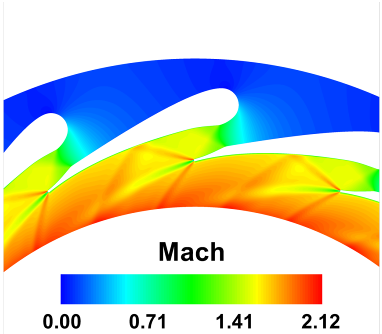

(c) Mesh # 3

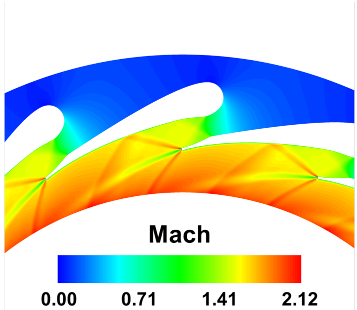

(d) Mesh # 4

Figure 5.5: Mid-span Mach distribution obtained by means of the four meshes used for the mesh sensitivity analysis

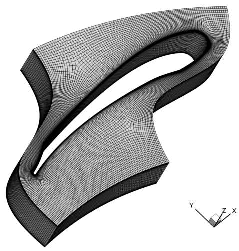

Figure 5.6: Computational mesh of $Z_N = 15 - \beta_m = 75°$ geometry

5.3 Results

Several RIT convergent-divergent vanes have been designed by means of the method presented in Section 5.2.1, varying the vane count Z_N and the outlet metal angle β_{m}. Particularly, 3 vane count values (10, 15, 20) and 3 outlet metal angle values (70°, 75°, 80°) have been considered, resulting in 9 geometries. Furthermore, all nine geometries share the same target Mach number, $\mathrm{Ma}_{\mathrm{tg}}$, required by Method of Characteristics, Section 4.2. More specifically, in all investigated cases $\mathrm{Ma}_{\mathrm{tg}}$ was set to 1.55, while the required Mach at stator discharge, Ma_3, from meanline design is 1.66. This choice ensures a further expansion up to the vane TE, which is known to provide a stabilizing effect on the state of the boundary layer. Consequently, the expansion ratio achieved in the bladed region, $\Pi_{\mathrm{th-E}}$, is equal to 2.14, while the one achieved in the semi-bladed region, $\Pi_{\mathrm{E-3}}$, that is the post-expansion, is 1.27.

It is worth mentioning that upon designing the investigated profiles, the distance between stator TE and rotor LE radii was kept constant and equal to the value found in the meanline design. Furthermore, the stator TE thickness was defined as a percentage of the inner throat, A_{th}, and was kept unchanged from case to case. As A_{th} scales with the vane count, this approach allows preserving the same TE thickness-to-pitch ratio –equal to $1.49 \cdot 10^{-2}$, so as to induce the same blockage by the TE, while making the actual one only dependent on the state of the boundary layer.

Figure 5.7 presents for the $Z_N = 15 - \beta_m = 75°$ configuration the mid-span static pressure, Fig. 5.7a, Mach number, Fig. 5.7b, and total pressure, Fig. 5.7c, distributions together with the superposition of the streamlines,

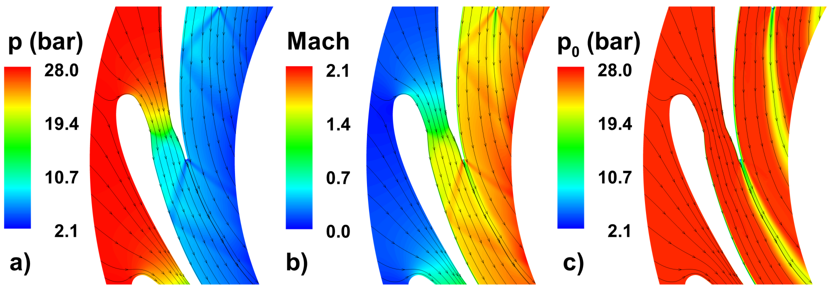

Figure 5.7: Mid-span contour of $Z_N = 15 - \beta_m = 75°$ geometry: static pressure a); Mach number b); total pressure c).

making possible to identify all the characteristic features of the flow field. Particularly, static pressure and Mach number distributions allow a clear visualization of the TE flow structures and, according to the streamlines deflection direction, one can distinguish between expansion fans and shock waves. Finally, the total pressure distribution allows to easily detect the wake behind the TE as a total pressure deficit region.

Finally, the CFD results allowed assess the suitability of the assumptions made in the MoC-based algorithm: as a matter of fact, the mass-weighted average Mach from CFD at the inner throat, A_{th}, resulted to be 1.04, against 1 (as assumed for the inverse sharp-edged nozzle design), while at the external throat, A_{E}, the mismatch between CFD and MoC-based results are well within 1%.

5.3.1 Flow Structures

The mid-span pressure gradient contours shown in Fig. 5.8 allow an easier identification of the flow structures that, as will be explained in the forthcoming, are the main driver of the downstream flow field non-uniformity in pitch-wise direction.

Particularly, several common features can be identified, such as the double expansion fan at the inner throat A_{th}, together with the TE flow structures, made up of the following features:

- Left-Running (LR) expansion fan, label A, Fig. 5.8.
- LR shock, label B in Fig. 5.8, slightly downstream of A.
- Right-Running (RR) expansion fan, reflected by the suction surface of the adjacent vane as a LR expansion fan, label C.
- RR shock, reflected by the suction surface of the adjacent vane as a LR shock, label D.

Furthermore, other peculiar set of waves, labels E' and E'', can be identified. These are two sets of in-passage compression waves originated by the suction side curvature featured by these designs.

- E' is located at the beginning of the uncovered suction side.
- E'' is located towards the stator TE.

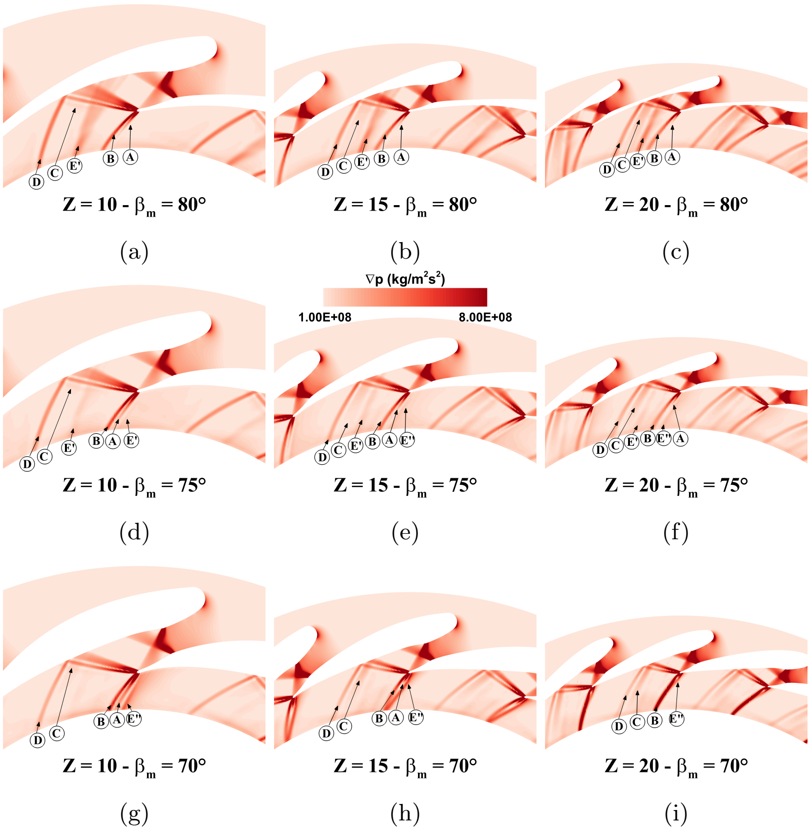

Figure 5.8: Mid-span pressure gradient contours of the 9 investigated configurations

Interestingly, both the vane count, Z_N, and the outlet metal angle, β_m, appear to affect the occurrence and intensity of these two additional sets of waves, E' and E'', via the different curvature distribution which results by the combination of Z_N and β_m. However, the effect of the outlet metal angle appears predominant. The following cases can be identified:

- At high β_m, only E' is present, e.g. Fig. Figs. 5.8a–5.8c.

- At medium values of β_m, both E' and E'' are present, although the former appears shifted downstream with respect to the high β_m case, and the latter is only of weak intensity.

- At low β_m, only E'' arises. However, a particular case can be seen in $Z_N = 20 - \beta_m = 70°$ case, Fig. 5.8i, in which the E'' is so close to the TE, that it is difficult to distinguish it from the LR shock B. Also, the two substantially merge while travelling downstream, making difficult to identify the LR expansion fan A.

5.3.2 Pitch-wise Distributions

The flow structures analysed in the previous section have a crucial effect on the pitch-wise distribution and, therefore, on the downstream flow field uniformity, featured by the geometries. Figure 5.9 and 5.10 shows the mid-span pitch-wise static pressure distributions evaluated at the R_4 surface. However, in Fig. 5.9 the distributions are grouped by common vane count Z_N, while in Fig. 5.10 they are grouped by outlet metal angle β_m. Additionally, the pitch-wise distributions are expressed as percentage deviation with respect to their average value and are presented as a function of the non-dimensional angular pitch. It is also worth to specify that the pitch fraction 0 actually refers to the right-hand side corner of the computational domain, while pitch fraction 1 refers to the left-hand side corner, Fig. 5.2.

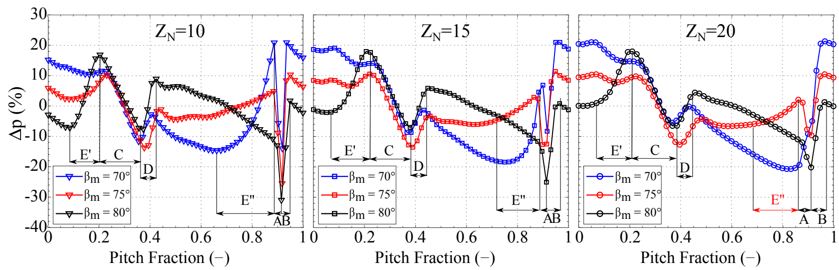

Figure 5.9: Mid-span pitch-wise distribution evaluated at R_4 of the static pressure, expressed as percentage deviation with respect to the average values as a function of the non-dimensional pitch fraction. Distributions grouped by common vane count Z_N

With respect to $Z_N = 10$ case in Fig. 5.9, several regions can be identified:

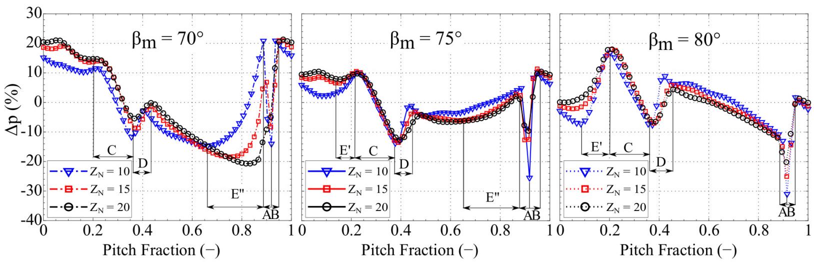

Figure 5.10: Mid-span pitch-wise distribution evaluated at R_4 of the static pressure, expressed as percentage deviation with respect to the average values as a function of the non-dimensional pitch fraction. Distributions grouped by common outlet metal angle β_m

- At low pitch fractions, namely 0–0.1, that corresponds to region behind the TE, a slightly decreasing trend can be observed. The latter can be ascribed to the wake, and only has a minor effect on the distribution itself.
- At pitch fractions 0.1–0.2, a sudden rise, related to the compression waves (E′), can be seen for $\beta_m = 75°$ and 80°. Consistently with the pressure gradient contour of $Z_N = 10 - \beta_m = 70°$ case, Fig. 5.8g, where no (E′) was detected, the corresponding pitch-wise distribution does not show the above-mentioned pressure rise that characterizes the other two configuration. Furthermore, the pressure rise seen in Fig. 5.9 is much larger for $\beta_m = 80°$, consistently with the larger curvature featured by this geometry at the start of the uncovered suction side.
- At pitch fractions 0.2–0.35 all cases show a decrease of similar magnitude, as these pitch fractions are reached by streamlines that have passed through the reflected LR expansion fan (C).
- At pitch fractions ≈ 0.35–0.4 a re-compression can be noticed, as these pitch fractions are reached by streamlines that have also passed through the reflected shock (D).
- Further ahead, at pitch fractions 0.4–0.85, different trends can be observed according to the value of β_m:
  - For $\beta_m = 70°$, after an initial decrease, the distribution start

rising again rapidly due to the effect of compression waves E'', located almost at the TE.

- For $\beta_m = 80°$, a decreasing trend can be seen, as a result of the lower curvature of the final part of the vane suction side, that does not lead to E'' set to arise.
- For $\beta_m = 75°$, an intermediate trend with respect to the previous two can be seen, with a milder increase due to milder E'' waves.

- At about pitch fraction 0.9, all cases show a decreasing trend, as these pitch fractions are reached by streamlines that have also passed through the LR expansion fan A.
- After pitch fraction 0.9 the trend rises again due to streamlines that have passed through LR shock B.
- Finally, a slightly decreasing trend can be observed towards pitch fraction 1, that is again behind the TE region.

Similar pressure patterns can be observed for $Z_N = 15$ and 20, with the exception of $Z_N = 20 - \beta_m = 70°$, for which E'' is practically merged with the LR TE shock B.

Differently from Fig. 5.9 in which the pitch-wise distributions have been grouped by common vane count Z_N, Fig. 5.10 shows the same pitch-wise distributions although grouped by common outlet metal angle β_m. Interestingly, in the latter case, the distributions almost collapse one on top the other with much better matching. This suggests that the outlet metal angle has a much stronger effect then the vane count.

Finally, Fig. 5.11 shows the mid-span pitch-wise distributions of the absolute flow angle, presented as a function of the non-dimensional pitch fraction. The distributions are evaluated at rotor inlet radius and are expressed as percentage deviation with respect to the average values. Although in this case max deviations from the average values do not exceed 15%, the trends are substantially unaltered with respect to those of static pressure. However, this should not surprise, as most of the above-mentioned features are due to streamlines passing through Mach waves.

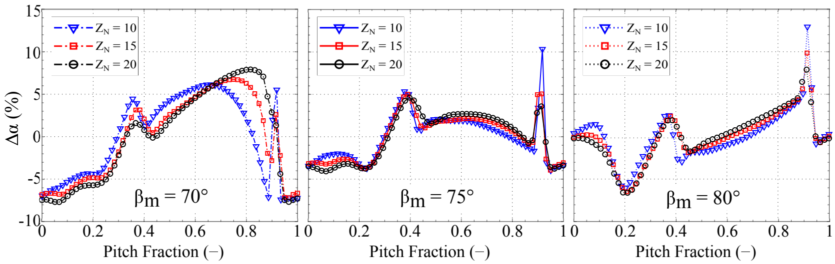

Figure 5.11: Mid-span pitch-wise distribution evaluated at R_4 of the absolute flow angle, expressed as percentage deviation with respect to the average values as a function of the non-dimensional pitch fraction. Distributions grouped by common outlet metal angle β_m

Vane Count Effect

To assess the effect of the vane count Z_N, the most suitable charts are those of Fig. 5.10, in which the mid-span pitch-wise distribution obtained at different Z_N can be compared directly. The overall effect the vane count on the mid-span pitch-wise distribution appear modest, particularly at $\beta_m = 75°$ and $80°$. Additionally, the major effects are confined to the magnitude of pressure change due to E$'$ and to the LR expansion fan and shock, A and B, with sharper trends attaining to lower vane counts. Differences induced by Z_N are enhanced only for $\beta_m = 70°$ cases, at pitch fractions attaining to the effect of E$''$, which occur earlier as the vane count is lowered.

Outlet Metal Angle Effect

As it can be seen in Figure 5.9, rather different trends are obtained at pitch fractions between those affected by the LR shock D and the LR expansion fan A. In fact, this is consistent with the fact that no E$''$ set of waves is present in the $\beta_m = 80°$ cases, while 70° and 75° both feature this set of waves, although of different intensity. Particularly, at pitch fraction between the LR shock D and the LR expansion fan A, the following trends can be observed:

- For $\beta_m = 80°$ a decreasing trend can be seen, as no E$''$ set is present for these cases.

- For $\beta_m = 75°$ an increasing trend can be seen after pitch fraction ≈ 0.6.
- For $\beta_m = 70°$ the trend is initially decreasing, followed by a sharp rise.

It is also worth noticing that the case $\beta_m = 80°$ is the one that features the deeper valley due to the LR expansion fan A.

Finally, similar conclusions can be drawn for the absolute flow angle mid-span pitch-wise distributions.

5.3.3 Global Trends

To sketch the overall picture of the stator performances, several figure of merits have been used for both stator losses and downstream flow field uniformity. Concerning the former, three coefficients have been considered, i.e. the total pressure loss coefficient Y, Eqn. 5.2, the kinetic loss coefficient ζ, Eqn. 5.3, and the stator efficiency η, Eqn. 5.4, all evaluated taking as outlet section the rotor inlet radius.

$$\mathrm{Y} = \frac{p_{0,\,\mathrm{In}} - p_{0,\,\mathrm{Out}}}{p_{0,\,\mathrm{Out}} - p_{\mathrm{Out}}} \cdot 100 \tag{5.2}$$

$$\zeta = \frac{c^2_{\mathrm{out,\,ise}} - c^2_{\mathrm{out}}}{c^2_{\mathrm{out,\,ise}}} \cdot 100 \tag{5.3}$$

$$\eta = \frac{h_{0,\,\mathrm{In}} - h_{\mathrm{Out}}}{h_{0,\,\mathrm{In}} - h_{\mathrm{Out,\,ise}}} \cdot 100 \tag{5.4}$$

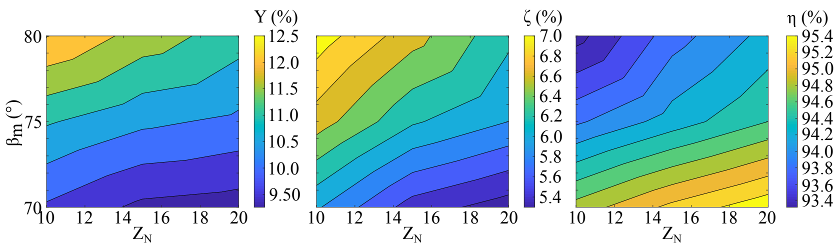

Figure 5.12: Distribution of stator performance coefficients within the investigated design space: total pressure loss coefficient Y, kinetic loss coefficient ζ, stator efficiency η, Equations (5.2)–(5.4)

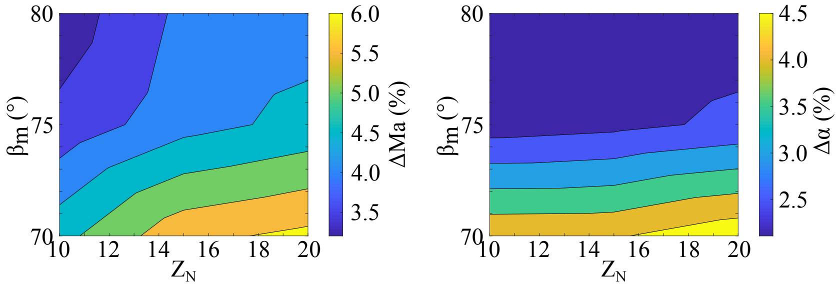

Figure 5.13: Distribution of Mach and absolute flow angle pitch-wise non-uniformity within the investigated design space evaluate by means of Eqn. 5.5

To assess the pitch-wise non-uniformity levels, several quantities have been evaluated taking the mid-span pitch-wise distributions at rotor inlet radius R_4, Fig. 5.2, by means of the figure of merit of Eqn. 5.5. The latter measures the deviation of the pitch-wise distribution of a general quantity of interest, χ, from its average value, $\overline{\chi}$, normalized both with respect to the average values $\overline{\chi}$ and to the angular pitch extension $\Delta\theta_{\text{pitch}}$.

$$\Delta\chi = \frac{\int_0^{\theta_{\text{pitch}}} |\chi - \overline{\chi}|\, d\theta}{\Delta\theta_{\text{pitch}}} \cdot \frac{100}{\overline{\chi}} \tag{5.5}$$

Figure 5.12 presents the contour of the figures of merit select to depict stator loss as a function of vane count Z_N and outlet metal angle β_m. Clear trends can be observed and all coefficients provide the same picture: higher losses occur at low vane count and high outlet metal angle, while the optimum appears located at the opposite side of the map, with losses decreasing for increasing values of the vane count and decreasing values of the outlet metal angle. Furthermore, the loss increase observed for a vane count reduction is consistent with the trends found by A. P. S. Wheeler and Ong (2013).

Figure 5.13 presents the Mach number, ΔMa, and absolute flow angle, $\Delta\alpha$, pitch-wise non-uniformity contour as a function of vane count Z_N and outlet metal angle β_m, both computed by means of Eqn. 5.5 considering the mid-span pitch-wise distributions at rotor inlet radius, R_4. As one can notice, opposite trends with respect to those of stator losses can be detected, with the lowest non-uniformity achieved at low vane count Z_N and high outlet metal angle β_m. Furthermore, the absolute flow angle non-uniformity level appears only weakly affected by the vane count. Also, lower non-uniformity levels can be observed at lower vane count Z_N, despite the sharper trends seen in Figs. 5.9–5.11. Finally, the conflicting trends of stator efficiency and stator downstream uniformity observed in this section suggest the need of multi-objective optimization strategies.

5.3.4 Analysis of Optimal Stator Vanes

The previous section showed conflicting trends between stator efficiency and stator downstream flow field uniformity. Therefore, depending on the target selected, different optimal candidates are found. Following, an in-depth analysis of these two stator configurations is presented, focusing both on non-ideal effects and pitch-wise non-uniformity. The vane profile selected from optimal stator efficiency point of view, i.e., the $Z_N = 20 - \beta_m = 70°$ configuration, is referred to as case 1, whereas the optimal downstream uniformity configuration, i.e., the $Z_N = 10 - \beta_m = 80°$ case, is referred to as case 2.

To gain further insight into the gas-dynamic behaviour and the non-ideal effects taking place with the stator passages, the mid-span contours of fundamental derivative of gas-dynamic, Γ, speed of sound, a, Mach number, Ma, and pressure gradient, ∇p, have been investigated and are presented in Figs. 5.14–5.15 for case 1 and 2, respectively.

As clearly visible in the Γ contour Fig. 5.14a and 5.15a, for both cases, the expansion process occurs almost entirely at $\Gamma < 1$. As a consequence, the gas-dynamic behaviour is non-ideal in almost all the domain, although the non-ideality is expected to reduce towards the domain exit, where Γ values approach 1.

The most relevant non-ideal effect can be observed in Fig. 5.14b and 5.15b, where one can notice generally increasing values of the speed of sound through all the expansion from inlet to outlet of the domain. Additionally, the speed of sound values encountered in the flow field are low in comparison to those typically encountered for other substances, such as air. This circumstance is a combined of non-ideality of the flow and of the high molecular weight featured by the R245fa, like most organic fluids, entailing relevant compressibility effects.

Finally, mid-span Mach and pressure gradient contours, shown in Figs. 5.14c and 5.15c and Figs. 5.14 and 5.15, for both case 1 and 2, provide a clear visualization of the peculiar flow structures previously discussed.

Further quantitative insight into the non-ideal effects that occur within the stator passages can be gained by means of Fig. 5.16. The latter presents

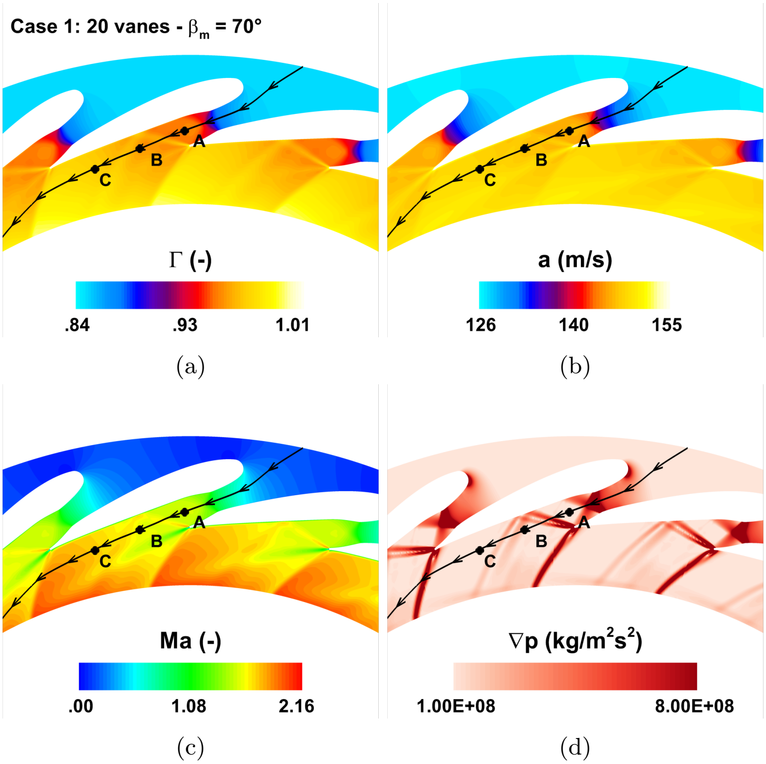

(a) (b) (c) (d)

Figure 5.14: Stator mid-span contour; case 1

the values of density, fundamental derivative, speed of sound and Mach number found along the streamline passing through the inner throat center, shown in black in Fig. 5.14 and 5.15, extracted from the CFD calculations.

As one can see in Fig. 5.16a, extremely large density changes occur from inlet to outlet of the stator domains along the mid-channel streamline, and particularly, within the first half of the streamwise length. In both cases the streamline can be seen to experience some density ripples, particularly from $\approx 40\%$ of the streamwise length. This non-monotone change is to be ascribed to the sequence of expansion fans and shocks encountered by the flow particles along the flow path. Particularly, the labels reported both in the contour plots, Fig. 5.14 and 5.15, and in the mid-channel streamline chart, Fig. 5.16a, allow to identify the corresponding flow structure more

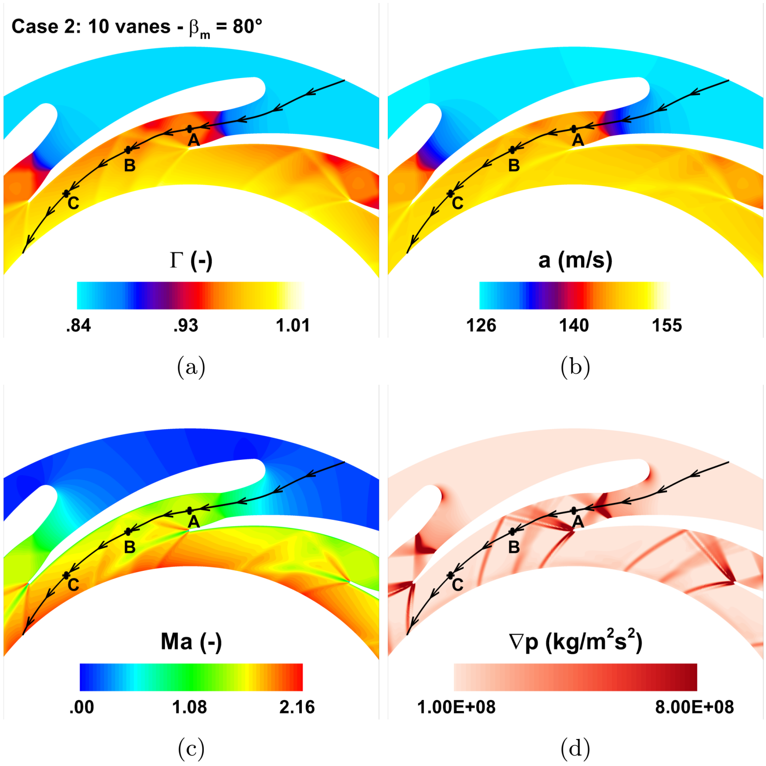

(a) (b) (c) (d)

Figure 5.15: Stator mid-span contour; case 2

easily. In fact, the label **A** is located within the bladed region, upstream of the RR branch of the TE expansion fan; the label **B** is located in the uncovered suction side region, downstream of the RR branch of the TE shock; while the label **C** is located in the rear suction side region, downstream of the reflected RR shock from stator TE.

As shown in Fig. 5.16b, $\Gamma < 1$ is encountered at almost all streamwise length values along the streamline. Similarly to the density distribution, some ripples are found in the Γ chart. However, these should not be ascribed to a non-monotone thermodynamic behaviour of the fluid, but, rather, to the non-continuous expansion due to sequence of expansion fan and shock wave encountered by the streamlines.

Relevant non-ideal effects can be seen in Fig. 5.16c, where the speed of

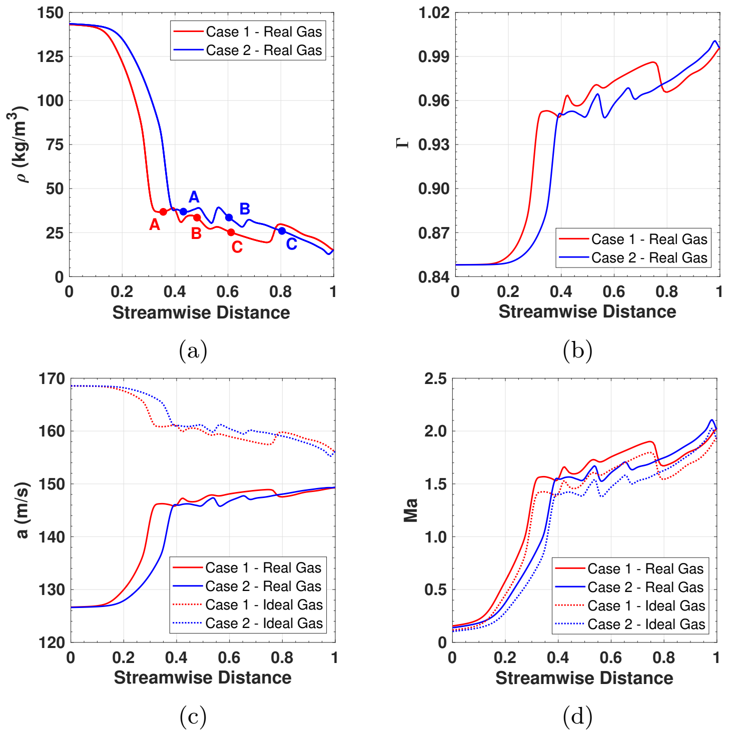

Figure 5.16: Changes of density (a), fundamental derivative (b), speed of sound (c) and Mach number (d) extracted from CFD of stator 1 and 2 along the mid-channel streamline.

sound values, a, extracted from the CFD along the streamlines, are shown with solid line in red and blue (case 1 and 2, respectively). While for an ideal gas the speed of sound values are expected to decrease along an isentropic expansion, values found along the streamlines exhibit the opposite trend, rising almost continuously from inlet to outlet. Once again, the small ripples are due to the non-continuous expansion occurring along the streamline.

As a further comparison to illustrate the non-ideal effects, for both case 1 and 2, together with values extracted from the CFD calculations, the ideal gas speed of sound, $a_{\text{ideal gas}}$, is shown with dotted line in Fig. 5.16c. The ideal gas speed of sound was computed as in Eqn. 5.6, in which $\mathcal{R}$ is the universal gas constant, $\mathcal{M}_{\text{R245fa}}$ is the molecular mass of the R245fa, while

γ and T are the specific heat ratio and the absolute temperature extracted from the CFD calculations along the streamline.

$$a_{\text{ideal gas}} = \sqrt{\gamma \frac{\mathcal{R}}{\mathcal{M}_{\text{R245fa}}} T} \tag{5.6}$$

Most notably, ideal and real gas speed of sound exhibit opposite trends, with the ideal gas speed of sound decreasing from inlet to outlet. Furthermore, much higher values are encountered in the ideal gas case, particularly at the inlet. However, the difference between the two trends decreases along the streamline length, as the non-ideal effects weakens, that is when Γ approaches 1.

Mach number values corresponding to the velocity magnitude found along the streamline are shown for both the ideal and real gas speed of sound in Fig. 5.16d. Particularly, while in the latter case the Mach number was extracted directly from the CFD results, in the former case the Mach number was computed taking the ratio of the velocity magnitude from the CFD calculations and the ideal gas speed of sound, Eqn. 5.6. While in both ideal and non-ideal cases similar trends are found, slightly lower values are observed in the ideal gas-based Mach number, as a result of higher speed of sound values, Fig. 5.16c.

It is worth to observe that these findings do not contradict other results available in published literature, e.g., those by Spinelli et al. (2018), that show the Mach number to decrease for increasing levels of non-ideality. In fact, in the cited work, the whole expansion was studied at different levels of non-ideality, which leads also the volumetric behaviour of the expansion and the temperature drop to be affected due to the different values of the compressibility factor Z. Therefore, affecting the velocity magnitude too.

Concerning the stator downstream uniformity and the pitch-wise distributions, a large non-uniformity can be noticed for both case 1 and 2 in Fig. 5.17, that shows the mid-span Mach number and absolute flow angle pitch-wise distribution at rotor inlet radius. This non-uniformity is due to the fact that each pitch fraction is reached by streamlines that have passed through a different number of compression/expansion waves, as discussed in Section. 5.3.2. Pitch-wise distributions of case 1, Fig. 5.17, show smoother trends, although larger deviations from the average values are found. Conversely, more uniform pitch-wise distributions can be noticed in case 2, but sharper trends are present. However, due to the large pitch-wise non-uniformity, large changes of local velocity triangles at rotor inlet

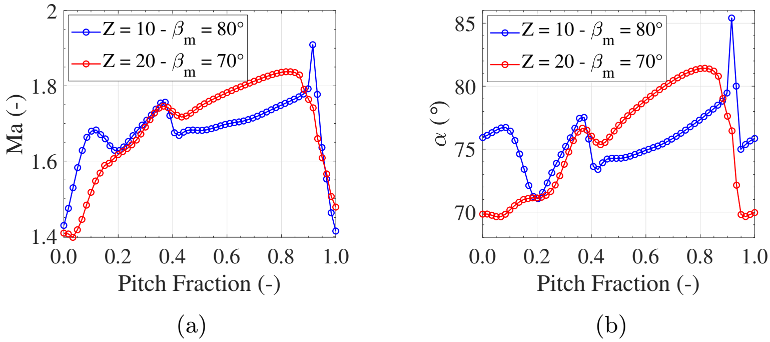

Figure 5.17: Mid-span pitch-wise distribution of Mach number (a) and outlet flow angle (b) at rotor inlet radius

radius are found along the pitch, as shown in Fig. 5.18. Particularly, this figure allows to draw several conclusions by comparing the mid-span pitch-wise averaged velocity triangles from CFD, shown in black, the meanline design requirement in grey and the local (maximum and minimum) velocity triangles, in red and blue, respectively.

First of all, the mid-span pitch-wise averaged velocity triangles from CFD agree surprisingly well with the meanline design specification, shown in grey, clearly showing the suitability of the design method. Nevertheless, if the velocity triangles are computed at pitch-wise locations where maximum and minimum Mach number occur, Fig. 5.17a, the picture becomes substantially different. In fact, these velocity triangles, shown in red and blue in Fig. 5.18 depart from the meanline design prescription, as well as from CFD average, dramatically. Thus, wide changes of the local velocity triangles and, therefore, of rotor blade incidence, occur along the pitch. This inevitably makes the rotor blade prone to flow separations, alternating stress and power output fluctuations.

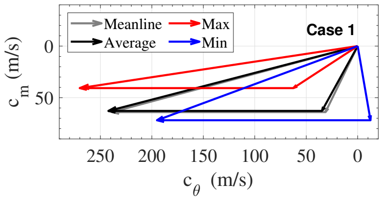

(a) Case 1

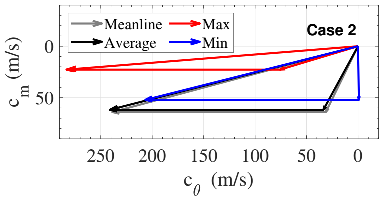

(b) Case 2

Figure 5.18: Mid-span velocity triangles at rotor inlet radius.

5.4 Concluding Remarks

In the present chapter nine ORC RIT convergent-divergent stator vanes were designed by means of a simple vane parametrization. The stators were designed to expand R245fa, according to the boundary conditions and preliminary design specifications coming from a previous chapter of this thesis. The methodology used for the stator design relies on the inverse design of sharp-edged minimum length nozzle obtained by means of a MoC-based algorithm, whose adaptation to dense gases was provided in a previous chapter. The vane parametrization allows the user to set stator outlet radius, vane height, vane count, outlet metal angle and design mass flow rate, therefore, it fits well into a turbomachinery design workflow. The effectiveness of the design method was proven comparing the CFD averaged quantities, both at inner and exit throats, as well as stator outlet velocity triangles, against the meanline design specification, showing that an excellent agreement is achieved.

The design method was used to carry out a parametric analysis, varying stator vane count and the outlet metal angle, while all the stators presented in this chapter share the same target Mach number for the MoC.

The CFD analysis of the stators allowed to assess the combined effect of the vane count and the outlet metal angle on stator losses and stator downstream flow field non-uniformity –for which a novel figure of merit was introduced.

Results unveiled conflicting trends between optimal stator efficiency and stator downstream uniformity, which suggests resorting to multi-objective optimization strategies. Moreover, further insight into the phenomena driving the downstream pitch-wise non-uniformity was gained by means of the mid-span pressure gradient contours, that allowed to visualize the Mach waves, so as to assess their influence on pitch-wise distributions.

Subsequently, the effect of vane count and outlet metal angle on flow structures were assessed and correlated to the levels of non-uniformity at rotor inlet radius. Overall, the effect of the vane count was found to be modest, although sharper trends were observed at lower vane count values. Conversely, the outlet metal angle was seen to have a strong impact on downstream pitch-wise distributions and sharper trends were noticed at higher outlet metal angles.

Furthermore, an in-depth analysis was provided for the stators selected for optimal efficiency and optimal downstream uniformity, providing qualitative and quantitative assessments of the non-ideal effects occurring in the stator passages. Additionally, for the two optimal stators, the effect of the downstream pitch-wise non-uniformity on the local velocity triangles, and their departure from the CFD average and meanline design specification, was shown.

The results of the present chapter provide a novel contribution particularly for what concerns the effects of the vane count and the outlet metal angle, as well as the conflicting trends between optimal stator efficiency and downstream flow field uniformity.

Possible extensions of the present work concern the study of a broader design space, so as to include the target Mach number for the MoC in the analysis. Also, the adoption of higher order Bezier polynomials would provide more flexibility to determine the rear suction side curvature distribution, although reducing the ease of use of the method. Finally, a multi-objective optimization of the stator profiles is recommended.

CHAPTER 6

Unsteady Stator-Rotor Interaction

6.1 Introduction

Single stage RITs for ORC applications can exhibit exceptionally high stator discharge Mach numbers, as also shown in previous chapters of the present thesis. This peculiarity poses relevant challenges from both design point of view and computational tools required.

Nowadays, the standard practice for turbomachinery blade design still relies on steady-state RANS calculations, adopting a mixing-plane for the stator-rotor interface. Nevertheless, the mixing-plane can introduce several complications when high stator discharge Mach is encountered. First of all, a relevant issue concerns the reflective behaviour of the mixing-plane implemented in several flow solvers. However, non-reflective implementations have also been developed (Vitale, Pini, and Colonna 2020).

Another source of inaccuracy associated with the use of steady-state calculations for high stator discharge Mach numbers concerns the unsteady interaction between the stator TE shock system and the rotor LE, which is completely neglected in steady calculations. In fact, this approximation has been shown to lead to increasing discrepancy between steady and unsteady stage efficiency prediction as the stator discharge Mach number increases (Rubechini, Marconcini, Giovannini, et al. 2015). Furthermore, when particularly high stator discharge pitch-wise non-uniformity arise, as it happens for very high stator discharge Mach number, increasing inaccuracy can be expected from the adoption of a mixing-plane. In fact, the mixing-plane introduces a punctual mixing-process, leading to an entropy jump at the mixing-plane, that is as big as the pitch-wise non-uniformity (Rubechini, Marconcini, Giovannini, et al. 2015). Case of high pitch-wise non-uniformity can arise either when purely convergent blades are operated at highly supersonic discharge or, in general, when the stator design features a high level of post-expansion (Deich 1956). Therefore, ORC turbines can be very challenging to model, due to the high pitch-wise non-uniformity shown previously.

As a results of particularly high stator discharge Mach numbers and the resulting intense expansion fans/shock system at stator TE, turbines for ORC applications generally exhibit a strong unsteady behaviour. Particularly, for ORC RITs pressure fluctuations amplitude at rotor LE was seen to be as wide as 200% of the average value (Rubechini, Marconcini, Arnone, et al. 2013), as well as high content of harmonics was found for the unsteady blade lift (Marconcini et al. 2012). Nevertheless, for a highly supersonic radial turbine for ORC plants, radial and tangential forces, as well as the moment exerted by the aerodynamic forces on rotor blades, were seen to undergo extremely wide fluctuations (also changing sign), which can clearly be of structural concern (Rinaldi, Pecnik, and Colonna 2016). Additionally, for highly supersonic turbines, unsteady phenomena occur in the rotor passages, such as shock-boundary layer interaction and viscous wakes, leading to unsteady loss generation mechanisms (Otero Rodriguez, Smit, and Pecnik 2021; Rinaldi, Pecnik, and Colonna di Paliano 2015; Rinaldi, Pecnik, and Colonna 2016).

Improving the unsteady interaction can be achieved by redesigning the stator, although care should be taken, since shape-optimization not accounting for flow uniformity has been seen to worsen the downstream uniformity (Anand, Vitale, et al. 2018). Therefore, ad-hoc design strategies are required.

The possibility of attenuating the unsteady interaction via stator redesign has been discussed by Rubechini, Marconcini, Arnone, et al. (2013). However, neither the profiles, nor the design methods are disclosed, so making difficult to draw conclusions. Additionally, the attenuation of the unsteady stator-rotor interaction for a radial outflow turbine was investigated by Persico, Romei, et al. (2018), who obtained a reduction of rotor blade loading fluctuations via isolated stator and rotor optimization, despite not targeting stator downstream uniformity improvements.

Overall, the impact of different levels of stator downstream non-uniformity on the unsteadiness seen by the subsequent rotor row and resulting fluctuations is not yet addressed comprehensively. Furthermore, the results presented in the previous chapter brought up an additional research question, that is whether or not stator efficiency should be chased by all means, at the expense of flow field uniformity, or, more likely, a trade-off should be sought for. Therefore, the purpose of the work presented in this chapter is two-fold: on the one hand, the work aims at assessing the effect of stator downstream uniformity on the fluctuations of power output and force on rotor blade, as well as on average stage efficiency, while, on the other hand, it aims at understanding the relative weight that should be given to the two conflicting optima seen previously.

The work shown in this chapter was presented at the ASME Turbo Expo 2021 (Cappiello and Tuccillo 2021a) and has been published in the *Journal of Turbomachinery* (Cappiello and Tuccillo 2022).

6.2 Methodology

6.2.1 Computational Cases and CFD Setup

To assess the impact of different levels of stator downstream pitch-wise non-uniformity on the unsteady stator-rotor interaction and unsteady loss generation for this class of turbines, two computational test cases have been defined. Particularly, they have been defined such to be paradigmatic of the two conflicting optima arisen in the previous chapter, which are stator efficiency and stator downstream flow field uniformity. To do so, two stators, selected among the vane profiles investigated in the previous chapter, have been matched to the same rotor design. The stators, whose main features are summarized in Tab. 6.1, have been chosen picking the optimal candidates from stator efficiency point of view, case 1, and stator downstream uniformity point of view, case 2. Furthermore, the stators performance indexes are summarized in Fig. 6.1, whereas the detailed analysis of the stator profiles is reported in Section 5.3.4. It is also worth to point out that the approach followed to define the test cases allows to verify the existence of a trade-off between the two conflicting requirements.

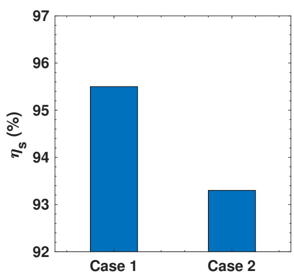

(a) Stator efficiency

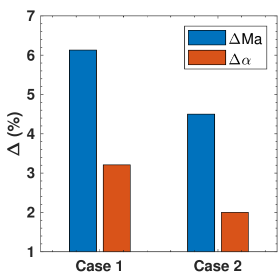

(b) Stator non-uniformity

Figure 6.1: Overview of the performance index of the selected stators

Nonetheless, it is worth recalling that, the stators presented in the previous chapter had all been designed based on the same preliminary design specifications, Section 2.3. Therefore, matching them to the same rotor does not pose any issue.

For what concerns the rotor, its design has been obtained based on the same preliminary design considered for the stators –first test case of Section 2.3– complemented by means of the Aungier's method for the first

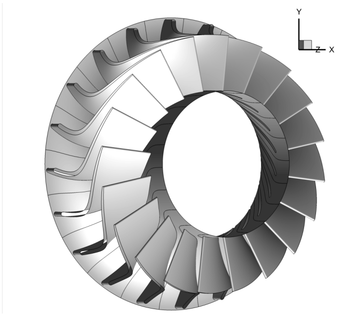

Figure 6.2: Modified rotor geometry

guess geometry generation. However, to reduce the computational cost of the calculations without compromising the accuracy of the results, only one passage was considered for the stator domains, hence exploiting the geometrical periodicity. To insure a pitch ratio at the stator-rotor interface equal to one, the rotor blade count, Z_R, was lowered from the value found during the preliminary design, 22, to 20, which led to the rotor geometry shown in Fig. 6.2, whose geometrical features are summarized in Tab. 6.2. However, in view of the different domain extension of the two stator domains, the approach led to simulate 1 stator passage and 1 rotor passage, in case 1, Fig. 6.3a, while 1 stator passage and 2 rotor passages were modelled in case 2, Fig. 6.3b, as shown in the schematic of the computational domain, reported in Fig. 6.3

The two cases, obtained matching the stators to the same rotor, have been analyzed by means of unsteady RANS calculations, carried out in ANSYS Fluent v17.1. Density based flow solver has been used with implicit formulation and Courant number equal to 5. Roe-FDS scheme has been used for fluxes, while, for the spatial discretization, Least Squares Cell Based has been used for gradients calculations, and second order upwind has been

CASE # (−)	Z_N (−)	$\beta_{\mathrm{met},3}$ (°)	$\mathrm{Re_c} \cdot 10^6$ (−)	$\mathrm{Ma_3}$ (−)	Chord (mm)	R_1 (mm)	R_2 (mm)
1	20	70	4.65	1.69	10.2	24.9	21.7
2	10	80	9.64	1.68	21.1	27.6	21.7

Table 6.1: Characteristic features of the two stators

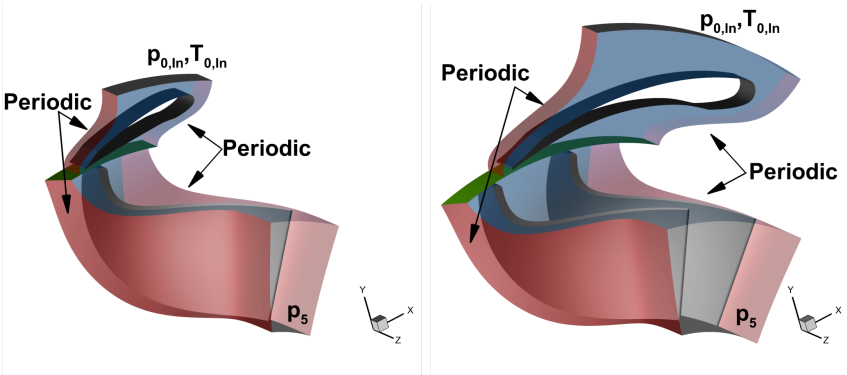

(a) Case 1 (b) Case 2

Figure 6.3: Computational domain schematics

chosen for flow and turbulence. Closure of the turbulence problem has been made by means of the $k-\omega$ SST model, also resorting to wall functions. Solid walls have been set to adiabatic with no-slip conditions. Real gas properties have been described by REFPROP routines (E. W. Lemmon, Huber, and McLinden 2010), that are built-in in ANSYS Fluent. Finally, first order implicit time dependent formulation has been used for time integration, together with sliding mesh approach.

Achieving a sufficient time resolution of the unsteady phenomena is of paramount importance to characterize the stator-rotor interaction and assess the influence of the stator downstream flow field non-uniformity. For this purpose, a sufficiently fine time step must be selected, therefore, subdividing the blade passing period in a sufficient number of time-steps. The blade passing frequency can be computed as in Eqn. 6.1a, in which Ω is the rotational speed in RPM, while the blade passing period can be found as the reciprocal of the blade passing frequency, Eqn. 6.1b. For the present

Z_R $(-)$	β_4 $(°)$	β_5 $(°)$	L_x (mm)	R_4 (mm)	R_5 (mm)	Ω (RPM)
20	24.5	-62.6	12.4	21.3	14.9	92822

Table 6.2: Characteristic features of the rotor geometry

$p_{0,\text{In}}$ (bar)	$T_{0,\text{In}}$ (K)	α_1 (°)	p_5 (bar)	Ω (RPM)
28	439	45	2.16	92822

Table 6.3: Boundary conditions for the uRANS calculations

application the blade passing frequency was found to be $f_{blade} = 30940$ Hz, while the blade passing period $\tau_{blade} = 3.232 \cdot 10^{-5}$ s. An angular step size $\Delta\theta = 0.15°$ was selected, corresponding to a time-step size of $\Delta t = 2.6933 \cdot 10^{-7}$ s, two order of magnitude smaller than blade passing period τ_{blade}.

$$f_{blade} = \frac{\Omega}{60} \cdot Z_R \tag{6.1a}$$

$$\tau_{blade} = \frac{1}{f_{blade}} \tag{6.1b}$$

Being the angular extension swept by a rotor blade within a stator passage equal to 18° in case 1 and to 36° in case 2, the selected time-step size corresponds to 120 steps per period in case 1, while 240 steps are required in case 2.

Furthermore, the selected time-step size also provides a sufficient resolution of wave propagation phenomena. In fact, an approximate calculation of the characteristic time of a right-travelling wave propagating along a mean flow path yields about $5 \cdot 10^{-5}$ s, that is two orders of magnitude larger than the selected time-step size.

Finally, in Tab. 6.3 the boundary conditions adopted for uRANS calculations are summarized.

6.2.2 Mesh Sensitivity

A baseline mesh for stator and rotor passages was built for the geometry of case 1 by means of hexahedral elements in ANSYS TurboGrid, with an average mesh spacing $h = 1.07 \cdot 10^{-4}$. An average $y^+ \approx 25$ was used for the stator domain. Because of the very high flow turning featured by the rotor geometry and, therefore, the high risk of suction side separation, $y^+ \approx 1$ was chosen for this component.

Mesh (−)	Cell Count (−)	h (m)	$\overline{F}_{blade}$ (N)	$\overline{\mathrm{Ma}}_{\mathrm{rel},4}$ (−)	$\overline{P}$ (kW)
Base	$4.45{\cdot}10^5$	$1.07 \cdot 10^{-4}$	69.3	0.651	21.9
Medium	$1.38{\cdot}10^6$	$7.38 \cdot 10^{-5}$	70.1	0.638	17.4
Fine	$3.31{\cdot}10^6$	$5.98 \cdot 10^{-5}$	70.7	0.631	17.2

Table 6.4: Influence of mesh size on the average uRANS results

However, to achieve reliable results a mesh sensitivity analysis was carried out for the flow domains of case 1, that is the most critical from TE expansion fans and shock waves point of view. To this aim, other two meshes were built for this configuration refining the average mesh spacing, which led to the average mesh spacing reported in Tab. 6.4.

Both average values and fluctuations of several quantities were monitored to assess the effect of the mesh size on the results. Particularly, Figs. 6.4a–6.4c shows the effect of the mesh size on the fluctuations of several quantities, for two consecutive periods, computed by means of uRANS calculations, after that time-periodic convergence was achieved for all the three meshes.

As one can notice in Fig. 6.4a and 6.4b, trends and values for both static pressure force on rotor blade and rotor inlet relative Mach number are well captured by all the three meshes considered. Nevertheless, the comparison in Fig. 6.4c unveils that a substantially different instantaneous power output is provided by the base mesh. Conversely, fairly similar instantaneous power output amplitude and waveforms are found by means of the medium and fine meshes. Similar conclusions can be drawn for time-average results reported in Tab. 6.4, where rather similar results can be noticed between medium and fine meshes. Additionally, the slightly lower Mach number at rotor inlet found by the fine mesh can be explained by the improved resolution of the TE shocks achieved by the fine mesh.

6.2.3 Time-step Sensitivity

To further corroborate the choice of the mesh and time-step size selected for the analyses presented in this chapter, it was deemed appropriate to perform a sensitivity analysis to the time-step size. To this end, a further uRANS calculation was carried out for case 1 on the medium mesh, considering a finer time-step size of $\Delta t = 1.7955 \cdot 10^{-7}$ s.

The results are presented in Fig. 6.5, that compares the mass-weighted

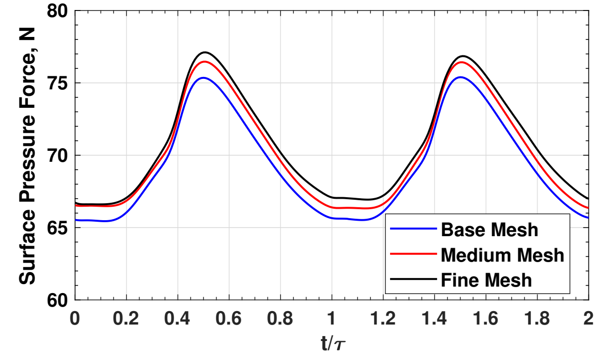

(a) Static pressure force on rotor blade

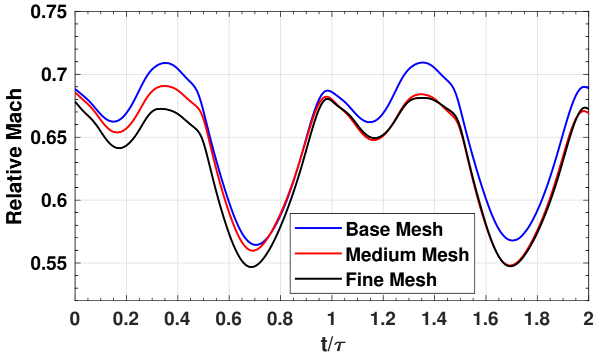

(b) Rotor inlet relative Mach number

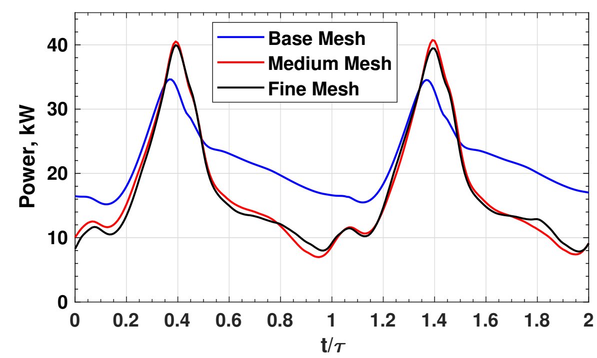

(c) Instantaneous power output

Figure 6.4: Unsteady mesh sensitivity analysis; case 1

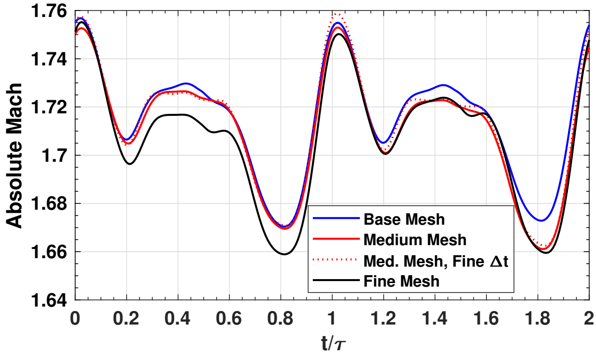

(a) Rotor inlet absolute Mach number

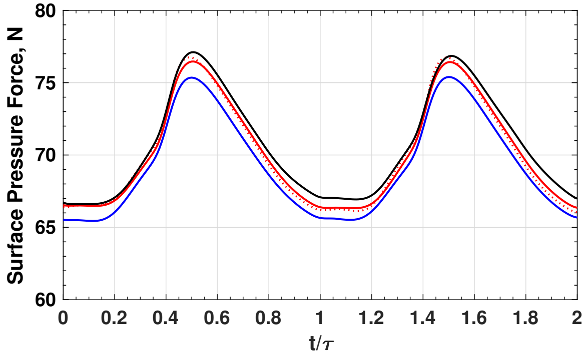

(b) Static pressure force on rotor blade

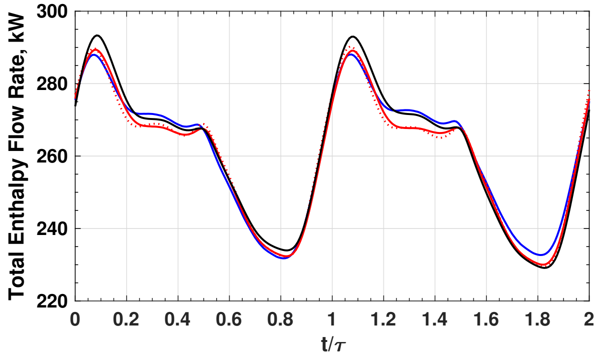

(c) Total enthalpy flow rate at rotor inlet (whole annulus)

Figure 6.5: Unsteady time-step sensitivity analysis; case 1

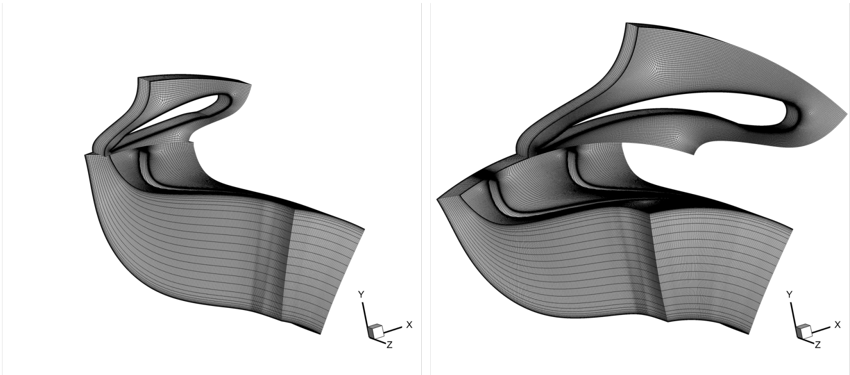

(a) Case 1: 1.38 million elements (b) Case 2: 3.36 million elements

Figure 6.6: Computational meshes for uRANS calculations

absolute Mach number at rotor inlet radius, Fig. 6.5a, pressure force on rotor blade, Fig. 6.5b, and total enthalpy flow rate at rotor inlet (computed for the whole annulus), Fig. 6.5c, obtained for the three meshes and baseline time-step against the results of the medium mesh fine time-step presented with red dotted lines. As one can notice, the results obtained by means of the baseline time-step agree well with those found on the same mesh, but considering a finer time-step size, showing an excellent agreement on both trends and values. This highlights the suitability of the larger time-step size, that does not compromise the accuracy of the results, while relieving the computational cost of the calculations.

In view of the results of the mesh and time-step size sensitivity analyses, it was decided to proceed with a time-step size of $\Delta t = 2.6933 \cdot 10^{-7}$ s and an average mesh spacing corresponding to the medium mesh, namely $h = 7.38 \cdot 10^{-5}$ m, for both case 1 and case 2, resulting in the computational meshes shown in Fig. 6.6 for case 1 and case 2, which have about 1.38 and 3.36 million elements, respectively.

6.3 Results

Unsteady RANS calculations were run for the two configurations described in Sec. 6.2.1, according to the setup presented in the same section. Additionally, in both cases, to ensure that time-periodic convergence was achieved and that, therefore, period-to-period variations are modest, several quantities at mesh interfaces, such as pressure, Mach number, total energy flow rate and mass flow rate, were monitored. In this regard, Fig. 6.7 shows the last 4 periods of case 1 convergence history, as a function of the non-dimensional time-period, together with the last period $\pm 3\%$. As one can notice, rather small period-to-period variations characterize the convergence history, with fairly similar wave forms. Furthermore, all periods presented in Fig. 6.7 are well within the last one $\pm 3\%$. These observations show that time periodic convergence was reached and that the actual time period corresponds to the one associated to the blade passing frequency, Eqn. 6.1a.

The results presented in the following sections are then based on the last two periods of each of the investigated cases. Particularly, in Sec. 6.3.1 the fluctuations of the most relevant quantities with the time period for case 1 and 2 are presented and compared, discussing their implications on the turbine operation; in Sec. 6.3.2 the key features of the unsteady flow field are analyzed and used to explain the trends discussed in Sec. 6.3.1.

6.3.1 Stator-Rotor Interaction and Period Analysis

Absolute and relative mass-weighted Mach numbers at stator outlet and rotor inlet are shown for case 1 and case 2 in Figs. 6.8a–6.8b, as a function of the non-dimensional time period τ. It is also worth to mention that, as a consequence of a different angular extensions of the domains, for case 1 $\tau = \tau_{blade}$, Eqn. 6.1b, while for case 2, $\tau = 2\tau_{blade}$. In these figures large fluctuations of both absolute and relative Mach numbers can be seen as a result of a strong stator-rotor interaction. Furthermore, one peak per period is detected in case 1, while two peaks are seen in case 2, since the latter rotor domain features two rotor blades. Furthermore, in both cases waveforms deviate substantially from a pure sinusoidal shape, arguably as a consequence of the superposition of other phenomena, like the interaction with shock waves and stator wakes.

Interestingly, trends and values found for case 1 and 2 are rather different. Moreover, case 1 features substantially larger fluctuations amplitude, consistently with the larger stator downstream non-uniformity in pitch-wise direction that characterises the first stator, Fig. 6.1.

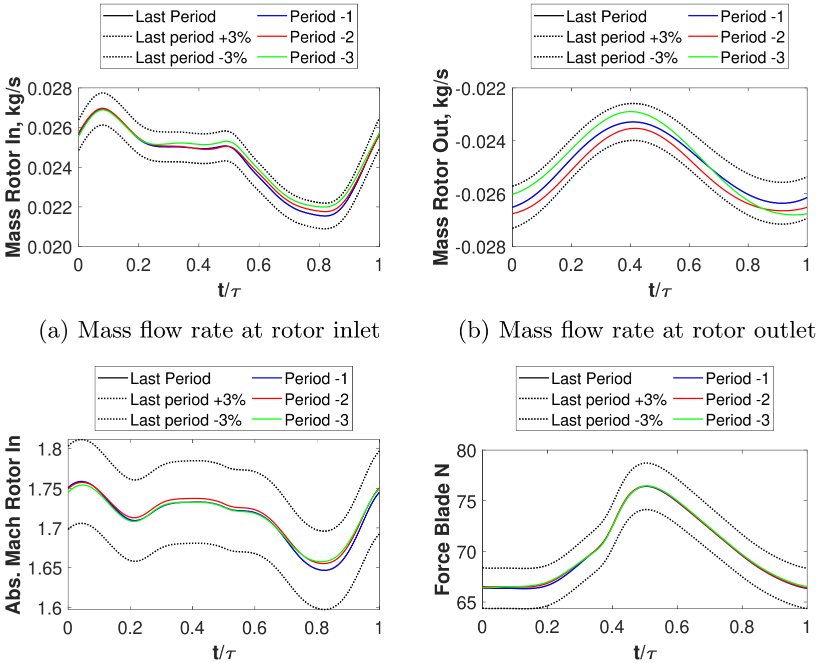

(a) Mass flow rate at rotor inlet

(b) Mass flow rate at rotor outlet

(c) Absolute Mach at rotor inlet

(d) Pressure force on rotor blade

Figure 6.7: Last 4 periods of case 1 convergence history

To compute the instantaneous power output, the unsteady energy balance must be solved. For an adiabatic open control volume –with no chemical reactions–, the latter can be written as in Eqn. 6.2, in which, first and second terms of the Right-Hand Side (RHS) are the inlet and outlet total enthalpy flow rates, while the third term of the RHS is the time derivative of the total energy accumulated within the rotor domain. More specifically, the total energy accumulated within the domain is defined as in Eqn. 6.3. To compute the unsteady energy accumulation and release, the total energy of the rotor domain, Eqn. 6.3, was monitored during the calculations and its time derivative was computed by means of backward finite-difference approach.

Figs. 6.8c–6.8d show the fluctuations three terms of the RHS of Eqn. 6.2 for case 1 and 2, with values computed for the whole annulus.

$$P(t) = \dot{m}_{\mathrm{In}}(t) \cdot h_{0,\mathrm{In}}(t) - \dot{m}_{\mathrm{Out}}(t) \cdot h_{0,\mathrm{Out}}(t) - \frac{dE}{dt}(t) \tag{6.2}$$

$$E = \int_{\mathrm{Domain}} \rho \left(h_0 - \frac{p}{\rho} \right) dV \tag{6.3}$$

Large fluctuations can be noticed in Figs. 6.8c–6.8d, both for case 1 and 2, particularly for total enthalpy flow rate at rotor inlet and time derivative of total energy accumulated in the domain. However, once again the fluctuations are much larger in case 1 than in case 2. Furthermore, a notable matching can be noticed between the total inlet enthalpy flow rate and the time derivative of the total energy. Finally, while the total enthalpy flow rate at rotor outlet exhibits an almost sinusoidal shape, more complicated trends characterize the other two quantities in Figs. 6.8c–6.8d.

Figs. 6.8e–6.8f present for both case 1 and 2 the instantaneous power output computed by means of Eqn. 6.2, together with the last term of Eqn. 6.2, both computed for the whole annulus.

In both cases the fluctuations are large. However, consistently with the other trends seen previously, and with the larger pitch-wise non-uniformity found for the stator of case 1, the fluctuations amplitude is extremely larger in case 1, as also summarized in Tab. 6.5. Particularly, for case 1 the maximum fluctuation amplitude of the instantaneous power output reaches 135% of the mean value, while only 27.5 % is reached in case 2. Nevertheless, the comparison of the average values of power output reported in the same table highlights that case 1, besides showing much larger fluctuation amplitudes, also exhibits a substantially lower average power output. The latter is in fact 17.3 kW against 20.8 kW achieved in case 2. This difference must be clearly related to a substantially different total-to-static efficiency, which is in fact much lower for case 1 than case 2, Tab. 6.5. Therefore, it is interesting to notice that, despite the second configuration features a less efficient stator, Fig. 6.1, the uRANS calculations highlight a substantially higher average stage efficiency for case 2, Tab. 6.5, arguably thanks to the more uniform flow at stator discharge. Ultimately, this finding suggests that the more uniform flow delivered by the second stator provides more favourable conditions for the rotor operation and that, to a certain extent, the stator downstream uniformity might outweigh the stator efficiency.

The power output fluctuations, seen in Figs. 6.8e–6.8f, can be corroborated by the mid-span rotor blade loading shown as a function of the normalized meridional coordinate, for three pitch fractions, in Figs. 6.9a–6.9b, for case 1 and 2, respectively. More specifically, significant variations of the

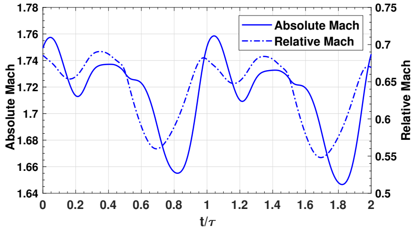

(a) Quantities at rotor inlet. Case 1

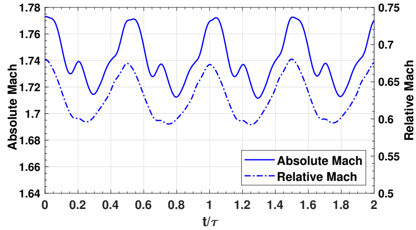

(b) Quantities at rotor inlet. Case 2

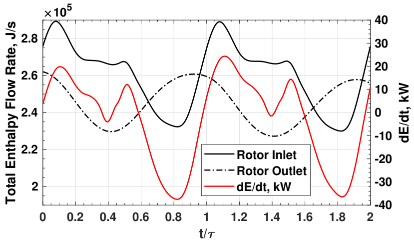

(c) RHS Terms of Eqn. 6.2. Case 1.

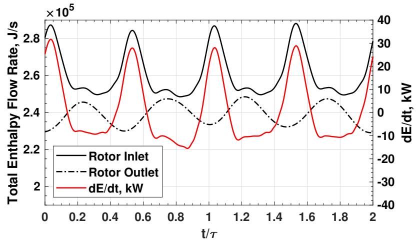

(d) RHS Terms of Eqn. 6.2. Case 2

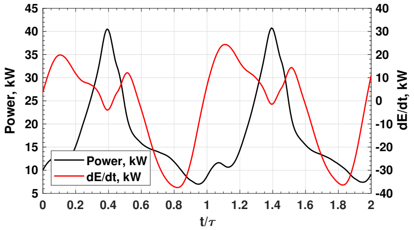

(e) Case 1

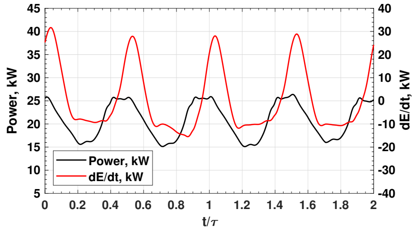

(f) Case 2

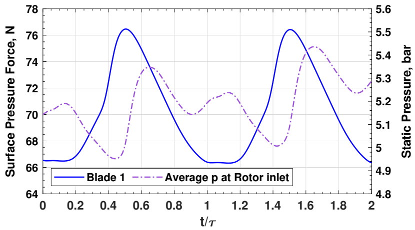

(g) Case 1

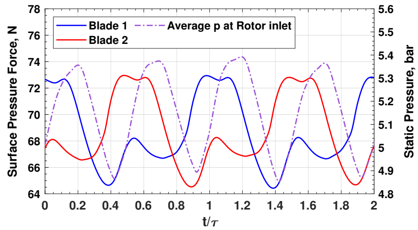

(h) Case 2

Figure 6.8: Time-period fluctuations. Values in Figs. 6.8c–6.8f referred to the whole annulus. Fluctuations of pressure force on rotor blade Figs. 6.8g–6.8h computed by Eqn. 6.4

Case #	$\overline{\eta}_{\mathrm{TS}}$ (%)	$\overline{P}$ (kW)	$\overline{F}$ (N)	$max\lvert\frac{P-\overline{P}}{\overline{P}}\rvert \cdot 100$ (%)	$max\lvert\frac{F-\overline{F}}{\overline{F}}\rvert \cdot 100$ (%)
1	64.7	17.3	70.1	135	9.0
2	77.5	20.8	68.6	27.5	6.2

Table 6.5: Efficiency, power output and pressure force: mean and maximum fluctuation

blade loading distributions can be noticed in the frontal part and particularly at the lowest meridional coordinate values, suggesting a large variability of the incidence occurring during the time period. Furthermore, more regular trends can be seen in case 2. Also, the area bounded by the blade loading in Figs. 6.9a–6.9b changes largely at different fractions of the time period. In turn, this arguably leads to highly variable forces exerted on the rotor blade surface, with possible implications from structural integrity point of view. In this regard, to provide a preliminary assessment of the aerodynamic forces exerted on the blade surface, the overall inviscid contribution was computed by means of Eqn. 6.4 and the results are shown in Figs. 6.8g–6.8h.

$$F(t) = \int_{blade} p(t) \cdot \overrightarrow{n} \cdot dA \tag{6.4}$$

As one can notice, rather different trends are achieved in case 1 and 2, for which two curves are shown in Fig. 6.8h, as its computational domain includes two blades. However, despite the rather different trends, substantially the same average values can be seen in Tab. 6.5, i.e., 70.1 vs 68.6 N.

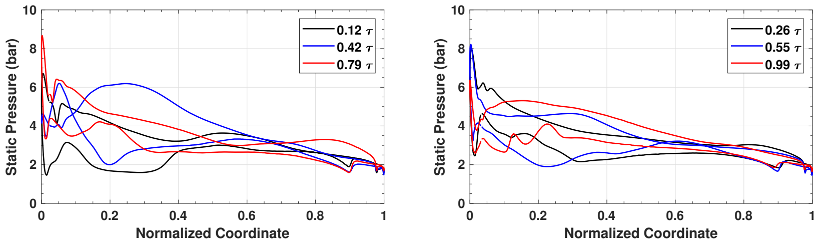

(a) Case 1 (b) Case 2

Figure 6.9: Instantaneous mid-span rotor blade loading

Furthermore, similarly to the other quantities investigated so far, maximum fluctuation amplitude of pressure force on rotor blade is 1.5 times larger for case 1 than case 2, Tab. 6.5.

As a final remark, it is worth to observed that all the investigated quantities, e.g., absolute and relative Mach number, pressure force on rotor blade and power output, showed much larger fluctuations for the first case. This occurrence can arguably be ascribed to the larger downstream non-uniformity in pitch-wise direction featured by the stator of case 1. Also, as will be shown in next section, this circumstance leads the rotor to work under highly variable incidence and, therefore, to fluctuating power output and load on rotor blade.

6.3.2 Unsteady Flow Field Analysis

To identify the reasons of the so different performance seen in the previous section for the two configurations, as well as the large fluctuations, the unsteady flow field was investigated, and the main characteristic features are presented in this section.

The Instantaneous mid-span static pressure contours are presented for case 1 and 2 at three time instants in Fig. 6.10. As one can notice, a relevant stator-rotor interaction is present in both cases, determining from time-step to time-step a highly variable pressure distribution at the stator rotor interface and, particularly, at the rotor LE. The footprint of stator TE shocks can be clearly seen in both cases, with variable strength and orientation during the time-period. The LR branch of the TE shock can be seen to propagate directly in the rotor passages, and to be periodically cut by the rotor LE. However, in case 2 the LR branches appear weaker and oriented more tangentially than in case 1. On the other hand, the RR branches first impinge on the suction side of the adjacent vane and are, in both cases, reflected downstream as LR shocks. Furthermore, the angles of reflection are clearly affected by the rotor position, particularly in case 2, for which the variability is enhanced. These aspects can clearly be noticed in the snapshots of the flow field, for both cases in Fig. 6.10. In fact, for case 1, the reflected RR branch appears to be oriented more radially at $t \approx 0.25\tau$, whereas it is instead more tangential at $t \approx 0.96\tau$, when it impinges on the rotor LE. Likewise, in case 2, the reflected RR branch is more radially oriented at $t \approx 0.17\tau$, with respect to $t \approx 0.38\tau$ and $t \approx 0.99\tau$, at which instants the reflected RR shocks are more tangential and impinge on the LE of two consecutive rotor blades.

Some other peculiar flow patterns can be identified for both case 1 and

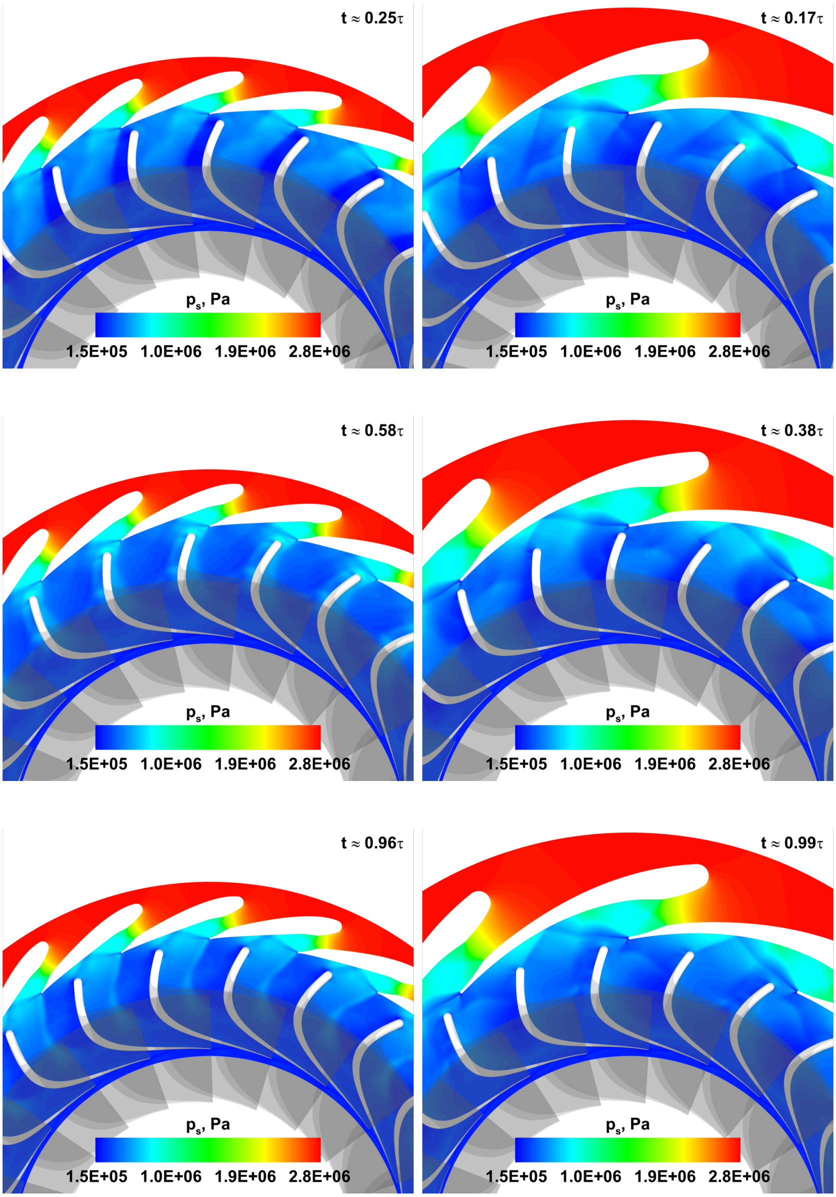

Case 1 Case 2

Figure 6.10: Instantaneous mid-span static pressure contours.

2. Particularly, for the first case at $t \approx 0.58\tau$, a pressure peak can be seen at the rotor LE. Similarly, in case 2, at $t \approx 0.17\tau$, when one of the two rotor blades of the computational domain passes through the set of compression waves (E$'$, Fig. 5.8a), a pressure peak can be detected at the rotor LE. Also, at this instant of time, both LR and reflected RR shocks can be seen to propagate into the rotor passages. Finally, a last peculiar flow structure, that can be detected in case 2 at $t \approx 0.38\tau$ and $t \approx 0.99\tau$, is a pressure wave, originated by a suction side separation (that will be discussed later), that travels upstream as a curved wave front.

Figure 6.11 presents the instantaneous mid-span relative Mach number contours of the rotor domain for case 1 and 2, for which several characteristic features of the flow field can be identified. First of all, in all the time-step presented, an initial over-expansion can be noticed in proximity of the rotor LE, leading to a very high peak of relative Mach number (≈ 1.6). However, the extension of this supersonic pocket is incredibly variable during the rotor period, particularly in case 1. For this case the supersonic pocket is particularly large at $t \approx 0.42\tau$, while only of modest dimension at $t \approx 0.12\tau$ and almost negligible at $t \approx 0.79\tau$. For case 2, with reference to the left hand side blade of the plots, the maximum Mach number peak and pocket size are detected at $t \approx 0.26\tau$ and progressively decrease towards $t \approx 0.55\tau$ and $t \approx 0.99\tau$.

Furthermore, at all the time-step presented, a rather large area of flow recirculation can be identified at the blade suction side as a low Mach region. As will be discussed later in the chapter, this separation is related to high entropy generation. Nevertheless, the size and location of the separation appear to be highly variable during the rotor period, particularly for case 1. In this case the separation size is maximum at $t \approx 0.12\tau$, while it progressively decreases moving to $t \approx 0.42\tau$ and to $t \approx 0.79\tau$.

The reasons behind the remarkable variations of size and location of the recirculation can be unveiled by means of the close-up view of the rotor LE region, shown for case 1 in Fig. 6.12 for three time-steps. As one can see, while the rotor travels through the stator pitch, the location of the stagnation point fluctuates significantly. Particularly, at $t \approx 0.37\tau$, the stagnation point is located at the RHS with respect to the LE center, while, at $t \approx 0.58\tau$, its location appears at the left of the LE, to be back at the right of the LE at $t \approx 1.00\tau$. This mechanism, that can arguably be ascribed to the high pitch-wise non-uniformity that characterizes the stator discharge, leads the rotor to work under highly variable incidence, leading, in turn, to the fluctuations of blade loading seen in the previous section, Figs. 6.9a–6.9b,

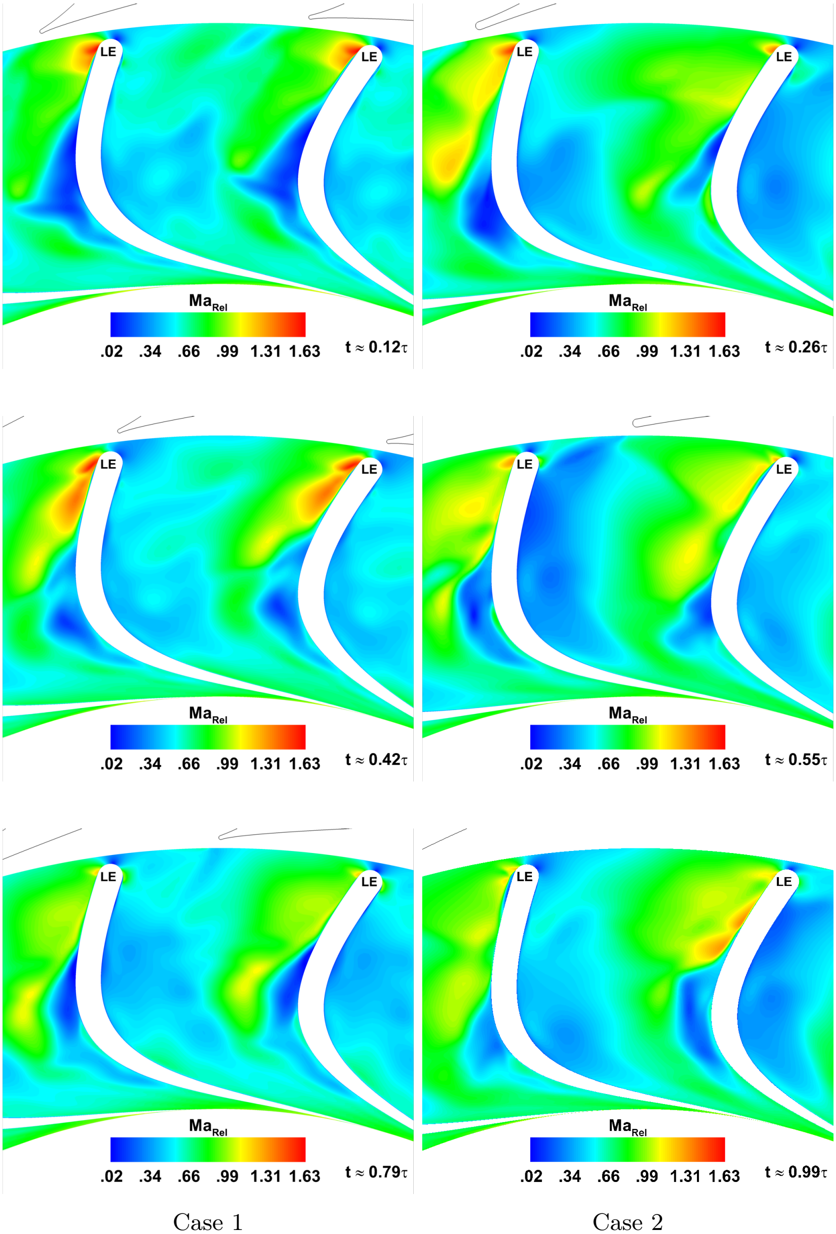

Figure 6.11: Instantaneous mid-span relative Mach number contours.

and of power output, Figs. 6.8e–6.8f. Hence, begin the stator downstream non-uniformity higher for case 1, fluctuations of power output, blade loading and stagnation point location are also larger in this case.

Figure 6.13 presents the instantaneous entropy contour at mid-span for both case 1 and 2, and allows the identification of the main sources of inefficiency. Proceeding in the streamwise direction from stator inlet, similar features of the entropy patterns can be identified in the two cases. The first entropy peak that is encountered is the one attaining to the stator wake. In both cases, this is shed downstream and cut by the rotor LE. Subsequently, the stator wake is ingested into the rotor passages and interact with the second entropy peak located at the suction side of the rotor blade, enlarging it. Particularly, the second entropy peak is related to the suction side separation seen previously, Fig. 6.11, and, therefore, it follows the same dynamic. Consequently, in both cases, the suction side entropy peak shows fluctuations of size and maximum values. However, quite remarkably, its size is generally larger for the first case, as also the maximum entropy values are larger for case 1.

Proceeding further downstream, the last entropy peak met in both cases is due to the rotor wake, that is then shed towards the outlet of the domain.

Particularly, a better visualization of the rotor wake is provided in Fig. 6.14, that shows the close-up view of the rotor TE region for case 1. Interestingly, despite the average relative Mach number at rotor discharge is subsonic, two supersonic regions can be seen in proximity of the rotor TE, where the expansion fans followed by the shocks encompass the whole rotor channel. Furthermore, the RR branch of the rotor TE pattern can be seen to interact with the rotor wake, leading the size of the supersonic regions to fluctuate. Moreover, as a results of the shock-boundary layer interaction, the thickening of suction side boundary layer downstream of the LR shock impingement can be noticed.

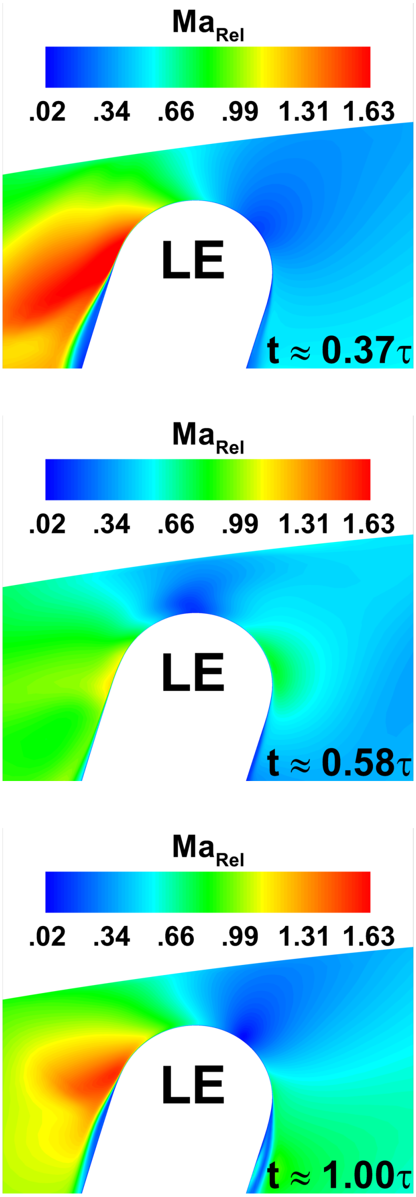

Figure 6.12: Close-up view of the rotor LE region. Case 1

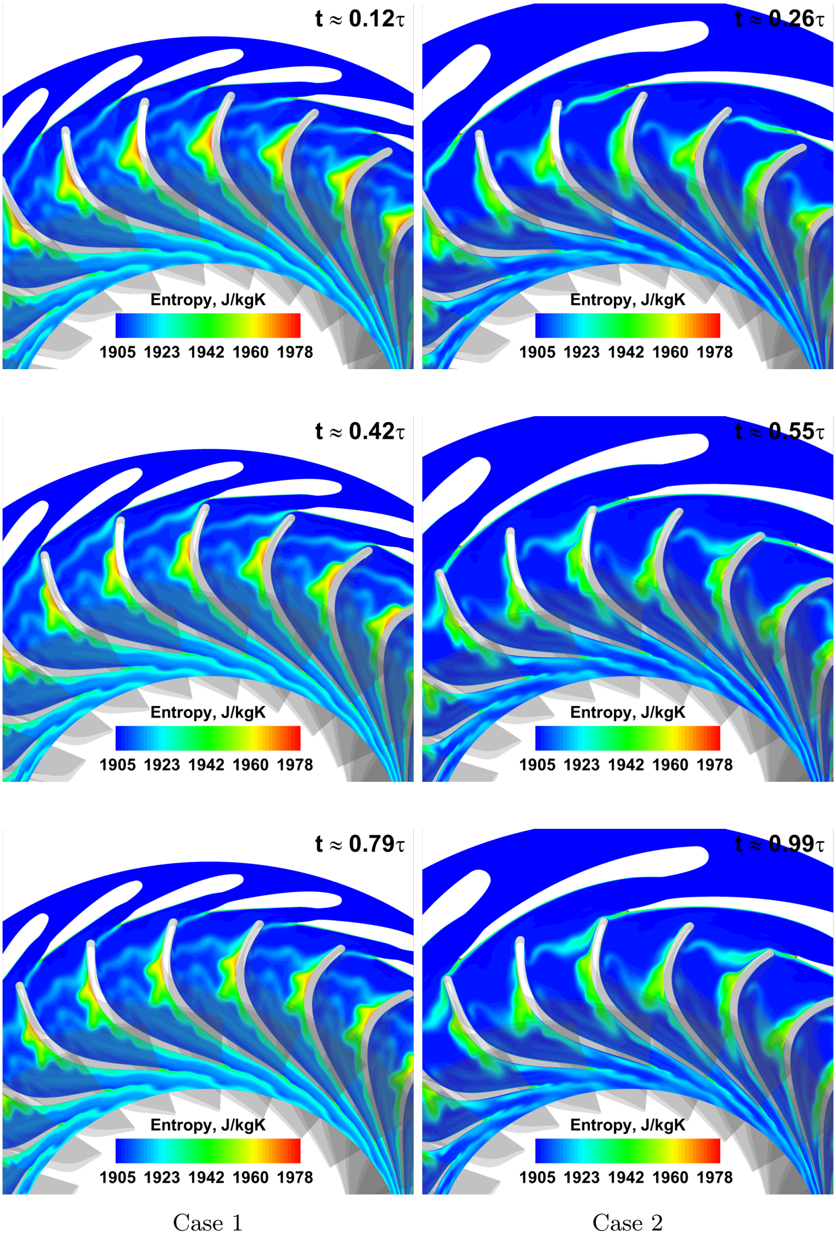

Figure 6.13: Instantaneous mid-span entropy contours.

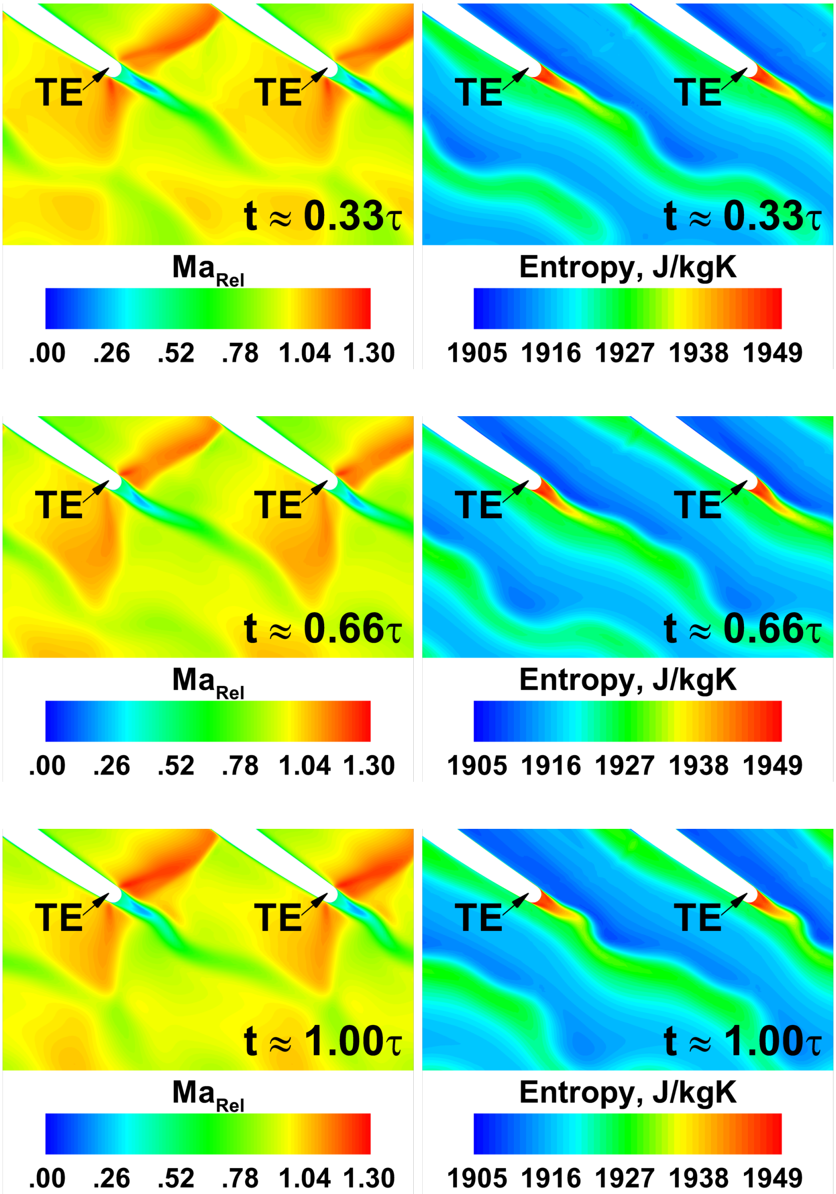

Relative Mach Entropy

Figure 6.14: Close-up view of the TE region. Case 1.

6.4 Concluding Remarks

In the present chapter two RIT stages have been analyzed by means of unsteady RANS calculations. More specifically, the same rotor geometry was matched to two supersonic convergent-divergent stators chosen among those investigated in a previous chapter, selecting the optimal candidates from stator efficiency and stator downstream uniformity points of view. Nevertheless, the stator chosen following the optimal efficiency criterion featured the worse stator downstream uniformity, and vice versa for the other stator.

The uRANS calculations showed that, both in case 1 and 2, large fluctuations of Mach number at stator-rotor interface, power output and pressure force on rotor blade exist during the rotor period. Particularly, this occurrence can arguably be ascribed to the large stator discharge pitch-wise non-uniformity, that characterizes ORC supersonic turbines stators.

Additionally, the fluctuations were seen to be much larger for the stage equipped with the stator that featured larger downstream non-uniformity, leading to dramatically wide power output fluctuations amplitude. Nonetheless, the average power output and stage efficiency resulted to be affected too. In fact, these quantities resulted to be substantially lower for the case featuring larger stator downstream non-uniformity.

The mechanism leading to the large fluctuations of power output was unveiled investigating the unsteady flow field. That is, the large stator downstream non-uniformity leads to rapid fluctuations of the stagnation point location at the rotor LE, which, in turn, leads the rotor to work under highly variable incidence. Therefore, the larger the stator downstream non-uniformity the larger the fluctuations.

Most notably, the configuration characterized by a larger stator downstream uniformity resulted to be the optimal one also from stage efficiency point of, despite the less efficient stator. This ultimately suggests that the stator downstream uniformity –that is a critical aspect for this class of turbines– might, in fact, outweigh the stator efficiency.

Furthermore, the results clearly show that only aiming at stator efficiency during the stator design might lead to highly sub-optimal configurations from stage efficiency point of view, envisaging the need to include the stator downstream uniformity among the design targets and/or moving towards multi-row optimization techniques.

It is also worth to observe that the work presented in this chapter provided novel contributions to the field of supersonic RITs for ORC plants, assessing the effect of different levels of stator downstream non-uniformity on the unsteady stator-rotor interaction, rotor operation and stage efficiency, which was a rather unexplored topic.

Finally, the analysis of the unsteady stator-rotor interaction for a turbine stage equipped with a shape-optimized stator (accounting for both stator efficiency and stator downstream uniformity) is advisable as future development.

CHAPTER 7

Stator-Rotor Radial Gap

7.1 Introduction

An often neglected aspect of Radial Inflow Turbine design is the stator-rotor radial gap. However, this might play a role in the reduction of viscous loss production, flow field uniformity at rotor inlet and aero-mechanical interactions between the two consecutive rows. Also, when laboratory experiments are concerned, larger radial gap sizes provide more space for instrumentation, e.g., for the characterization of the flow at stator discharge in pitch-wise direction.

Nonetheless, only few studies have addressed the stator-rotor radial gap impact on RITs performance. Among the first to investigate the topic, Tunakov (1961) proposed an empirical rule to determine the optimal radial gap size as a function of vane height and outlet flow angle. Therefore, the optimal radial gap size is meant to be the compromise between poor flow uniformity that may arise as a result of a too small radial gap and excessive friction loss that may arise in the opposite scenario.

Later on, Watanabe, Ariga, and Mashimo (1971) performed experiments on a set of vanes and found that the radial gap had small impact on efficiency. More recently, Khalil, Tabakoff, and Hamed (1976) investigated the impact of stator-rotor radial gap from subsonic to transonic regime and found that losses were only slightly affected by the radial gap size. More recently, Simpson, Spence, and Watterson (2013) investigated the effect of stator-rotor radial gap both numerically and experimentally and found only slight efficiency decrease due to the effect of the radial gap.

Nevertheless, it is worth recalling that the operative conditions featured by single stage RITs for high temperature ORC plants are substantially different from those of conventional applications. In fact, RITs for high temperature ORC plants usually expand fluids made up of complex molecules, potentially entailing non-ideal effects (Colonna and Guardone 2006), according to the value of the fundamental derivative of gasdynamics (Thompson 1971). The latter is also known to affect turbine performance (Baumgärtner, Otter, and A. P. S. Wheeler 2020; Giuffre' and Pini 2020), as well as TE expansion fan/shock system (Baumgärtner, Otter, and A. P. S. Wheeler 2021b; F. D. Galiana et al. 2017; F. J. D. Galiana, A. P. Wheeler, and Ong 2016). Also, single stage RITs for high temperature ORC plants usually features high stator discharge Mach number (Anand, Vitale, et al. 2018; A. P. S. Wheeler and Ong 2013), generally accompanied by large stator downstream uniformity (Anand, Vitale, et al. 2018; Pasquale, Ghidoni, and Rebay 2013; Pini, Persico, Pasquale, et al. 2014), that can be a relevant issue for this class of turbines, determining wide fluctuations of aerodynamic forces on rotor blade (Rinaldi, Pecnik, and Colonna 2016). Finally, it is worth to observe that, if the vane height is constant, the radial gap can be considered an area-decreasing channel.

In view of these very unconventional flow conditions, the stator-rotor radial gap of this class of turbines requires in-depth investigations, with particular focus on the flow field behavior. Hence the purpose of the work presented in this chapter is to gain further insight into the flow physics occurring in the stator-rotor radial gap of supersonic RITs for high temperature ORC plants. To do so, several stator geometries of increasing outlet radius have been designed –by means of an open source code– and tested by means of 3D RANS calculations. This activity has been carried out during a visiting stay of four months at the Delft University of Technology in the Propulsion and Power group.

The work shown in this chapter is part of a work accepted for publication at the ASME Turbo Expo 2022 (Cappiello, Majer, et al. 2022).

7.2 Methodology

The convergent-divergent RIT stator geometries investigated in the present section have been designed by means of the open-source code developed at TU Delft, known as *openMOC* (Anand, Colonna, and Pini 2020; Anand, Vitale, et al. 2018). The code is implemented in Python and is based on the well-known MoC, adapted to dense gases, also encompassing different methods for fluid properties description, e.g., various thermodynamic libraries and LuT approach.

Differently, from the MoC presented in Section 4.2, that allows to size the divergent section of a sharp-edged MLN, of which an example is provided in Fig. 4.1a, the openMOC code sizes the divergent portion of a *smoothly contoured* nozzle, Fig. 4.1b.

To be able to vary the outlet radius of the row independently of the mass flow rate delivered by the nozzle, a mass flow rate-based scaling of the divergent section was introduced in the code. However, as a consequence of this change, several modifications have been required, namely, for the way the divergent section is arranged in the nozzle, as well as the rear suction side generation.

The openMOC sizes the non-dimensional divergent section to expand a given working fluid from upstream total conditions, p_0 and T_0, to a target Mach number, $\mathrm{Ma}_{\mathrm{tg}}$, by means of the MoC. Similarly to the vane parametrization presented in Section 5.2.1, the divergent section is scaled to deliver the design mass flow rate, $\dot{m}$, according to Eqn. 7.1, in which Z_N is the vane count, ρ_{th} and a_{th} are density and speed of sound in the throat, respectively, and b is the vane height. Later, several geometrical operations are performed to place the divergent section in the correct position and build a closed vane profile around the divergent section, in a similar way to the steps presented in Section 5.2.1.

$$A_{\mathrm{th}} = \frac{\dot{m}}{Z_N \cdot \rho_{\mathrm{th}} \cdot a_{\mathrm{th}} \cdot b} \tag{7.1}$$

Differently from the vane parametrization adopted in Section 5.2.1, the subsonic portions of vane pressure and suction sides are built by means of single NURBS curve (Piegl and Tiller 1997), insuring tangency at the junction with the supersonic parts obtained by means of the MoC. Likewise, the uncovered suction side is built by means of a second NURBS curve.

The geometries investigated in the present chapter are designed to fit the ORCHID turbine (C. M. De Servi et al. 2019), that features an expansion ratio of about 41, maximum Mach number of approximately 2 and power

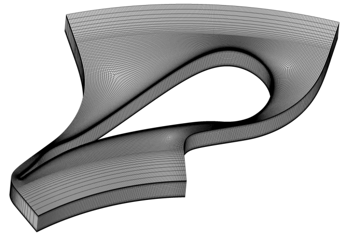

Figure 7.1: Computational mesh of the baseline stator geometry

output of 10 kW. Therefore, considered the similarity between the working conditions, e.g., Re, Ma and working fluid, of the profiles investigated in the present chapter to that investigated by C. M. De Servi et al. (2019), all computational meshes used in the present section have been built so as to provide the same average mesh spacing h, Eqn. 2.50, adopted by C. M. De Servi et al. (2019), that was already proven to be sufficiently refined. Thus, computational meshes have been built in ANSYS TurboGrid by means of hexahedral cells of average $h = 4.83 \cdot 10^{-5}$ m, ensuring $y^+_{\text{blade}} = 1$ and $y^+_{\text{Endwalls}} = 5$. Additionally, the computational domains have been enlarged downstream, placing the outlet surface of the stator meshes at ≈ 23 mm (while the radius at which the stator-rotor interface would lay is ≈ 26 mm), avoiding to force non-physical solutions. This led to the baseline mesh, shown in Fig. 7.1, made up of about $3.2 \cdot 10^6$ elements. In view of the increasing domain size that occurs as the radial gap increases, meshes for the other geometries investigated in the present chapter are characterized by larger cell counts, up to $4.22 \cdot 10^6$ elements for the biggest radial gap investigated.

To investigate the effect of the stator-rotor radial gap size, 3D steady-state calculations with RANS approach have been carried out for the stator domains. The calculations have been performed in ANSYS CFX v19, adopting second order numerical scheme for the advection terms, while high resolution was adopted for turbulence. The turbulence problem closure was achieved by means of $k - \omega$ SST turbulence model and the fluid properties have been described by LuT approach with table size 1000x1000. Finally, residual values of 10^{-7} was used as convergence criterion.

Solid walls have been treated as adiabatic with no-slip condition. Fluid boundary conditions have been provided by means of upstream total pressure $p_{0,\mathrm{In}}$ and temperature $T_{0,\mathrm{In}}$, while static pressure was provided for the outlet boundary. Starting from the baseline case, i.e., the smallest radial gap investigated, the outlet static pressure value was selected such to achieve a static pressure at the stator-rotor interface radius as close as possible to the value found in stage calculations. This resulted in an expansion ratio $\Pi \approx 26$. Subsequently, the expansion ratio of the other geometries was set accordingly. Finally, the CFD boundary conditions are summarized in Tab. 7.1.

Fluid	$p_{0,\mathrm{In}}$	$T_{0,\mathrm{In}}$	Π
-	(bar)	(K)	-
MM	18.1	573	26.3

Table 7.1: CFD boundary conditions

Case	Z_N	$\beta_{m,3}$	Ma_{tg}	$\frac{\text{width}_{TE}}{\text{pitch}}$	$\frac{R_3}{R_4}$	ΔR	N	Re_c
-	-	(°)	-	-	-	(mm)	-	-
Original *	12	80	2	0.0054	1.037	0.96	1.51	$4.00 \cdot 10^6$
Baseline	12	80	1.91	0.0143	1.037	0.96	1.57	$4.14 \cdot 10^6$
ΔR_1	12	80	1.91	0.0143	1.043	1.10	1.56	$4.16 \cdot 10^6$
ΔR_2	12	80	1.91	0.0143	1.058	1.50	1.56	$4.20 \cdot 10^6$
ΔR_3	12	80	1.91	0.0143	1.074	1.90	1.56	$4.26 \cdot 10^6$
ΔR_4	12	80	1.91	0.0143	1.153	3.93	1.54	$4.51 \cdot 10^6$
ΔR_5	12	80	1.91	0.0143	1.250	5.94	1.51	$4.82 \cdot 10^6$

Table 7.2: Stator design variables. (*) by C. M. De Servi et al. (2019)

7.3 Results

To assess the effect of the stator-rotor radial gap, six stator geometries have been designed by means of the method described in Section 7.2.

First of all, the stator configuration presented by C. M. De Servi et al. (2019) was redesigned, so as to respect the manufacturing constraints provided by TU Delft's in-house workshop, which led to increase the TE thickness from less than 0.1 mm to 0.2 mm. This redesigned geometry will be from here on referred to as *baseline*.

Subsequently, other 5 geometries of increasing radial gap size, $\Delta R = R_{\text{stator,TE}} - R_{\text{rotor,LE}}$, have been designed keeping all the other design variables, such as target Mach number for the MoC, outlet metal angle and vane count, fixed, according to values reported in the Tab. 7.2. The resulting six geometries from baseline to ΔR_5 are shown in Fig. 7.2, together with the rotor inlet radius.

It is worth to notice that the baseline geometry exhibit a much larger stator TE thickness-to-pitch ratio, $\frac{\text{width}_{TE}}{\text{pitch}}$, than the original geometry. As a matter of fact, while the stator pitch remained unchanged, the stator trailing edge thickness was more than doubled with respect to the original design.

For what concerns the other geometries, i.e., from ΔR_1 to ΔR_5, to compensate for the increasing pitch values due to the increasing outlet radius, the stator TE thickness was adapted case-by-case, so as to insure the same values of $\frac{\text{width}_{TE}}{\text{pitch}}$ for all the investigated cases. This arguably allows not to introduce a bias in the results due to different TE blockages and hence TE loss, therefore, isolating the effect of the stator-rotor radial gap.

Finally, it is also worth observing that the solidity change remained for

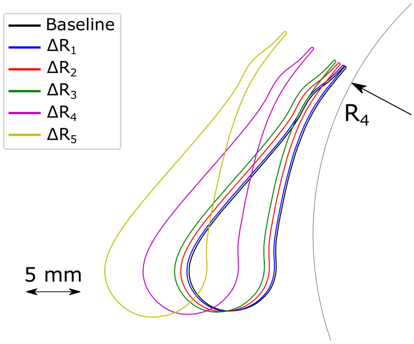

Figure 7.2: Stator geometries

all the cases within 1.5 %.

The resulting geometries have been analysed by means of 3D steady-state RANS calculations, as described in Section 7.2, and the effect of the radial gap size are presented in Fig. 7.3a and 7.3b: the former shows the expansion ratios, Π, achieved up to the stator TE, $p_{0,1}/p_3$, together with the one achieved in the radial gap, p_3/p_4; the latter shows the stator efficiency, η_{N}, evaluated both taking as outlet section the stator outlet radius, R_3 (i.e., the radius to which the stator TE is tangent), Eqn 7.2a, and the radius where the stator-rotor interface would lay, R_4, Eqn 7.2b.

$$\eta_{N,\,3} = \frac{h_{0,\,\mathrm{In}} - h_3}{h_{0,\,\mathrm{In}} - h_{3,\,\mathrm{ise}}} \cdot 100 \tag{7.2a}$$

$$\eta_{N,\,4} = \frac{h_{0,\,\mathrm{In}} - h_4}{h_{0,\,\mathrm{In}} - h_{4,\,\mathrm{ise}}} \cdot 100 \tag{7.2b}$$

Fig. 7.3a clearly shows that a radial gap size change entails a redistribution of the expansion ratio share between radial gap and stator, namely, vaneless and vaned portion of the stationary component, as the expansion ratio achieved at the stator TE progressively diminishes as the radial gap increases. Conversely, the expansion ratio achieved in the radial gap increases if the radial gap size is increased. Nevertheless, the change in expansion ratio share is accompanied by a relevant performance deterioration, that worsen monotonically for increasing ΔR, Fig. 7.3b. Particularly, a relevant loss contribution occurs in the radial gap, in fact, the efficiency decrement is much larger if the efficiency is evaluated including the radial gap, green curve in Fig. 7.3b.

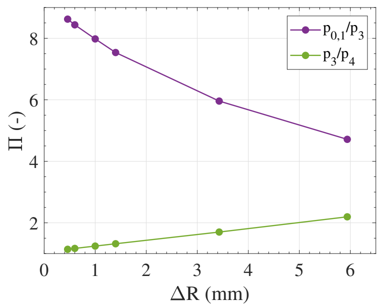

(a) Total-to-static expansion ratio

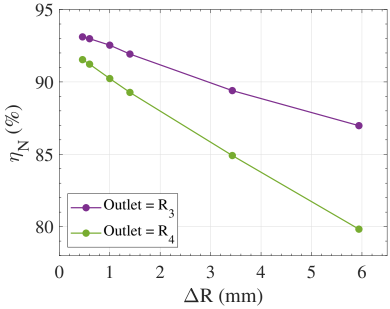

(b) Stator efficiency

Figure 7.3: Effect of radial gap size on stator performance

To unveil the mechanisms leading to these trends the flow field of each configuration must be thoroughly investigated. For this reason, mid-span Mach number and pressure gradient contours are presented in Fig. 7.4 and 7.6.

In the Mach number contours, Fig. 7.4, all peculiar features of convergent-divergent RIT stators can be recognized, e.g., the double expansion fan in the inner throat region and, further downstream, the typical TE expansion fan/shock system can be seen. Interestingly, a rather different TE wake dynamic appears from case to case. In fact, as the radial gap increases the wake travels longer in the domain, while at low radial gap size, the wake exits from the domain sooner. Also, for larger radial gap sizes, the mixing process of the wake seems slower. As a matter of fact, for lower radial gap sizes, the mixing process appears already at an enhanced stage after that the wake has crossed the reflected RR shock. Conversely, at larger gap sizes the wakes are well defined for a longer path, and several wakes crossing the TE shocks can be noticed. Thus, at larger gap sizes, larger number of wakes are seen to cross the domain. As a consequence, the pitch-wise distributions are inevitably affected by a radial gap size change. In this regard, Fig. 7.5 presents the entropy pitchwise distributions –together with their averaged values with dash-dotted lines– for the baseline, ΔR_3 and ΔR_5 cases. As one can notice, in the baseline case the wake footprint is clearly visible as an entropy peak between pitch fraction 0.15 and 0.4. As the radial gap increases, e.g., in the ΔR_3 case, the wake footprint becomes wider and the peak value decreases. Finally, in the ΔR_5 case the profile of the wake is rather difficult to identify.

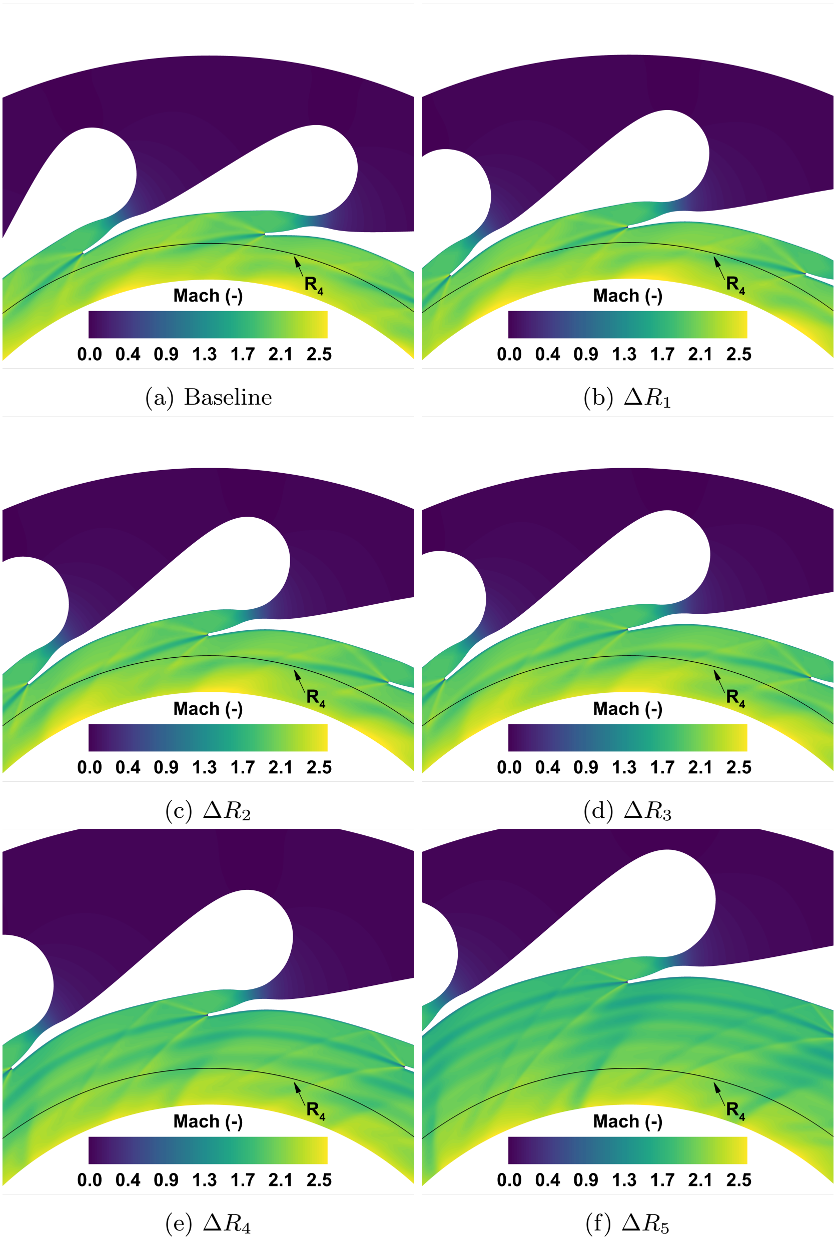

(a) Baseline (b) ΔR_1

(c) ΔR_2 (d) ΔR_3

(e) ΔR_4 (f) ΔR_5

Figure 7.4: Mid-span Mach number contour

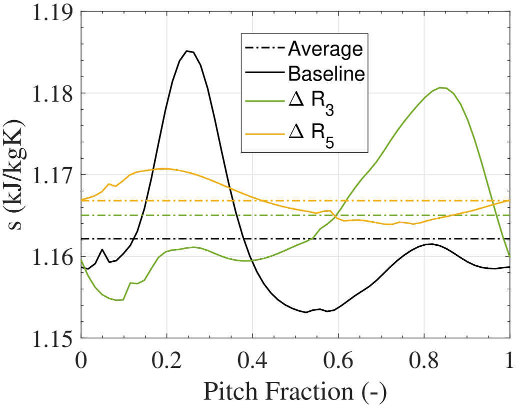

Figure 7.5: Entropy pitchwise distributions and average values at R_4 for Baseline, ΔR_3 and ΔR_5

These observations are consistent with the typical wake dynamics, that, for increasing distances downstream of the TE, leads the wake profile to widen and the average entropy level to increase while the mixing process advances. As the radial gap increases, the distance covered by the flow between stator TE and R_4 indeed increases, leading the mixing reached at R_4 to a more advanced stage, which is witnessed by the higher average entropy values seen for larger gaps at R_4 in Fig. 7.5.

Finally, the entropy rise related to stator TE shocks is visible as small cusps.

The pressure gradient contours presented in Fig. 7.6 show that significant changes of the TE expansion fan/shock system occur as the radial gap increases, appearing as the mechanisms that allows to achieve the expansion ratio redistribution seen previously in Fig. 7.3a.

Notably, for increasing values of the radial gap size, the angular extension of the RR expansion fan **A** in Fig. 7.6 reduces, thus, reducing the post expansion of the row and the expansion ratio achieved up to the TE radius. Furthermore, the RR shock **B** moves upstream and is also strengthened.

This dynamic is also witnessed by a visible blade loading change occurring in the rear part of the vane suction side, where the expansion fan and shock from the adjacent vane TE impinge, slightly after streamwise coordinate 0.8, Fig. 7.7. As a matter of fact, at this location the pressure decrease –due to the expansion fan impinging on the blade suction side– reduces as

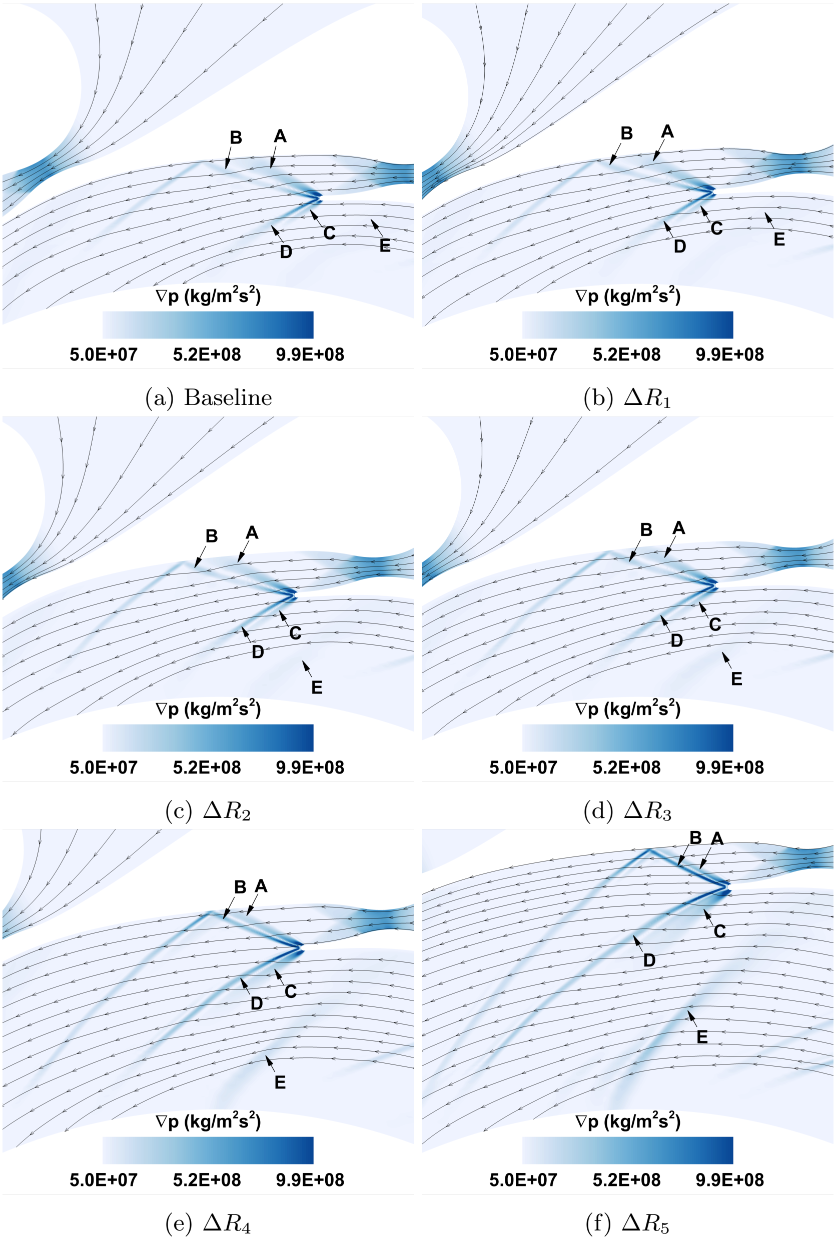

(a) Baseline (b) ΔR_1

(c) ΔR_2 (d) ΔR_3

(e) ΔR_4 (f) ΔR_5

Figure 7.6: Close-up view of mid-span pressure gradient contour

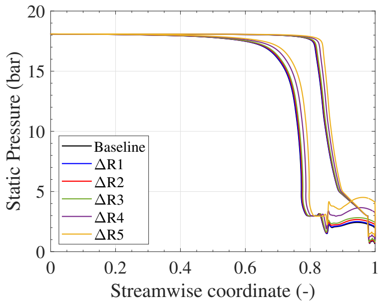

Figure 7.7: Stator loading vs non-dimensional streamwise coordinate

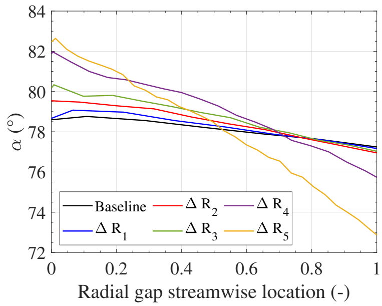

Figure 7.8: Absolute flow angle evolution in the radial gap

the radial gap size increases, whereas the subsequent recompression –due to the impinging shock– strengthens dramatically as the radial gap increases. The latter occurrence has also the effect of unloading the rear suction side.

Thus, the loss increase that occur upstream of the TE radius, R_3, for increasing values of the radial gap, Fig. 7.3b, is arguably due to both shock loss increase and stronger shock-boundary layer interaction for the shock impingement.

Interestingly, because of different shock intensity and orientation, at larger radial gap sizes the streamlines passing through the RR shock are rotated clockwise much more than in cases at low radial gap size.

With respect to the LR branch of the expansion fan/shock system, an opposite dynamic to the one of the RR branch can be noticed. When the radial gap size increases, the LR expansion fan **C** is forced to widen to both match the imposed expansion ratio (compensating the expansion ratio reduction occurred in the bladed region) and the direction of the streamlines coming from the other side of the TE, that is the bladed region. Therefore, this leads to increase the expansion ratio in the radial gap.

It is also interesting to notice that the TE expansion fan/shock system assumes an intermediate configuration for ΔR_4, with both LR and RR TE expansion fans having approximately the same angular extension. Concerning the LR shock **D**, its intensity appears strengthened for increasing sizes of the radial gap.

Another noticeable effect is that, at low radial gap sizes, the LR and the reflected RR shocks travels further apart from each other, while, at larger gap sizes, the two shocks travels much more toward each other. Finally, the radial gap size change also affects the set of compression waves **E** that arises from the curved rear suction side design. While they are hard to distinguish at low ΔR, at larger values they coalesce into a shock further downstream.

Therefore, the overall loss increase occurring in the radial gap when its size is increased can be ascribed to several features, such as the larger number of wakes mixing out in the radial gap and larger wetted area.

Figure 7.8 presents the absolute flow angle (measured from radial direction) evolution within the radial gap as a function of the non-dimensional streamwise location. It is worth mentioning that streamwise location 0 corresponds to the stator TE location, i.e., R_3, whereas streamwise location 1 corresponds to the rotor LE radius, i.e., R_4. Moderate flow angle deflections occur from inlet to outlet of the gap at low radial gap sizes, e.g., $\approx 1.5°$ for baseline and ΔR_1 cases, whereas higher flow angle deflections are achieved as the radial gap size increases, reaching about $9.5°$ for the ΔR_5 case. As one can notice in Fig. 7.8, the larger the radial gap size, the larger the values of the flow angle at the stator TE, i.e., at streamwise location 0, meaning that the flow at the stator TE surface becomes more and more tangential as the radial gap size grows. However, being the outlet metal angle of the vanes constant from case to case, different values of the stator outlet flow angle entail different values of the deviation angle. To explain this finding one should consider the TE flow patter change that occurs as the radial gap size is changed, Figs. 7.6a–7.6f. As a matter of fact, the RR expansion fan **A** turns the flow counter-clockwise, that is, more radially; on the other hand, the RR shock **B** turns the flow clockwise, that is, more tangentially. When the radial gap size is increased, the RR expansion fan **A** becomes smaller, attenuating the counter-clockwise turning, and the RR shock **B** intensifies, strengthening the clockwise turning, hence resulting in a more tangential flow at stator TE, R_3. Ultimately, the deviation angle change mitigates the flow angle differences at the rotor LE.

The significant change of the TE flow structure that occurs as the radial gap size changes also impacts the non-uniformity level of the pitchwise

Table 7.3: Pitchwise non-uniformity levels at rotor inlet

	Baseline	ΔR_1	ΔR_2	ΔR_3	ΔR_4	ΔR_5
$\Delta \mathrm{Ma}_4$	5.40	4.94	2.33	3.78	4.42	4.03
$\Delta\alpha_4$	3.92	3.78	3.33	3.08	2.95	2.99
$\Delta\beta_4$	36.17	33.92	17.78	26.10	31.37	37.76

distributions found at the rotor inlet radius R_4. To provide a quantitative assessment of this aspect, the figure of merit introduced in Sec. 5.3.3 was employed for the Mach number, Ma_4, absolute flow angle, α_4, and relative flow angle, β_4, distributions. The values of the non-uniformity indexes, computed by means of Eqns. 7.3 and reported in Tab. 7.3, show a non-monotone trend as a function of the radial gap size.

$$\Delta \mathrm{Ma}_4 = \frac{\int_0^{\theta_\mathrm{pitch}} |\mathrm{Ma}_4 - \overline{\mathrm{Ma}_4}|\, d\theta}{\Delta\theta_\mathrm{pitch}} \cdot \frac{100}{\overline{\overline{\mathrm{Ma}_4}}} \tag{7.3a}$$

$$\Delta \alpha_4 = \frac{\int_0^{\theta_\mathrm{pitch}} |\alpha_4 - \overline{\alpha_4}|\, d\theta}{\Delta\theta_\mathrm{pitch}} \cdot \frac{100}{\overline{\overline{\alpha_4}}} \tag{7.3b}$$

$$\Delta \beta_4 = \frac{\int_0^{\theta_\mathrm{pitch}} |\beta_4 - \overline{\beta_4}|\, d\theta}{\Delta\theta_\mathrm{pitch}} \cdot \frac{100}{\overline{\overline{\beta_4}}} \tag{7.3c}$$

The most relevant of the non-uniformity indexes considered is the $\Delta\beta_4$, Eqn. 7.3c, since it is directly related to the incidence variability at rotor inlet. Therefore, in view of the results shown in Tab. 7.3, large incidence fluctuations can be expected. Nevertheless, the radial gap size appears as a design variable that can play a role to alleviate the pitchwise non-uniformity.

7.4 Concluding Remarks

In the present chapter the effect of stator-rotor radial gap size on supersonic mini ORC RIT stator performance and flow filed was investigated designing six convergent-divergent stators, which differed by the stator outlet radius. The stators have been designed by means of the open-source code –developed at TU Delft– called *openMOC*, that was modified to carry out the present task. These stator profiles, designed to fit the ORCHID turbine, have been later analyzed by means of 3D CFD calculations.

The results show that, as the radial gap increases, a redistribution of the overall expansion ratio between vaned and vaneless region occurs, leading the latter to increase. This occurrence is accompanied by a non-negligible performance deterioration of the stationary component, which becomes much larger if the radial gap exit is taken as outlet section for the efficiency evaluation.

The investigation of the flow field allowed to gain insight into the mechanism driving the expansion ratio redistribution, which revealed to be related to a substantial change of the stator Trailing Edge expansion fan/shock system. When the radial gap size is increased, on the one hand, this leads the RR branch of TE expansion fan to shrink, reducing the expansion ratio achieved upstream of the TE. On the other hand, the LR branch enlarges, increasing the expansion ratio share of the radial gap. Additionally, the TE expansion fans change is also followed by a relevant change of the TE shocks structure.

Nonetheless, the impact of the TE expansion fans/shocks system on loss was also discussed, with particular focus on the interaction with the suction side boundary layer and the effects on the blade loading. Also, depending on the radial gap size, the stator wake mixing process was seen to follow a rather different dynamics.

Finally, results suggest that, when the radial gap size is increased, a reduction of the target Mach number for the Method of Characteristics might be beneficial to alleviate the loss increase observed in the present analysis. In this circumstance, reducing the target Mach number for the MoC might also compensate the further expansion occurring in the radial gap. Nonetheless, the extension of the investigated design space, so as to include the target Mach number, is recommended.

CHAPTER 8

Conclusions

In the present thesis, several knowledge gaps concerning the design of single stage Radial-Inflow Turbines (RITs) for Organic Rankine Cycle (ORC) applications in the tens of kW scale have been addressed. Particularly, several aspects have been investigated, ranging from design methods, namely, preliminary design and first guess geometry generation codes, to the CFD analysis of various stator designs, as well as unsteady stator-rotor interaction.

First of all, a meanline design code for single stage RITs design was developed. The code is implemented in MATLAB and is suited to both ideal gas and dense vapour applications, via link to thermodynamic library for fluid properties evaluation. The code was used to investigate the RIT design space for several test cases, encompassing different fluids (i.e., a refrigerant and a siloxane) and various expansion ratios (up to a volumetric expansion ratio about 21) and the optimal design requirements were discussed, enriching the extremely limited information available in published literature for these expansion ratio levels. The maximum blade peripheral speed was seen to attain values well within the safe region, while the optimum design was seen to require generally high flow turning from inlet to outlet of the rotor, therefore, it is recommended to verify its feasibility on a case-by-case basis. High η_{TS} and η_{TT} were found to be possible, despite the high expansion ratio, attaining to medium-low degree of reaction values. As a consequence, though, the optimal design entails highly supersonic stator discharge conditions. Conversely, there exist many solutions that allow achieving subsonic flow in the relative frame at rotor inlet and outlet. Also, at optimal design conditions stator losses were seen to be comparable to rotor losses. Moreover, the meanline design code was validated against CFD calculations and a fairly good agreement was found concerning the total-to-total efficiency.

A design code for convergent-divergent RIT vanes was developed, together with the extension to dense gases of a Method of Characteristics algorithm used to shape the divergent section. The accuracy of the method was assessed comparing the design requirements against the CFD results of the vane profiles, showing an excellent agreement. The method was exploited to address research questions concerning the effects of the stator design parameters on stator losses and stator downstream flow field uniformity. The stator downstream pitch-wise non-uniformity was discussed, correlating the distributions to the flow structures that characterize the flow field, and particularly high levels of pitch-wise non uniformity were observed in all investigated cases.

Most notably, the stator downstream flow field uniformity and the stator efficiency showed conflicting trends. This brought up additional research questions concerning the relative weight that should be given to each of the two design requirements and the effects of different levels of non-uniformity on the unsteady stator-rotor interaction and stage efficiency.

To address these research questions, unsteady CFD calculations have been carried out on stage configurations obtained matching the same rotor design to two different stators, each of them selected from one of the two conflicting objectives.

Remarkably high levels of stator-rotor interaction and power output fluctuations, that increase as the stator downstream non-uniformity increases, were noticed. Furthermore, this evidence suggests that the stator downstream uniformity can be used to take into account the stator design repercussions on rotor unsteady operation.

Surprisingly, the unsteady calculations showed that the optimal configuration is the one equipped with the optimal stator from downstream uniformity point of view, despite its lower stator efficiency. This finding suggests that for this class of turbines the stator downstream non-uniformity is a particularly crucial issue and that an improvement of this parameter could be more beneficial than a stator efficiency increase, if the effect on rotor operation is not accounted for.

Eventually, the influence of the stator-rotor radial gap was investigated and the results showed that it has a non-negligible impact on losses and expansion ratio share between vaned and vaneless region of the stationary part of the machine.

Based on the results showed in the present thesis, some design recommendations can be drawn. Designing single stage high efficiency RITs for small scale ORC plants appears possible. However, this generally entails highly supersonic flows at stator discharge, which in turn lead to relevant levels of stator downstream non-uniformity. In view of the conflicting trends of stator efficiency and stator downstream uniformity, multi-objective optimization strategies are recommended to deal with the stator design. Particularly, improving the stator downstream uniformity appears lively to improve the stage efficiency and to relieve the fluctuations of power output and aerodynamic forces on rotor blade. Nonetheless, upon designing the stator, the radial gap size must be properly accounted for, in order to select an appropriate target Mach number for the Method of Characteristics. Furthermore, the results presented highlight that the optimal turbine candidate from stage efficiency point of view may not necessarily correspond to the isolated stator and rotor efficiency optima, envisaging the need for multi-row simultaneous optimization.

Concerning the turbine design process, it is interesting to notice that the approach followed in the work proved to be particularly effective, delivering relatively high efficiency 3D turbine design candidates at inexpensive computational cost. On the other hand, improvements of turbine efficiency and mitigation of power output fluctuations could be achieved resorting to multi-objective optimization strategies. Particularly, their use is highly recommended to deal with aspects that are neglected by the design process adopted, such as the stator downstream non-uniformity.

Finally, among the possible future developments of the present work, the most relevant ones concern both the improvement of the design tools and the extension of the parametric analyses. Particularly, the improvement of the total-to-static efficiency prediction provided by the meanline code, the extension of the investigated stator data set –accounting for other fluids and various target Mach number for the Method of Characteristics, as well as the multi-objective optimization of the stator profiles are recommended.

Bibliography

Abagnale, C., Cameretti, M. C., De Robbio, R., and Tuccillo, R. (June 2017). "Thermal Cycle and Combustion Analysis of a Solar-Assisted Micro Gas Turbine". In: 10.6, p. 773. DOI: 10.3390/en10060773.

Ahmadi, P., Dincer, I., and Rosen, M. A. (Dec. 2012). "Exergo-environmental analysis of an integrated organic Rankine cycle for trigeneration". In: *Energy Conversion and Management* 64, pp. 447–453. DOI: 10.1016/j.enconman.2012.06.001.

Ahmadi, P., Rosen, M. A., and Dincer, I. (Oct. 2012). "Multi-objective exergy-based optimization of a polygeneration energy system using an evolutionary algorithm". In: *Energy* 46.1, pp. 21–31. DOI: 10.1016/j.energy.2012.02.005.

Aldo, A. C. and Argrow, B. M. (1993). "Supersonic minimum length nozzle design for dense gases". In: *The Fifth Annual Thermal and Fluids Analysis Workshop*. URL: https://ntrs.nasa.gov/search.jsp?R=19940019183.

Alshammari, F., Karvountzis-Kontakiotis, A., Pesiridis, A., and Giannakakis, P. (Sept. 2018). "Off-design performance prediction of radial turbines operating with ideal and real working fluids". In: *Energy Conversion and Management* 171, pp. 1430–1439. DOI: 10.1016/j.enconman.2018.06.093.

Alshammari, F., Kontakiotis, A. K., and Pesyridis, A. (2018). "Effect of radial turbo-expander design on off-highway vehicle organic Rankine cycle system efficiency". In: 7.1/2/3, p. 72. DOI: 10.1504/ijpt.2018.090364.

Alshammari, F., Pesyridis, A., Karvountzis-Kontakiotis, A., Franchetti, B., and Pesmazoglou, Y. (Apr. 2018). "Experimental study of a small scale organic Rankine cycle waste heat recovery system for a heavy duty diesel engine with focus on the radial inflow turbine expander performance". In: *Applied Energy* 215, pp. 543–555. DOI: 10.1016/j.apenergy.2018.01.049.

Anand, N., Colonna, P., and Pini, M. (July 2020). "Design guidelines for supersonic stators operating with fluids made of complex molecules". In: *Energy* 203, p. 117698. DOI: 10.1016/j.energy.2020.117698.

Anand, N., Vitale, S., Pini, M., Otero, G. J., and Pecnik, R. (Nov. 2018). "Design Methodology for Supersonic Radial Vanes Operating in Non-ideal Flow Conditions". In: *Journal of Engineering for Gas Turbines and Power* 141.2. DOI: 10.1115/1.4040182.

Argrow, B. M. and Emanuel, G. (Sept. 1988). "Comparison of Minimum Length Nozzles". In: *Journal of Fluids Engineering* 110.3, pp. 283–288. DOI: 10.1115/1.3243546.

Argrow, B. M. and Emanuel, G. (Sept. 1991). "Computational Analysis of the Transonic Flow Field of Two-Dimensional Minimum Length Nozzles". In: *Journal of Fluids Engineering* 113.3, pp. 479–488. DOI: 10.1115/1.2909521.

Astolfi, M. (2017). "Technical options for Organic Rankine Cycle systems". In: *Organic Rankine Cycle (ORC) Power Systems*. Elsevier. Chap. 3, pp. 67–89. DOI: 10.1016/b978-0-08-100510-1.00003-x.

Aungier, R. H. (2006a). "Aerodynamic Performance Analysis of Axial-Flow Turbines". In: *Turbine Aerodynamics: Axial-Flow and Radial-Flow Turbine Design and Analysis*. ASME Press. Chap. 5, pp. 93–131. DOI: 10.1115/1.802418.ch5.

Aungier, R. H. (2006b). "Aerodynamic Performance Analysis of Radial-Inflow Turbines". In: *Turbine Aerodynamics: Axial-Flow and Radial-Flow Turbine Design and Analysis*. ASME. Chap. 9. ISBN: 0791802418. URL: http://dx.doi.org/10.1115/1.802418.ch9.

Aungier, R. H. (2006c). "Preliminary Aerodynamic Design of Axial-Flow Turbine Stages". In: *Turbine Aerodynamics: Axial-Flow and Radial-Flow Turbine Design and Analysis*. ASME Press. Chap. 6, pp. 133–166. DOI: 10.1115/1.802418.ch6.

Aungier, R. H. (2006d). "Preliminary Aerodynamic Design of Radial-Inflow Turbine Stages". In: *Turbine Aerodynamics: Axial-Flow and Radial-Flow Turbine Design and Analysis*. ASME. Chap. 10. ISBN: 0791802418. URL: http://dx.doi.org/10.1115/1.802418.ch10.

Avery, W. H. and Wu, C. (1994). *Renewable energy from the ocean: a guide to OTEC*. Oxford University Press.

Bahamonde, S., Pini, M., De Servi, C., Rubino, A., and Colonna, P. (2017). "Method for the preliminary fluid dynamic design of high-temperature mini-organic rankine cycle turbines". In: *Journal of Engineering for Gas Turbines and Power* 139.8, p. 082606.

Bahamonde, S., Pini, M., Servi, C. D., and Colonna, P. (Dec. 2017). "Active subspaces for the optimal meanline design of unconventional turbomachinery". In: 127, pp. 1108–1118. DOI: 10.1016/j.applthermaleng.2017.08.093.

Balje´, O. E. (1962). "A Study on Design Criteria and Matching of Turbomachines: Part A—Similarity Relations and Design Criteria of Turbines". In: *Journal of Engineering for Power* 84.1, pp. 83–102. DOI: 10.1115/1.3673386.

Baumgärtner, D., Otter, J. J., and Wheeler, A. P. S. (2020). "The Effect of Isentropic Exponent on Transonic Turbine Performance". In: *Journal of Turbomachinery* 142 (8). DOI: https://doi.org/10.1115/1.4046528. URL: https://doi.org/10.1115/1.4046528.

Baumgärtner, D., Otter, J. J., and Wheeler, A. P. S. (June 2021a). "The Effect of Compressibility Factor on Turbine Performance". In: *Turbo Expo: Power for Land, Sea, and Air*. American Society of Mechanical Engineers. DOI: 10.1115/gt2021-60241.

Baumgärtner, D., Otter, J. J., and Wheeler, A. P. S. (2021b). "The Effect of Isentropic Exponent on Supersonic Turbine Wakes". In: *Proceedings of the 3rd International Seminar on Non-Ideal Compressible Fluid Dynamics for Propulsion and Power*. Springer International Publishing, pp. 153–161. DOI: 10.1007/978-3-030-69306-0_16.

Bell, I. and Lemmon, E. (2017). "Organic fluids for Organic Rankine Cycle systems". In: *Organic Rankine Cycle (ORC) Power Systems*. Elsevier. Chap. 4, pp. 91–119. DOI: 10.1016/b978-0-08-100510-1.00004-1.

Bell, I. H., Wronski, J., Quoilin, S., and Lemort, V. (2014). "Pure and Pseudo-pure Fluid Thermophysical Property Evaluation and the Open-Source Thermophysical Property Library CoolProp". In: *Industrial & Engineering Chemistry Research* 53 (6), pp. 2498–2508. DOI: https://doi.org/10.1021/ie4033999.

Bianchi, G., Panayiotou, G. P., Aresti, L., Kalogirou, S. A., Florides, G. A., Tsamos, K., Tassou, S. A., and Christodoulides, P. (Sept. 2019). "Estimating the waste heat recovery in the European Union Industry". In: *Energy, Ecology and Environment* 4.5, pp. 211–221. DOI: 10.1007/s40974-019-00132-7.

Bindon, J. P. and Carmichael, A. D. (Oct. 1971). “Streamline Curvature Analysis of Compressible and High Mach Number Cascade Flows”. In: 13.5, pp. 344–357. DOI: `10.1243/jmes_jour_1971_013_053_02`.

Bombarda, P., Invernizzi, C., and Gaia, M. (Mar. 2013). “Performance Analysis of OTEC Plants With Multilevel Organic Rankine Cycle and Solar Hybridization”. In: *Journal of Engineering for Gas Turbines and Power* 135.4. DOI: `10.1115/1.4007729`.

Bosman, C. and El-Shaarawi, M. A. I. (Mar.). “Quasi-Three-Dimensional Numerical Solution of Flow in Turbomachines”. In: *Journal of Fluids Engineering* 99.1, pp. 132–140. DOI: `doi:10.1115/1.3448514`. URL: `http://dx.doi.org/10.1115/1.3448514`.

Boyaghchi, F. A. and Heidarnejad, P. (June 2015). “Thermoeconomic assessment and multi objective optimization of a solar micro CCHP based on Organic Rankine Cycle for domestic application”. In: *Energy Conversion and Management* 97, pp. 224–234. DOI: `10.1016/j.enconman.2015.03.036`.

Bronicki, L. (2017). “History of Organic Rankine Cycle systems”. In: *Organic Rankine Cycle (ORC) Power Systems.* Elsevier. Chap. 2, pp. 25–66. DOI: `10.1016/b978-0-08-100510-1.00002-8`.

Bronicki, L. Y. and Schochet, D. N. (2005). “Bottoming organic cycle for gas turbines”. In: vol. 47284. Turbo Expo: Power for Land, Sea, and Air. Reno-Tahoe, pp. 79–86. DOI: `doi.org/10.1115/GT2005-68121`.

Brown, B. (1947). *Friction coefficients in a vaneless diffuser.* Tech. rep. No. 1311. NACA. URL: `https://ntrs.nasa.gov/archive/nasa/casi.ntrs.nasa.gov/19930081992.pdf`.

Bruno, J. C., López-Villada, J., Letelier, E., Romera, S., and Coronas, A. (Dec. 2008). “Modelling and optimisation of solar organic rankine cycle engines for reverse osmosis desalination”. In: *Applied Thermal Engineering* 28.17-18, pp. 2212–2226. DOI: `10.1016/j.applthermaleng.2007.12.022`.

Cameretti, M. C., Ferrara, F., Gimelli, A., and Tuccillo, R. (Dec. 2015a). “Combined MGT – ORC Solar – Hybrid System. PART A: Plant Optimization”. In: 81, pp. 368–378. DOI: `10.1016/j.egypro.2015.12.106`.

Cameretti, M. C., Ferrara, F., Gimelli, A., and Tuccillo, R. (Dec. 2015b). “Combined MGT – ORC Solar – Hybrid System. PART B: Component Analysis and Prime Mover Selection”. In: 81, pp. 379–389. DOI: `10.1016/j.egypro.2015.12.107`.

Cameretti, M. C., Ferrara, F., Gimelli, A., and Tuccillo, R. (June 2015c). “Employing Micro-Turbine Components in Integrated Solar-MGT-ORC

Power Plants". In: American Society of Mechanical Engineers. DOI: 10.1115/gt2015-42572.

Canada, S., Cohen, G., Cable, R., Brosseau, D., and Price, H. (Jan. 2005). "Parabolic Trough Organic Rankine Cycle Power Plant". In: URL: https://www.osti.gov/biblio/860827.

Capozzoli, A. and Primiceri, G. (Dec. 2015). "Cooling Systems in Data Centers: State of Art and Emerging Technologies". In: *Energy Procedia* 83, pp. 484–493. DOI: 10.1016/j.egypro.2015.12.168.

Cappiello, A. (2020). "Poster: An Application of Conventional First Guess Geometry Rules to ORC Radial-Inflow Turbine Rotors: A Critical Assessment (GT2020–16005)". In: *Turbo Expo: Power for Land, Sea, and Air*. American Society of Mechanical Engineers.

Cappiello, A. and Tuccillo, R. (2020). "Design and CFD Analysis of a Radial-Inflow Turbine for Small Scale ORC Applications". In: *75th National ATI Congress – # 7 Clean Energy for all (ATI 2020)*. Vol. 197. Roma: E3S Web Conf. DOI: 10.1051/e3sconf/202019711005. URL: https://doi.org/10.1051/e3sconf/202019711005.

Cappiello, A. and Tuccillo, R. (June 2021a). "Influence of Supersonic Nozzle Design Parameters on the Unsteady Stator-Rotor Interaction in Radial-Inflow Turbines for Organic Rankine Cycles". In: *Turbo Expo: Power for Land, Sea, and Air*. American Society of Mechanical Engineers. DOI: 10.1115/gt2021-59123.

Cappiello, A. (2021). "Progettazione di una turbina a flusso radiale ad alto rapporto di espansione per ciclo Rankine organico di piccola taglia". In: *La Termotecnica*. URL: https://www.latermotecnica.net/newsletter_TER/2021_05/maggio_2021.htm.

Cappiello, A., Majer, M., Tuccillo, R., and Pini, M. (2022). "On the Influence of Stator-Rotor Radial Gap Size on the Fluid-Dynamic performance of Mini-ORC Supersonic Turbines". In: *Turbo Expo: Power for Land, Sea, and Air*. American Society of Mechanical Engineers.

Cappiello, A. and Tuccillo, R. (Sept. 2021b). "Design Parameter Influence on Losses and Downstream Flow Field Uniformity in Supersonic ORC Radial-Inflow Turbine Stators". In: *International Journal of Turbomachinery, Propulsion and Power* 6.3, p. 38. DOI: 10.3390/ijtpp6030038.

Cappiello, A. and Tuccillo, R. (2022). "Influence of Supersonic Nozzle Design Parameters on the Unsteady Stator-Rotor Interaction in Radial-Inflow Turbines for Organic Rankine Cycles". In: *Journal of Turbomachinery*. DOI: 10.1115/1.4054068.

Cappiello, A., Tuccillo, R., Cameretti, M. C., and Pesyridis, A. (2019). "Axial Flow Turbine Concept for Conventional and e-Turbocharging". In:

14th International Conference on Engines & Vehicles. SAE Technical Paper. DOI: https://doi.org/10.4271/2019-24-0185.

Chen, H., Goswami, D. Y., and Stefanakos, E. K. (2010). "A review of thermodynamic cycles and working fluids for the conversion of low-grade heat". In: *Renewable and sustainable energy reviews* 14.9, pp. 3059–3067.

Clemente, S., Micheli, D., Reini, M., and Taccani, R. (2013). "Bottoming organic Rankine cycle for a small scale gas turbine: A comparison of different solutions". In: *Applied energy* 106, pp. 355–364. DOI: doi.org/10.1016/j.apenergy.2013.02.004.

Colonna, P., Rebay, S., Harinck, J., and Guardone, A. (2006). "Real-gas effects in ORC turbine flow simulations: influence of thermodynamic models on flow fields and performance parameters". In: *ECCOMAS CFD 2006 Conference, Egmond Aan Zee, North Holland.*

Colonna, P. and Guardone, A. (May 2006). "Molecular interpretation of nonclassical gas dynamics of dense vapors under the van der Waals model". In: *Physics of Fluids* 18.5, p. 056101. DOI: 10.1063/1.2196095.

Colonna, P., Nannan, N., Guardone, A., and Stelt, T. van der (Nov. 2009). "On the computation of the fundamental derivative of gas dynamics using equations of state". In: 286.1, pp. 43–54. DOI: 10.1016/j.fluid.2009.07.021.

Colonna, P., Casati, E., Trapp, C., Mathijssen, T., Larjola, J., Turunen-Saaresti, T., and Uusitalo, A. (2015). "Organic Rankine Cycle Power Systems: From the Concept to Current Technology, Applications, and an Outlook to the Future". In: *Journal of Engineering for Gas Turbines and Power* 137.10, pp. 100801-1-100801–19. DOI: 10.1115/1.4029884. URL: http://dx.doi.org/10.1115/1.4029884.

Cramer, M. and Crickenberger, A. (1992). "Prandtl-Meyer function for dense gases". In: *AIAA journal* 30.2, pp. 561–564.

d'Amelio, L. (1936a). "La Turbina a Vapore ed i cicli Binari con Fluidi Diversi Dall'acqua Fra le Isoterme Inferiori". In: *L'Elettrotecnica* 23.9, pp. 250–257.

d'Amelio, L. (1936b). "La Turbina a Vapore ed i cicli Binari con Fluidi Diversi Dall'acqua Fra le Isoterme Inferiori". In: *L'Elettrotecnica* 23.10, pp. 286–292.

d'Amelio, L. (1935). "Impiego di vapori ad alto peso molecolare in piccole turbine e utilizzazione del calore solare per energia motrice". In: *Industria Napoletana Arti Grafiche.*

D'Auria, D. (2020). "Thermo-Economic Analysis of Organic Rankine Cycles for Most Promising Heat Recovery from Market Perspective". MA thesis.

SCUOLA POLITECNICA DELLE SCIENZE DI BASE, University of Naples, Federico II.

Da Lio, L., Manente, G., and Lazzaretto, A. (Nov. 2017). "A mean-line model to predict the design efficiency of radial inflow turbines in organic Rankine cycle (ORC) systems". In: *Applied Energy* 205, pp. 187–209. DOI: `10.1016/j.apenergy.2017.07.120`.

De Servi, C. M., Burigana, M., Pini, M., and Colonna, P. (2019). "Design Method and Performance Prediction for Radial-Inflow Turbines of High-Temperature Mini-Organic Rankine Cycle Power Systems". In: *Journal of Engineering for Gas Turbines and Power* 141 (9). DOI: `https://doi.org/10.1115/1.4043973`.

Deich, M. E. (1956). *Flow of Gas Through Turbine Lattices*. 1393. National Advisory Committee for Aeronautics.

Dixon, S. L. and Hall, C. (2013). *Fluid mechanics and thermodynamics of turbomachinery*. Butterworth-Heinemann.

Ebrahimi, K., Jones, G., and Fleischer, A. (May 2014). "A review of challenging issues in the integration of absorption refrigeration and organic Rankine Cycle into a data center cooling system". In: *Fourteenth Intersociety Conference on Thermal and Thermomechanical Phenomena in Electronic Systems (ITherm)*. IEEE. DOI: `10.1109/itherm.2014.6892397`.

Ebrahimi, K., Jones, G. F., and Fleischer, A. S. (Nov. 2017). "The viability of ultra low temperature waste heat recovery using organic Rankine cycle in dual loop data center applications". In: *Applied Thermal Engineering* 126, pp. 393–406. DOI: `10.1016/j.applthermaleng.2017.07.001`.

Espinosa, N., Tilman, L., Lemort, V., Quoilin, S., and Lombard, B. (2010). "Rankine cycle for waste heat recovery on commercial trucks: approach, constraints and modelling". In: *Diesel International Conference and Exhibition*. URL: `http://hdl.handle.net/2268/62995`.

Fiaschi, D., Innocenti, G., Manfrida, G., and Maraschiello, F. (2016). "Design of micro radial turboexpanders for ORC power cycles: From 0D to 3D". In: *Applied Thermal Engineering* 99, pp. 402–410. ISSN: 1359-4311. DOI: `https://doi.org/10.1016/j.applthermaleng.2015.11.087`. URL: `http://www.sciencedirect.com/science/article/pii/S1359431115013332`.

Fiaschi, D., Manfrida, G., and Maraschiello, F. (2012). "Thermo-fluid dynamics preliminary design of turbo-expanders for ORC cycles". In: *Applied Energy* 97. Energy Solutions for a Sustainable World - Proceedings of the Third International Conference on Applied Energy, May 16-18, 2011 - Perugia, Italy, pp. 601–608. ISSN: 0306-2619. DOI: `https:`

//doi.org/10.1016/j.apenergy.2012.02.033. URL: http://www.sciencedirect.com/science/article/pii/S0306261912001274.

Forman, C., Muritala, I. K., Pardemann, R., and Meyer, B. (May 2016). "Estimating the global waste heat potential". In: *Renewable and Sustainable Energy Reviews* 57, pp. 1568–1579. DOI: 10.1016/j.rser.2015.12.192.

Fransson, T., Jocker, M., Bolcs, A., and Ott, P. (1999). "Viscous and inviscid linear/nonlinear calculations versus quasi-three-dimensional experimental cascade data for a new aeroelastic turbine standard configuration". In: *Journal of Turbomachinery* 121.4, pp. 717–725. DOI: doi:10.1115/1.2836725.

Fu, C., Zou, Z., Kong, Q., Cheng, H., and Zhang, W. (2016). "Aerodynamic Design and Numerical Analysis of Supersonic Turbine for Turbo Pump". In: *International Journal of Turbo & Jet-Engines* 33 (3), pp. 239–252. DOI: https://doi.org/10.1515/tjj-2015-0028. URL: https://www.degruyter.com/view/journals/tjj/33/3/article-p239.xml.

Galiana, F. D., Wheeler, A., Ong, J., and M Ventura, C. de (Mar. 2017). "The effect of dense gas dynamics on loss in ORC transonic turbines". In: *Journal of Physics: Conference Series* 821, p. 012021. DOI: 10.1088/1742-6596/821/1/012021.

Galiana, F. J. D., Wheeler, A. P., and Ong, J. (June 2016). "A Study of Trailing-Edge Losses in Organic Rankine Cycle Turbines". In: *Journal of Turbomachinery* 138.12. DOI: 10.1115/1.4033473.

García-Rodríguez, L. and Delgado-Torres, A. M. (June 2007). "Solar-powered Rankine cycles for fresh water production". In: *Desalination* 212.1-3, pp. 319–327. DOI: 10.1016/j.desal.2006.10.016.

Giuffre', A. and Pini, M. (Dec. 2020). "Design Guidelines for Axial Turbines Operating With Non-Ideal Compressible Flows". In: *Journal of Engineering for Gas Turbines and Power* 143.1. DOI: 10.1115/1.4049137.

Glassman, A. J. (1976). *Computer program for design analysis of radial-inflow turbines.* Tech. rep. TN-D-8164. Lewis Research Center Clevehnd, Ohio: NASA. URL: https://ntrs.nasa.gov/citations/19760010058.

Goldman, L. J. (Mar. 1972). "Supersonic Turbine Design and Performance". In: *ASME 1972 International Gas Turbine and Fluids Engineering Conference and Products Show.* American Society of Mechanical Engineers. DOI: 10.1115/72-gt-63.

Goldman, L. J. and Vanco, M. R. (1971). *Computer program for design of two-dimensional sharp-edged-throat supersonic nozzle with boundary layer correction.* Tech. rep. NASA-TM-X-2343. NASA. URL: https://ntrs.nasa.gov/citations/19710023317.

Goldman, L. J. (1994). *Supersonic Turbines.* Washington: NASA, pp. 249–278. URL: https://ntrs.nasa.gov/search.jsp?R=19950015924.

Goldstein, A. W. and Jerison, M. (1947). *Isolated and cascade airfoils with prescribed velocity distribution.* Tech. rep. FLIGHT PROPULSION RESEARCH LAB CLEVELAND OH. URL: https://apps.dtic.mil/sti/pdfs/ADA298727.pdf.

Guardone, A. and Vimercati, D. (July 2016). "Exact solutions to non-classical steady nozzle flows of Bethe–Zel'dovich–Thompson fluids". In: *Journal of Fluid Mechanics* 800, pp. 278–306. DOI: 10.1017/jfm.2016.392.

Guercio, A. and Bini, R. (2017). "Biomass-fired Organic Rankine Cycle combined heat and power systems". In: *Organic Rankine Cycle (ORC) Power Systems.* Elsevier, pp. 527–567. DOI: 10.1016/b978-0-08-100510-1.00015-6.

Györke, G., Groniewsky, A., and Imre, A. (Feb. 2019). "A Simple Method of Finding New Dry and Isentropic Working Fluids for Organic Rankine Cycle". In: 12.3, p. 480. DOI: 10.3390/en12030480.

Harinck, J., Guardone, A., and Colonna, P. (Aug. 2009). "The influence of molecular complexity on expanding flows of ideal and dense gases". In: 21.8, p. 086101. DOI: 10.1063/1.3194308.

Harinck, J., Pasquale, D., Pecnik, R., Buijtenen, J. van, and Colonna, P. (2013). "Performance improvement of a radial organic Rankine cycle turbine by means of automated computational fluid dynamic design". In: *Proceedings of the Institution of Mechanical Engineers, Part A: Journal of Power and Energy* 227 (6), pp. 637–645. DOI: 10.1177/0957650913499565. URL: https://journals.sagepub.com/doi/full/10.1177/0957650913499565.

Harinck, J., Turunen-Saaresti, T., Colonna, P., Rebay, S., and Buijtenen, J. van (2010). "Computational Study of a High-Expansion Ratio Radial Organic Rankine Cycle Turbine Stator". In: *Journal of Engineering for Gas Turbines and Power* 132 (5). DOI: 10.1115/1.3204505. URL: https://doi.org/10.1115/1.3204505.

Heppenstall, T. (Sept. 1998). "Advanced gas turbine cycles for power generation: a critical review". In: 18.9-10, pp. 837–846. DOI: 10.1016/s1359-4311(97)00116-6.

Ho, T., Mao, S. S., and Greif, R. (June 2012). "Comparison of the Organic Flash Cycle (OFC) to other advanced vapor cycles for intermediate and high temperature waste heat reclamation and solar thermal energy". In: *Energy* 42.1, pp. 213–223. DOI: 10.1016/j.energy.2012.03.067.

Hoarau, J.-C., Cinnella, P., and Gloerfelt, X. (Feb. 2021). "Large Eddy Simulations of Strongly Non-Ideal Compressible Flows through a Transonic Cascade". In: 14.3, p. 772. DOI: 10.3390/en14030772.

Hoffren, J., Talonpoika, T., Larjola, J., and Siikonen, T. (2002). "Numerical Simulation of Real-Gas Flow in a Supersonic Turbine Nozzle Ring". In: *Journal of Engineering for Gas Turbines and Power* 124 (2), pp. 395–403. DOI: 10.1115/1.1423320. URL: https://doi.org/10.1115/1.1423320.

Ikegami, Y. and Morisaki, T. (June 2012). "Research On Double Stage-Rankine Cycle For Ocean Thermal Energy Conversion Using Ammonia As Working Fluid". In: *The Twenty-second International Offshore and Polar Engineering Conference.* Vol. All Days. International Ocean and Polar Engineering Conference. ISOPE-I-12-036. eprint: https://onepetro.org/ISOPEIOPEC/proceedings-pdf/ISOPE12/All-ISOPE12/ISOPE-I-12-036/1604186/isope-i-12-036.pdf.

Invernizzi, C., Iora, P., and Silva, P. (2007). "Bottoming micro-Rankine cycles for micro-gas turbines". In: *Applied thermal engineering* 27 (1), pp. 100–110. DOI: doi.org/10.1016/j.applthermaleng.2006.05.003.

Jamieson, A. (1955). "Gas turbine principles and practice". In: ed. by S. H. R. Cox. George Newnes London. Chap. The radial turbine.

Japikse (1982). "Advanced diffusion levels in turbocharger compressors and component matching". In: *First International Conference on Turbocharging and Turbochargers IMechE.*

Johnston, I. H. and Dransfield, D. C. (1959). *The Test Performance of Highly Loaded Turbine Stages Designed for High Pressure Ratio.* Tech. rep. London: HM Stationery Office. DOI: doi=10.1.1.227.2268. URL: http://citeseerx.ist.psu.edu/viewdoc/download?doi=10.1.1.227.2268&rep=rep1&type=pdf.

Kang, S. H. (2012). "Design and experimental study of ORC (organic Rankine cycle) and radial turbine using R245fa working fluid". In: *Energy* 41 (1), pp. 514–524. DOI: doi.org/10.1016/j.energy.2012.02.035. URL: http://www.sciencedirect.com/science/article/pii/S0360544212001302.

Karvountzis-Kontakiotis, A., Pesiridis, A., Zhao, H., Alshammari, F., Franchetti, B., Pesmazoglou, I., and Tocci, L. (Mar. 2017). "Effect of an ORC Waste Heat Recovery System on Diesel Engine Fuel Economy for Off-Highway Vehicles". In: SAE International. DOI: 10.4271/2017-01-0136.

Katsanis, T. (Dec. 1964). *Use of arbitrary quasi-orthogonals for calculating flow distribution in the meridional plane of a turbomachine.* Tech. rep.

TN-D-2546. NASA. URL: https://ntrs.nasa.gov/citations/19650002705.

Katsanis, T. (May 1965). *Use of arbitrary quasi-orthogonals for calculating flow distribution on a blade-to-blade surface in a turbomachine.* Tech. rep. TN-D-2809. NASA. URL: https://ntrs.nasa.gov/citations/19650013567.

Katsanis, T. (1966). "Use of arbitrary quasi-orthogonals for calculating flow distribution in a turbomachine". In: *Journal of Engineering for Power* 88.2, pp. 197–202. DOI: doi:10.1115/1.3678504.

Khalil, I. M., Tabakoff, W., and Hamed, A. (Sept. 1976). "Losses in Radial Inflow Turbines". In: *Journal of Fluids Engineering* 98.3, pp. 364–371. DOI: 10.1115/1.3448323.

Klonowicz, P., Heberle, F., Preißinger, M., and Brüggemann, D. (Aug. 2014). "Significance of loss correlations in performance prediction of small scale, highly loaded turbine stages working in Organic Rankine Cycles". In: *Energy* 72, pp. 322–330. DOI: 10.1016/j.energy.2014.05.040.

Lampe, M., Servi, C. D., Schilling, J., Bardow, A., and Colonna, P. (Oct. 2019). "Toward the Integrated Design of Organic Rankine Cycle Power Plants: A Method for the Simultaneous Optimization of Working Fluid, Thermodynamic Cycle, and Turbine". In: 141.11. DOI: 10.1115/1.4044380.

Lang, W., Colonna, P., and Almbauer, R. (Mar. 2013). "Assessment of Waste Heat Recovery From a Heavy-Duty Truck Engine by Means of an ORC Turbogenerator". In: 135.4. DOI: 10.1115/1.4023123.

Lemmon, E. W., Huber, M. L., and McLinden, M. O. (2010). "NIST standard reference database 23". In: *Reference fluid thermodynamic and transport properties (REFPROP), version* 9.

Lemort, V., Guillaume, L., Legros, A., Declaye, S., and Quoilin, S. (2013). "A comparison of piston, screw and scroll expanders for small scale Rankine cycle systems". In: *Proceedings of the 3rd international conference on microgeneration and related technologies.*

Li, M., Wang, J., He, W., Gao, L., Wang, B., Ma, S., and Dai, Y. (2013). "Construction and preliminary test of a low-temperature regenerative Organic Rankine Cycle (ORC) using R123". In: *Renewable Energy* 57, pp. 216–222. DOI: doi.org/10.1016/j.renene.2013.01.042. URL: http://www.sciencedirect.com/science/article/pii/S0960148113000803.

Macchi, E. (2017a). "Theoretical basis of the Organic Rankine Cycle". In: *Organic Rankine Cycle (ORC) Power Systems.* Elsevier. Chap. 1, pp. 3–24. DOI: 10.1016/b978-0-08-100510-1.00001-6.

Macchi, E. (2017b). *Theoretical basis of the Organic Rankine Cycle*. Woodhead Publishing. Chap. 1, pp. 3–24. DOI: https://doi.org/10.1016/B978-0-08-100510-1.00001-6.

Marconcini, M., Rubechini, F., Arnone, A., Greco, A. S. D., and Biagi, R. (June 2012). "Aerodynamic Investigation of a High Pressure Ratio Turbo-Expander for Organic Rankine Cycle Applications". In: *Volume 8: Turbomachinery, Parts A, B, and C*. American Society of Mechanical Engineers. DOI: 10.1115/gt2012-69409.

Markides, C. N. (Dec. 2015). "Low-Concentration Solar-Power Systems Based on Organic Rankine Cycles for Distributed-Scale Applications: Overview and Further Developments". In: *Frontiers in Energy Research* 3. DOI: 10.3389/fenrg.2015.00047.

Meroni, A., Robertson, M., Martinez-Botas, R., and Haglind, F. (Dec. 2018). "A methodology for the preliminary design and performance prediction of high-pressure ratio radial-inflow turbines". In: *Energy* 164, pp. 1062–1078. DOI: 10.1016/j.energy.2018.09.045.

Moffitt, T. P. (1958). *Maximum theoretical tangential velocity component possible from straight-back converging and converging-diverging stators at supercritical pressure ratios*. Tech. rep. Cleveland: NACA. URL: https://ntrs.nasa.gov/search.jsp?R=19930085040.

Monaco, J. F., Cramer, M. S., and Watson, L. T. (Jan. 1997). "Supersonic flows of dense gases in cascade configurations". In: *Journal of Fluid Mechanics* 330, pp. 31–59. DOI: 10.1017/s0022112096003564.

Moradi, R., Marcantonio, V., Cioccolanti, L., and Bocci, E. (Feb. 2020). "Integrating biomass gasification with a steam-injected micro gas turbine and an Organic Rankine Cycle unit for combined heat and power production". In: 205, p. 112464. DOI: 10.1016/j.enconman.2019.112464.

Mounier, V., Olmedo, L. E., and Schiffmann, J. (Jan. 2018). "Small scale radial inflow turbine performance and pre-design maps for Organic Rankine Cycles". In: *Energy* 143, pp. 1072–1084. DOI: 10.1016/j.energy.2017.11.002.

Najjar, Y. S. (Mar. 2001). "Efficient use of energy by utilizing gas turbine combined systems". In: 21.4, pp. 407–438. DOI: 10.1016/s1359-4311(00)00033-8.

Najjar, Y. S. and Radhwan, A. M. (Jan. 1988). "Cogeneration by combining gas turbine engine with organic rankine cycle". In: 8.3, pp. 211–219. DOI: 10.1016/0890-4332(88)90057-9.

Nguyen, V. M., Doherty, P. S., and Riffat, S. B. (2001). "Development of a prototype low-temperature Rankine cycle electricity generation system". In: *Applied Thermal Engineering* 21, pp. 169–181. DOI: doi.org/10.

1016/S1359-4311(00)00052-1. URL: http://www.sciencedirect.com/science/article/pii/S1359431100000521.

Ofeldt, F. W. (1898). U.S. pat. US611792 A. URL: https://patents.google.com/patent/US611792A/en.

Ohlsson, G. O. (1964). "Supersonic Turbines". In: *Journal of Engineering for Power* 86 (1), pp. 7–12. DOI: 10.1115/1.3675427. URL: https://doi.org/10.1115/1.3675427.

Oomori, H. and Ogino, S. (Mar. 1993). "Waste Heat Recovery of Passenger Car Using a Combination of Rankine Bottoming Cycle and Evaporative Engine Cooling System". In: SAE International. DOI: 10.4271/930880.

Orosz, M. and Dickes, R. (2017). "Solar thermal powered Organic Rankine Cycles". In: *Organic Rankine Cycle (ORC) Power Systems*. Elsevier, pp. 569–612. DOI: 10.1016/b978-0-08-100510-1.00016-8.

Otero Rodriguez, G. J., Smit, S. H., and Pecnik, R. (Feb. 2021). "Three-dimensional unsteady stator-rotor interactions in high-expansion organic Rankine cycle turbines". In: *Energy* 217, p. 119339. DOI: 10.1016/j.energy.2020.119339.

Otter, J. J., Baumgärtner, D., and Wheeler, A. P. S. (2021). "The Development of a Generic Working Fluid Approach for the Determination of Transonic Turbine Loss". In: *Proceedings of the 3rd International Seminar on Non-Ideal Compressible Fluid Dynamics for Propulsion and Power*. Springer International Publishing, pp. 123–131. DOI: 10.1007/978-3-030-69306-0_13.

Pasquale, D., Ghidoni, A., and Rebay, S. (2013). "Shape optimization of an organic rankine cycle radial turbine nozzle". In: *Journal of Engineering for Gas Turbines and Power* 135.4, p. 042308.

Pei, G., Li, J., Li, Y., Wang, D., and Ji, J. (2011). "Construction and dynamic test of a small-scale organic rankine cycle". In: *Energy* 36 (5), pp. 3215–3223. DOI: doi.org/10.1016/j.energy.2011.03.010. URL: http://www.sciencedirect.com/science/article/pii/S0360544211001666.

Peng, D.-Y. and Robinson, D. B. (1976). "A new two-constant equation of state". In: *Industrial & Engineering Chemistry Fundamentals* 15.1, pp. 59–64.

Perdichizzi, A. and Lozza, G. (1987). "Design criteria and efficiency prediction for radial inflow turbines". In: *ASME 1987 International Gas Turbine Conference and Exhibition*. American Society of Mechanical Engineers, V001T01A086–V001T01A086. DOI: http://dx.doi.org/10.1115/87-GT-231.

Persico, G. and Pini, M. (2017). "Fluid dynamic design of Organic Rankine Cycle turbines". In: *Organic Rankine Cycle (ORC) Power Systems*.

Elsevier. Chap. 8, pp. 253–297. DOI: 10.1016/b978-0-08-100510-1.00008-9.

Persico, G., Romei, A., Dossena, V., and Gaetani, P. (Dec. 2018). "Impact of shape-optimization on the unsteady aerodynamics and performance of a centrifugal turbine for ORC applications". In: *Energy* 165, pp. 2–11. DOI: 10.1016/j.energy.2018.09.044.

Persky, R. and Sauret, E. (Mar. 2019). "Loss models for on and off-design performance of radial inflow turbomachinery". In: *Applied Thermal Engineering* 150, pp. 1066–1077. DOI: 10.1016/j.applthermaleng.2019.01.042.

Piegl, L. and Tiller, W. (1997). *The NURBS Book*. Springer Berlin Heidelberg. DOI: 10.1007/978-3-642-59223-2.

Pini, M., Persico, G., Pasquale, D., and Rebay, S. (Oct. 2014). "Adjoint Method for Shape Optimization in Real-Gas Flow Applications". In: *Journal of Engineering for Gas Turbines and Power* 137.3. DOI: 10.1115/1.4028495.

Pini, M., Servi, C. D., Burigana, M., Bahamonde, S., Rubino, A., Vitale, S., and Colonna, P. (2017). "Fluid-dynamic design and characterization of a mini-ORC turbine for laboratory experiments". In: *Energy Procedia* 129, pp. 1141–1148. DOI: doi.org/10.1016/j.egypro.2017.09.186. URL: http://www.sciencedirect.com/science/article/pii/S1876610217341000.

Pini, M., Persico, G., Casati, E., and Dossena, V. (Mar. 2013). "Preliminary Design of a Centrifugal Turbine for Organic Rankine Cycle Applications". In: 135.4. DOI: 10.1115/1.4023122.

Qiu, G., Liu, H., and Riffat, S. (2011). "Expanders for micro-CHP systems with organic Rankine cycle". In: *Applied Thermal Engineering* 31.16, pp. 3301–3307. ISSN: 1359-4311. DOI: https://doi.org/10.1016/j.applthermaleng.2011.06.008. URL: http://www.sciencedirect.com/science/article/pii/S1359431111003188.

Quarteroni, A. (2009). *Numerical models for differential problems*. Vol. 2. Springer.

Quoilin, S., Orosz, M., Hemond, H., and Lemort, V. (May 2011). "Performance and design optimization of a low-cost solar organic Rankine cycle for remote power generation". In: *Solar Energy* 85.5, pp. 955–966. DOI: 10.1016/j.solener.2011.02.010.

Quoilin, S., Broek, M. V. D., Declaye, S., Dewallef, P., and Lemort, V. (2013). "Techno-economic survey of Organic Rankine Cycle (ORC) systems". In: *Renewable and Sustainable Energy Reviews* 22, pp. 168–186.

Rahbar, K., Mahmoud, S., Al-Dadah, R. K., Moazami, N., and Mirhadizadeh, S. A. (2017). "Review of organic Rankine cycle for small-scale applications". In: *Energy conversion and management* 134, pp. 135–155.

Reichert, A. W. and Simon, H. (1997). "Design and Flow Field Calculations for Transonic and Supersonic Radial Inflow Turbine Guide Vanes". In: *Journal of Turbomachinery* 119 (1), pp. 103–113. DOI: 10.1115/1.2840999. URL: https://doi.org/10.1115/1.2840999.

Rinaldi, E., Pecnik, R., and Colonna di Paliano, P. (2015). "Unsteady rans simulation of the off-design operation of a high expansion ratio ORC radial turbine". English. In: *Proceedings of the 3rd international seminar on ORC power systems*. Ed. by V. Lemort, S. Quoilin, M. De Paepe, and M. van den Broek. 3rd international seminar on ORC power systems, ASME-ORC 2015, Brussels, Belgium ; Conference date: 11-10-2015 Through 14-10-2015. United States: ASME, pp. 1–9.

Rinaldi, E., Pecnik, R., and Colonna, P. (July 2016). "Unsteady Operation of a Highly Supersonic Organic Rankine Cycle Turbine". In: *Journal of Turbomachinery* 138.12. DOI: 10.1115/1.4033973.

Ringler, J., Seifert, M., Guyotot, V., and Hübner, W. (Apr. 2009). "Rankine Cycle for Waste Heat Recovery of IC Engines". In: 2.1, pp. 67–76. DOI: 10.4271/2009-01-0174.

Roache, P. J. (Sept. 1994). "Perspective: A Method for Uniform Reporting of Grid Refinement Studies". In: *Journal of Fluids Engineering* 116.3, pp. 405–413. DOI: 10.1115/1.2910291.

Roache, P. J. (Jan. 1997). "QUANTIFICATION OF UNCERTAINTY IN COMPUTATIONAL FLUID DYNAMICS". In: *Annual Review of Fluid Mechanics* 29.1, pp. 123–160. DOI: 10.1146/annurev.fluid.29.1.123.

Roache, P. J., Ghia, K. N., and White, F. M. (Mar. 1986). "Editorial Policy Statement on the Control of Numerical Accuracy". In: *Journal of Fluids Engineering* 108.1, p. 2. DOI: 10.1115/1.3242537.

Robertson, M. C., Costall, A. W., Newton, P. J., and Martinez-Botas, R. F. (2016). "Radial Turboexpander Optimization Over Discretized Heavy-Duty Test Cycles for Mobile Organic Rankine Cycle Applications". In: *Proceedings of the ASME Turbo Expo 2016: Turbomachinery Technical Conference and Exposition.* 49743, V003T25A007–. URL: http://dx.doi.org/10.1115/GT2016-56754.

Rohlik, H. E. (1968). *Analytical determination of radial inflow turbine design geometry for maximum efficiency.* Tech. rep. TN D-4384. NASA. URL: https://ntrs.nasa.gov/archive/nasa/casi.ntrs.nasa.gov/19680006474.pdf.

Romei, A., Vimercati, D., Persico, G., and Guardone, A. (Nov. 2019). "Non-ideal compressible flows in supersonic turbine cascades". In: *Journal of Fluid Mechanics* 882. DOI: 10.1017/jfm.2019.796.

Rubechini, F., Marconcini, M., Arnone, A., Greco, A. S. D., and Biagi, R. (Aug. 2013). "Special Challenges in the Computational Fluid Dynamics Modeling of Transonic Turbo-Expanders". In: *Journal of Engineering for Gas Turbines and Power* 135.10. DOI: 10.1115/1.4025034.

Rubechini, F., Marconcini, M., Giovannini, M., Bellucci, J., and Arnone, A. (May 2015). "Accounting for Unsteady Interaction in Transonic Stages". In: *Journal of Engineering for Gas Turbines and Power* 137.5. DOI: 10.1115/1.4028667.

Sauer, R. (1947). *General Characteristics of the Flow Through Nozzles at Near CriticalSpeeds.* Technical Memorandum 1147. NACA.

Shapiro, A. H. and Edelman, G. M. (1947a). *Method of Characteristics for Two-dimensional Supersonic Flow: Graphical and Numerical Procedures.* Tech. rep.

Shapiro, A. H. (1953). *The dynamics and thermodynamics of compressible fluid flow.* New York: John Wiley & Sons.

Shapiro, A. H. and Edelman, G. M. (June 1947b). "Method of Characteristics for Two-Dimensional Supersonic Flow—Graphical and Numerical Procedures". In: *Journal of Applied Mechanics* 14.2, A154–A162. DOI: 10.1115/1.4009667.

Simpson, A. T., Spence, S. W. T., and Watterson, J. K. (Mar. 2013). "Numerical and Experimental Study of the Performance Effects of Varying Vaneless Space and Vane Solidity in Radial Turbine Stators". In: *Journal of Turbomachinery* 135.3. DOI: 10.1115/1.4007525.

Slade, S. and Palmer, C. (2019). "Worldwide Gas Turbine Forecast". In: *Turbomachinery Handbook* 59.6. URL: https://www.turbomachinerymag.com/view/worldwide-gas-turbine-forecast-2.

Soave, G. (June 1972). "Equilibrium constants from a modified Redlich-Kwong equation of state". In: 27.6, pp. 1197–1203. DOI: 10.1016/0009-2509(72)80096-4.

Song, J., Gu, C.-w., and Ren, X. (2016). "Influence of the radial-inflow turbine efficiency prediction on the design and analysis of the Organic Rankine Cycle (ORC) system". In: *Energy Conversion and Management* 123, pp. 308–316. ISSN: 0196-8904. DOI: https://doi.org/10.1016/j.enconman.2016.06.037. URL: http://www.sciencedirect.com/science/article/pii/S019689041630512X.

Spadacini, C. and Rizzi, D. (2017). "Radial outflow turbines for Organic Rankine Cycle expanders". In: *Organic Rankine Cycle (ORC) Power*

Systems. Elsevier, pp. 335–359. DOI: 10.1016/b978-0-08-100510-1.00011-9.

Spadacini, C., Xodo, L., and Quaia, M. (2017). "Geothermal energy exploitation with Organic Rankine Cycle technologies". In: *Organic Rankine Cycle (ORC) Power Systems*. Elsevier, pp. 473–525. DOI: 10.1016/b978-0-08-100510-1.00014-4.

Span, R. (2013). *Multiparameter equations of state: an accurate source of thermodynamic property data*. Springer Science & Business Media.

Spencer, L. (1989). "A comprehensive review of small solar-powered heat engines: Part II. Research since 1950—"conventional" engines up to 100 kW". In: *Solar Energy* 43.4, pp. 197–210. DOI: 10.1016/0038-092x(89)90020-0.

Spinelli, A., Cammi, G., Gallarini, S., Zocca, M., Cozzi, F., Gaetani, P., Dossena, V., and Guardone, A. (July 2018). "Experimental evidence of non-ideal compressible effects in expanding flow of a high molecular complexity vapor". In: *Experiments in Fluids* 59.8. DOI: 10.1007/s00348-018-2578-0.

Sprouse, C. and Depcik, C. (Mar. 2013). "Review of organic Rankine cycles for internal combustion engine exhaust waste heat recovery". In: 51.1-2, pp. 711–722. DOI: 10.1016/j.applthermaleng.2012.10.017.

Stanitz (1952). *One-dimensional compressible flow in vaneless diffusers of radial-and mixed-flow centrifugal compressors, including effects of friction, heat transfer and area change*. Tech. rep. No. 2610. NACA. URL: https://ntrs.nasa.gov/api/citations/19930083365/downloads/19930083365.pdf.

Al-Sulaiman, F. A., Dincer, I., and Hamdullahpur, F. (May 2010a). "Energy analysis of a trigeneration plant based on solid oxide fuel cell and organic Rankine cycle". In: *International Journal of Hydrogen Energy* 35.10, pp. 5104–5113. DOI: 10.1016/j.ijhydene.2009.09.047.

Al-Sulaiman, F. A., Dincer, I., and Hamdullahpur, F. (Apr. 2010b). "Exergy analysis of an integrated solid oxide fuel cell and organic Rankine cycle for cooling, heating and power production". In: *Journal of Power Sources* 195.8, pp. 2346–2354. DOI: 10.1016/j.jpowsour.2009.10.075.

Tabor, H. and Bronicki, L. (Apr. 1963). "Small turbine for solar energy power package". In: *Solar Energy* 7.2, p. 82. DOI: 10.1016/0038-092x(63)90015-x.

Thompson, P. A. (1971). "A Fundamental Derivative in Gasdynamics". In: *Physics of Fluids* 14.9, p. 1843. DOI: 10.1063/1.1693693.

Tian, H. and Shu, G. (2017). "Organic Rankine Cycle systems for large-scale waste heat recovery to produce electricity". In: *Organic Rankine Cycle*

(ORC) Power Systems. Elsevier, pp. 613–636. DOI: 10.1016/b978-0-08-100510-1.00017-x.

Tissandier, G. and Parville, H. de (1888). "Moteurs a vapeurs volatiles". In: *La Nat.* 790, pp. 113–114.

Tosto, F., Giuffre', A., Colonna, P., and Pini, M. (2021). "Non-ideal Effects in Compressible Swirling Flows". In: *Proceedings of the 3rd International Seminar on Non-Ideal Compressible Fluid Dynamics for Propulsion and Power*. Springer International Publishing, pp. 36–43. DOI: 10.1007/978-3-030-69306-0_5.

Tunakov, A. (1961). *Effect of the Radial Clearance on the Operation of a Centripetal Gas Turbine*. Tech. rep. FOREIGN TECHNOLOGY DIV WRIGHT-PATTERSON AFB OHIO.

Turunen-Saaresti, T., Uusitalo, A., and Honkatukia, J. (2017). "Design and testing of high temperature micro-ORC test stand using Siloxane as working fluid". In: *Journal of Physics: Conference Series* 821, p. 012024. DOI: 10.1088/1742-6596/821/1/012024. URL: https://doi.org/10.1088%2F1742-6596%2F821%2F1%2F012024.

Uusitalo, A., Zocca, M., Turunen-Saaresti, T., and Grönman, A. (Nov. 2021). "Analysis on gas dynamic effects and design of supersonic ORC stator nozzles for transcritical expansions". In: *Energy Conversion and Management* 247, p. 114703. DOI: 10.1016/j.enconman.2021.114703.

Van Der Waals, J. (1873). "On the Continuity of the Gaseous and Liquid States". In: ed. by T. N. UniversiteitLeiden Leiden.

Vanco, M. R. and Goldman, L. J. (1968). *Computer program for design of two dimensional supersonic nozzle with sharp edged throat*. Tech. rep. Cleveland, OH: NASA. URL: https://ntrs.nasa.gov/search.jsp?R=19680005278.

Vega, L. A. (May 2010). "Economics of Ocean Thermal Energy Conversion (OTEC): An Update". In: *All Days*. OTC. DOI: 10.4043/21016-ms.

Vitale, S., Pini, M., and Colonna, P. (May 2020). "Multistage Turbomachinery Design Using the Discrete Adjoint Method Within the Open-Source Software SU2". In: *Journal of Propulsion and Power* 36.3, pp. 465–478. DOI: 10.2514/1.b37685.

Wang, J., Zhao, L., and Wang, X. (Nov. 2010). "A comparative study of pure and zeotropic mixtures in low-temperature solar Rankine cycle". In: *Applied Energy* 87.11, pp. 3366–3373. DOI: 10.1016/j.apenergy.2010.05.016.

Watanabe, I., Ariga, I., and Mashimo, T. (Jan. 1971). "Effect of Dimensional Parameters of Impellers on Performance Characteristics of a Radial-

Inflow Turbine". In: *Journal of Engineering for Power* 93.1, pp. 81–102. DOI: 10.1115/1.3445411.

Wei, Z. (2014). "Meanline Analysis of Raidal Inflow Turbines at Design and Off-Design Conditions". PhD thesis. Carleton University. DOI: https://doi.org/10.22215/etd/2014-10546.

Weiß, A. P. (2015). "Volumetric expander versus turbine–which is the better choice for small ORC plants". In: 3rd ASME ORC conference. Brussels.

Wheeler, A. P. S. and Ong, J. (2013). "The Role of Dense Gas Dynamics on Organic Rankine Cycle Turbine Performance". In: *Journal of Engineering for Gas Turbines and Power* 135 (10). DOI: 10.1115/1.4024963. URL: https://doi.org/10.1115/1.4024963.

White, M. and Sayma, A. (2015). "The one-dimensional meanline design of radial turbines for small scale low temperature organic Rankine cycles". In: *ASME Turbo Expo 2015: Turbine Technical Conference and Exposition*. American Society of Mechanical Engineers, V02CT42A014–V02CT42A014. DOI: http://dx.doi.org/10.1115/GT2015-42466.

White, M. T. (2021). "Investigating the Validity of the Fundamental Derivative in the Equilibrium and Non-equilibrium Two-Phase Expansion of MM". In: *Proceedings of the 3rd International Seminar on Non-Ideal Compressible Fluid Dynamics for Propulsion and Power*. Springer International Publishing, pp. 3–11. DOI: 10.1007/978-3-030-69306-0_1.

White, M. T., Markides, C. N., and Sayma, A. I. (2018). "Working-Fluid Replacement in Supersonic Organic Rankine Cycle Turbines". In: *Journal of Engineering for Gas Turbines and Power* 140 (9). DOI: 10.1115/1.4038754. URL: https://doi.org/10.1115/1.4038754.

Zanelli, R. and Daniel, F. (1994). "Experimental investigation of a hermetic scroll expander-generator". In: Proceedings of the 12th international compressor engineering. Purdue.

Zhang, H., Wang, E., and Fan, B. (Feb. 2013). "A performance analysis of a novel system of a dual loop bottoming organic Rankine cycle (ORC) with a light-duty diesel engine". In: *Applied Energy* 102, pp. 1504–1513. DOI: 10.1016/j.apenergy.2012.09.018.

Zucrow, M. J. and Hoffman, J. D. (1977a). "Gas dynamics". In: vol. 1. John Wiley and Sons, Inc. Chap. 10, pp. 540–544.

Zucrow, M. J. and Hoffman, J. D. (1977b). "Gas dynamics". In: vol. 1. John Wiley and Sons, Inc. Chap. 12, pp. 580–621.